Title
Synthesis and Characterization of 14-1-11 Ytterbium Manganese Antimonide Derivatives for Thermoelectric Applications

Permalink

Author
Star, Kurt

Publication Date
2013

Peer reviewed|Thesis/dissertation

UNIVERSITY OF CALIFORNIA
Los Angeles

Synthesis and Characterization of 14-1-11 Ytterbium Manganese Antimonide Derivatives for Thermoelectric Applications

A dissertation submitted in partial satisfaction of the
requirements for the degree Doctor of Philosophy
in Materials Science and Engineering

by

Kurt Star

2013

ABSTRACT OF THE DISSERTATION

Synthesis and Characterization of 14-1-11 Ytterbium Manganese Antimonides for Thermoelectric Applications

by

Kurt Star
Doctor of Philosophy in Materials Science and Engineering
University of California, Los Angeles, 2013
Professor Bruce Dunn, Chair

$Yb_{14}MnSb_{11}$ is a promising thermoelectric material for high temperature applications with values of the non-dimensional figure of merit ZT peaking at 1.4 above 1200 K. $Yb_{14}MnSb_{11}$ exhibits low lattice thermal conductivity values and a p-type semimetallic behavior. This compound is a member of a large family of Zintl phases with a "14-1-11" $A_{14}MPn_{11}$ stoichiometry (Pn = As, Sb, Bi; A = Ca, La, Sr, Yb, Eu; M = Mn, Al, Cd, Ga, In, Nb, Zn). There is significant interest in investigating how substitutions on any of the atomic sites impact the band gap, lattice thermal conductivity and charge carrier concentration and mobility.

High energy ball milling is shown here to be a convenient method of synthesis to prepare $Yb_{14}MnSb_{11}$ and solid solution systems derived from this compound by substitution of elements. Here compositions in the $Yb_{14}Mn_{1-x}Al_xSb_{11-y}Bi_y$, $Yb_{14}MnSb_{11-y}As_y$, $Yb_{14-x}Ca_xMnSb_{11}$, Yb_{14-}

$_x$La$_x$MnSb$_{11}$ and Yb$_{14-x}$Na$_x$AlSb$_{11}$ systems are considered. Characterization of the synthesized compositions was done by X-ray diffraction, electron microprobe. High temperature measurements of the electrical and thermal transport properties were carried out up to 1275 K. The experimental results on solid solution samples are compared to that of pure Yb$_{14}$MnSb$_{11}$ samples prepared by the same synthesis technique. A single parabolic band degenerate Fermi statistical model was used to estimate various properties such as effective mass. Calculated lattice thermal conductivity in solid solutions was also compared to various models. Though some increase in ZT was calculated below 900K, none of the derivatives studied were calculated to have a averge ZT significantly higher than Yb$_{14}$MnSb$_{11}$.

The dissertation of Kurt Star is approved.

Laurent Pilon

Richard Kaner

Bruce Dunn, Committee Chair

University of California, Los Angeles
2013

To all those who have come before me.

CONTENTS

ACKNOWLEDGEMENTS

I have been very fortunate and am very grateful to have had two great advisors who have guided me on my path toward my Ph.D. My UCLA faculty advisor, Prof. Bruce Dunn, has been enthusiastically supportive of me in spite of my long absences from campus. My advisor at the Jet Propulsion Laboratory (JPL), Dr. Jean-Pierre Fleurial, has been likewise supportive as well as patient with the progression of my work. I also would like to thank Prof. Richard Kaner, Prof. Laurent Pilon and Prof. Vidvuds Ozolins for their time and discussion as they served on my committee.

I would like to thank my labmates in Prof. Dunn's group at UCLA especially Dr. Esther Lan and Dr. John Wang. I also thank the students of Prof. Kaner's group especially Danny King, James Ma and Michael Yeung. I also thank Dr. Frank Kyte for his assistance with microprobe operation.

As much of the work was carried out at JPL, I thank Dr. Thierry Caillat, Dr. Sabah Bux, Leslie D. Zoltan, George Nakatsukasa, Dr. Chen-Kuo Huang, and rest of the staff of the Thermal Energy Conversion Technologies Group at JPL who assisted in high temperature measurments. I would also like to thank Dr. Trinh Vo and Dr. Paul Von Allmen also at JPL. I also would like to give very special thanks to Prof. Jeff Sakomoto, now at Michigan State University, for giving me my start at JPL.

I thank Dr. G. Jeffrey Snyder and Alex Zevalkink at Caltech, Dr. Eric Toberer at the Colorado School of Mines and Prof. Susan Kauzlarich and Dr. Catherine (Cox) Uvarov at UC Davis for their helpful discussion.

I reserve the greatest thanks for my family. My wife Lisa has given me seemingly limitless amounts of patience and support throughout my time in grad school. I thank my parents, grandparents and the rest of my family for giving me the opportunity to achieve such a high distinction.

This work was funded by and part of this work was performed at the Jet Propulsion Laboratory, California Institute of Technology under contract with the National Aeronautics and Space Administration.

Chapter 5 contains material based on the work “Synthesis and Thermoelectric Properties of Doped $Yb_{14}MnSb_{11-x}Bi_x$ Zintls”, published in *Materials Research Society Symposium Proceedings*, volume 1267, 2010. It was co-authored with Alex Zevalkink and Dr. Chen-Kuo.Huang who provided technical discussion and Prof. Bruce Dunn and Dr. Jean-Pierre Fleurial who were co-principle investigators. I preformed all synthesis and charachterization. Chapter 6 contains material based on the work, “The Effect of Tm Substitution on the Thermoelectric Performance of $Yb_{14}MnSb_{11}$”, published in Science of Advanced Materials, volume 3, issue 4, 2011. It was co-authored with Catherine (Cox) Uvarov who preformed phase characterization of the materials, M. N. Abdusalyamova and F. Makhmudov who synthesized the materials and Jean-Pierre Fleurial and Susan M. Kauzlarich who were co-principle investigators. This research was additionally funded by NSF, DMR-0600742, International Science and Technology Center (ISTC) Project #T-1597. Sarah Roeske and Brian Joy provided assistance with microprobe analysis and Bruce Dunn provided additional helpful discussion.

VITA

2004	B.S. in Material Science and Engineering University of California, Los Angeles
2008	M.S. in Material Science and Engineering University of California, Los Angeles
2004-2011	Graduate Student Researcher Department of Materials Science and Engineering University of California, Los Angeles

PUBLICATIONS AND PRESENTATIONS

F, Marchioni, K, Star, E. Menke, T. Buffeteau, L. Servant, B. Dunn, & F. Wudl. “Protection of lithium metal surfaces using chlorosilanes”, *Langmuir*, *23*(23), 11597-11602 (2007)

C. A. Uvarov, M. N. Abdusalyamova, F. Makhmudov, K. Star, J.-P. Fleurial & S. M. Kauzlarich, “The Effect of Tm Substitution on the Thermoelectric Performance of $Yb_{14}MnSb_{11}$”, *Science of Advanced Materials*, *3*(4), 652-658 (2011)

K. Star, A. Zevalkink, C.-K. Huang, B. Dunn, & J.-P. Fleurial, “Synthesis and Thermoelectric Properties of Doped $Yb_{14}MnSb_{11-x}Bi_x$ Zintls”, H. L. Tuller, J. D. Baniecki, G. J. Snyder, & J. A. Malen (Eds.), *Materials Research Society Symposium Proceedings,* 1267, (2010)

V. A. Ravi, B. C. Y. Li, J.-P. Fleurial, & K. Star, “Fabrication of Lanthanum Telluride 14-1-11 Zintl High-Temperature Thermoelectric Couple”, *NASA Tech Briefs*, (November 2010)

K. Star, T. Ikeda, C.-K. Huang, B. Dunn & J.-P. Fleurial, “High Energy Ball Mill Synthesis and Thermoelectric Properties of the $Yb_{14-x}Ca_xMnSb_{11-y}Bi_y$ System”, 2007 MRS meeting, Boston, MA, November 27

K. Star, A. Zevalkink, C.-K. Huang, B. Dunn & J.-P. Fleurial, “Synthesis and Thermoelectric Properties of Doped $Yb_{14}MnSb_{11-x}Bi_x$ and $Yb_{14}MnSb_{11-x}As_x$ Zintls”, Spring 2010 MRS meeting, San Francisco, CA, April 6

K. Star, C.-K. Huang, B. Dunn & J.-P. Fleurial, “Synthesis & Thermoelectric Properties of $Yb_{14}MnSb_{11-x}As_x$ Zintls” Spring 2011 MRS meeting, San Francisco, CA, April 27

K. Star, C.-K. Huang, , T. Vo, P. Von Allmen, B. Dunn & J.-P. Fleurial, “Synthesis and Thermoelectric Properties of $Yb_{14}MnSb_{11}$ Derivatives”, The 30th International Conference on Thermoelectrics, Traverse City, MI, July 19 (2011)

Chapter 1. Introduction and Objectives

Thermoelectric materials have been instrumental in the exploration of space. $Yb_{14}MnSb_{11}$ is a recently identified high temperature p-type thermoelectric with a possible operational range up to 1300K. This is a dramatic improvement over SiGe which has been state-of-the-art in high temperature p-the thermoelectrics for over 40 years. There are many compounds which are isostructural to $Yb_{14}MnSb_{11}$ which have been identified but not characterized for high temperature electrical and thermal properties. Additionally, very little research has been published regarding the properties of their alloys. Experience from other material systems has shown that modifying compositions to adjust thermal and electrical properties can lead to materials with increased performance. $Yb_{14}MnSb_{11}$ has been synthesized by a relatively new high energy ball milling methods which is convenient for common powder forming methods. This dissertation addresses the effects of substitution of each of the three elements in $Yb_{14}MnSb_{11}$ to demonstrate the following: (1) demonstrating the wide application of high energy ball mill synthesis for these compounds, (2) improving the thermoelectric efficiency by altering materials properties through substitution and (3) estimating fundamental materials properties and establishing the validity of established models of electrical and thermal properties.

The first systems presented are those of $Yb_{14}MnSb_{11-y}Bi_y$ and $Yb_{14}MnSb_{11-y}As_y$. The suitability of $Yb_{14}MnBi_{11}$ as a thermoelectric has not been studied and $Yb_{14}MnAs_{11}$ has not been synthesized. There have been no-reported studies of any type for alloy compositions in the $Yb_{14}MnSb_{11-y}Bi_y$ or $Yb_{14}MnSb_{11-y}As_y$ systems. In this study, compositions were characterized for high temperature (~300K-1300K) electrical and thermal properties. Their performance as thermoelectric materials was evaluated. Electrical properties were then analyzed by simple models to estimate basic materials parameters. The results of measured thermal properties were compared to a predictive model.

The second system of focus is $Yb_{14}Mn_{1-x}Al_xSb_{11-y}Bi_y$. This section aims to reproduce work done on the $Yb_{14}Mn_{1-x}Al_xSb_{11}$ system which was synthesized using a “Sn-flux” method. In this dissertation, a different synthesis approach is used and further modeling methods are applied. The data and derived properties were compared between the two synthesis methods. The same approach was applied to the system $Yb_{14}Mn_{1-x}Al_xSb_{5.5}Bi_{5.5}$ which has not been previously synthesized.

The third focuses on substitution of Yb with other elements in $Yb_{14}Mn_{1-x}Al_xSb_{11}$. $Yb_{14-x}M_xMnSb_{11}$ where M=Ca and La and $Yb_{14-x}Na_xAlSb_{11}$ synthesized with the ball milling method were considered. For comparison, $Yb_{14-x}Tm_xMnSb_{11}$ samples synthesized via a Sn-flux method were also analyzed. These substitutions, with the exception of Ca, aim to change the carrier concentration to optimize performance. Samples were characterized and results are compared to $Yb_{14}Mn_{1-x}Al_xSb_{11}$ results in order to determine if any substation holds a potential advantage in performance**.**

Chapter 2. Background and History of Thermoelectric Devices

2.1. Thermoelectric Generators

2.1.2. Principle of Operation

Thermoelectric generators (TEG) have excelled at providing reliable, long lasting and maintenance free power in extreme environments.[1, 2] Thermoelectric converters have no moving parts and can be designed with a high level of redundancy in systems scaling from milliwatts to hundreds of watts. They have demonstrated extreme reliability, even when operating under harsh temperatures, pressures, vibration and radiation conditions. These properties have made radioisotope thermoelectric generators (RTGs), systems using thermoelectric elements to convert heat generated by a decaying radioisotope to electrical power, well suited for deep space exploration as well as use in remote terrestrial locations.[1, 3] Over the last 50 years, RTGs have a proven track record, and their graceful degradation in performance has been modeled accurately over their entire life cycle.[1, 3] The longevity of these devices is well illustrated by the Voyager I spacecraft that was launched in 1977 powered by three Multi-Hundred Watt RTGs (MHW-RTG) supplying 470W and has continued to transmit data beyond the edge of solar system with the RTG still supplying 285 Watts.[4]

At the heart of an RTG are many individual thermocouples that convert heat from the radioisotope decay heat into electrical power. A schematic of one such thermoelectric couple is shown in Figure 2.1. Heat radiates or conducts to a “hot shoe” which also electrically connects two legs consisting of one n-type and one p-type material. Opposite from the heat source, the legs are attached to an electrically insulated heat sink and leads for each leg. In evaluating these systems the temperatures are measured at the top of legs closest to the heat source (T_h) and at the bottom closest to the heat sink (T_c). The response to this temperature difference ($\Delta T= T_h- T_c$) generates a voltage due to the Seebeck effect which can be measured in the leads connected to the cold side of legs. Connecting the leads to a resistive load (R_L) will result in a current flow (I). In addition to power generation, the Seebeck effect is used in temperature sensing thermocouples. This same structure could be used for heat pumping, generally cooling, applications if a potential is applied to the leads due to the Peltier effect.

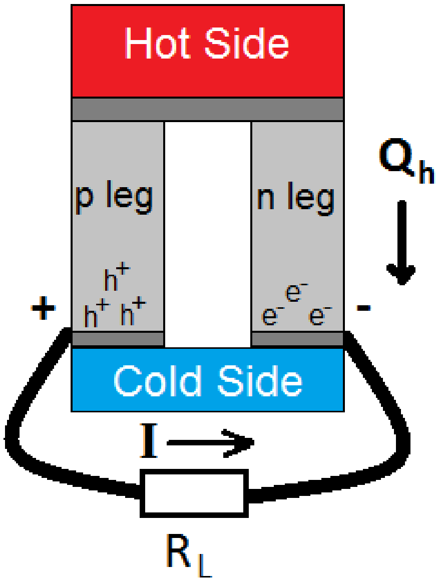

Figure 2.1: Schematic of an un-segmented thermoelectric couple in with a load resistance (R_l).

Thermoelectric devices can be thought of as heat engines that use charge carriers as the working fluid. As such, they can be considered to have an associated efficiency limit as defined by the Carnot cycle ($\eta=\Delta T/T_{hot}$). In RTGs, the electrical efficiency (η_e) can be written in terms of the electrical work done according to Joule's law in terms of voltage (V) and current (I) and the heat flow through the leg (Q_h).[2, 5, 6]

$$\eta_e = \frac{IV}{Q_h} \tag{2.1a}$$

When operating in power generation mode across a resistive load (R_L), equation (2.1a) can further be rewritten using the Seebeck coefficient (α), thermal conductivity (κ), the device internal electrical resistance (R) of both legs as well as the hot and cold side temperatures.

$$\eta_e = \frac{I(\alpha\Delta T - IR_L)}{I\alpha T_h + \kappa\Delta T - 1/2 I^2 R} \tag{2.1b}$$

The electrical power (P) of the thermoelectric device can be determined using the same variables.

$$P = \frac{\alpha\Delta T^2 R_L}{(R+R_L)^2} \tag{2.2}$$

The output electrical power is maximized when the internal resistance matches the load resistance (R=R_L). This condition when applied to equation (2.1b) then yields the well known equation featuring the dimensionless thermoelectric figure of merit (ZT).

$$\eta_{\max} = \frac{T_{hot} - T_{cold}}{T_{hot}} \frac{\sqrt{1+ZT}+1}{\sqrt{1+ZT}+\frac{T_{hot}}{T_{cold}}} \tag{2.3}$$

This ZT is related to the Seebeck coefficient (α), temperature (T), thermal conductivity (κ) and electrical resistivity (ρ) of the materials used.

$$zT = \frac{\alpha^2 T}{\kappa\rho} \tag{2.4}$$

It is important to note that the performance of a device depends on the average value of Z throughout the range between T_{hot} and T_{cold} as well as for both n- and p-type legs. Equation (2.1) reduces back to the Carnot efficiency as Z approaches infinity. In Figure 2.2, the maximum electrical efficiency of a device assuming a cold side operating temperature of 300K is plotted as a function of temperature for various values of ZT and the Carnot efficiency (ZT=∞). Figure 2.3 shows the ZT curves with temperature for material systems which are being investigated for RTG development and it is important to note that ZT values are not constant over operating temperature ranges.[1] While peak ZT values in excess of 1 are common, the average value over the operating range is what determines device performance. For high temperature applications (T_h≈1300K), state-of-practice thermoelectric materials have average ZT values of about 0.5 across the full temperature range, and for a 1000K difference this yields theoretical efficiencies of about 11%. This is in contrast to mechanical turbine power generation systems which can achieve real world thermal-to-electric efficiency conversions in excess of 60%.[7]

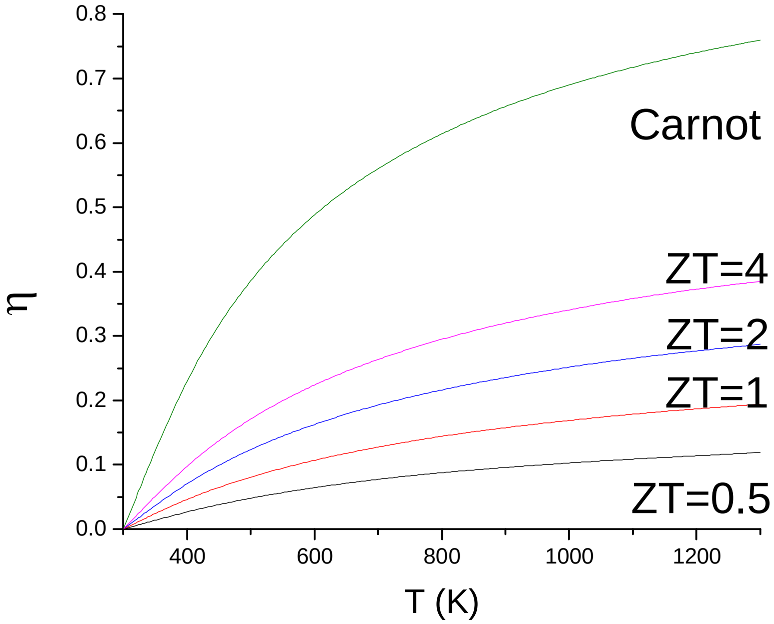

Figure 2.2. Efficiencies of a thermoelectric device as a function of hot junction temperature for various values of ZT while holding the cold side of the device at 300K. The Carnot efficiency (achieved for very large values of ZT) is also shown for reference.

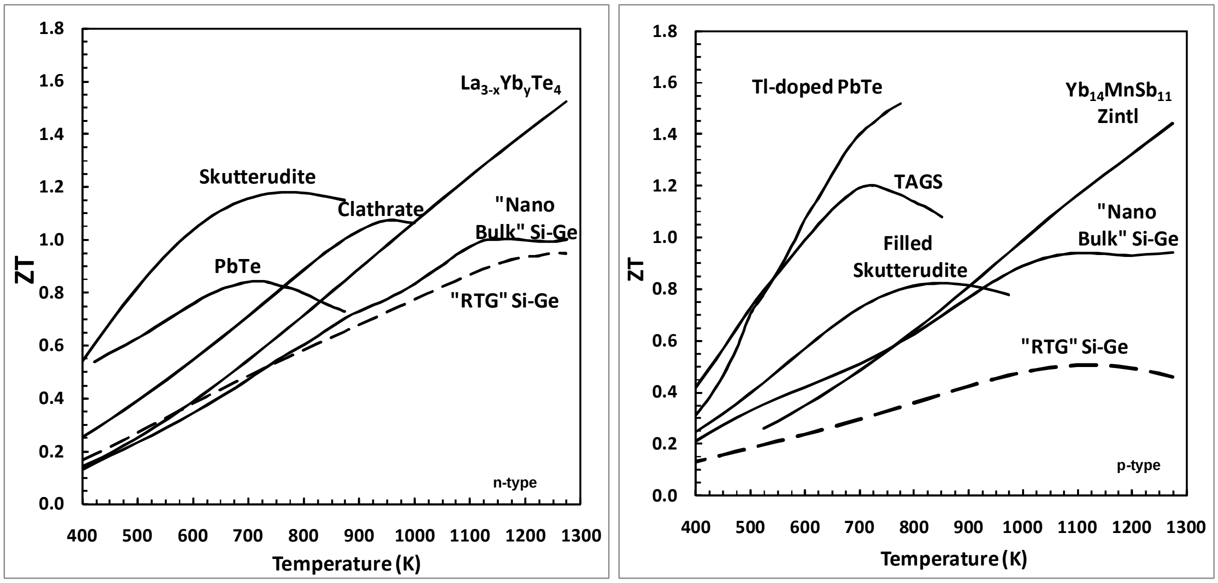

Figure 2.3. ZT versus temperature plots for n-type (left) and p-type (right) materials being investigated for use in RTG applications measured at JPL from reference 1.

Besides improving ZT values, to improve the efficiency of the thermoelectric device, each leg might be segmented to take advantage of the fact that the performance of materials, peaks at different temperatures in different materials. Figure 2.4b shows an example of two ZT curves for two hypothetical materials. In a leg was only composed of Material 2 (Figure 2.4b, curve b), a resulting average ZT of ~0.5 would be obtained for the leg (Figure 2.4b, curve b). But devices may be constructed with segmented legs as shown in Figure 2.4a with a second material (Material 1, Figure 2.4b, curve a). This device can be engineered so that the boundary temperature (Figure 2.4b, line c) between the two materials optimizes the average ZT of the leg. The lower temperature Material 1 segment operates at a higher average ZT (Figure 2.4b, line e) than the higher temperature Material 2 over the lower portion of the device's operating range, resulting in an overall higher average ZT (Figure 2.4b, line g). In this example between 400K and 1273K, the increase in ZT from ~0.5 to 0.65 yields a substantial increase in conversion efficiency from 10% to 12%. In practice, other material properties such as the coefficient of thermal expansion and the thermoelectric compatibility factor also need to be taken into account.[1, 8, 9] A good example of a successful system is the p-leg in the 1960's Viking lander SNAP-19 RTG which used GeTe-AgSbTe$_2$ (TAGS) for lower temperatures coupled with a (Pb,Sn)Te for higher temperatures.[2]

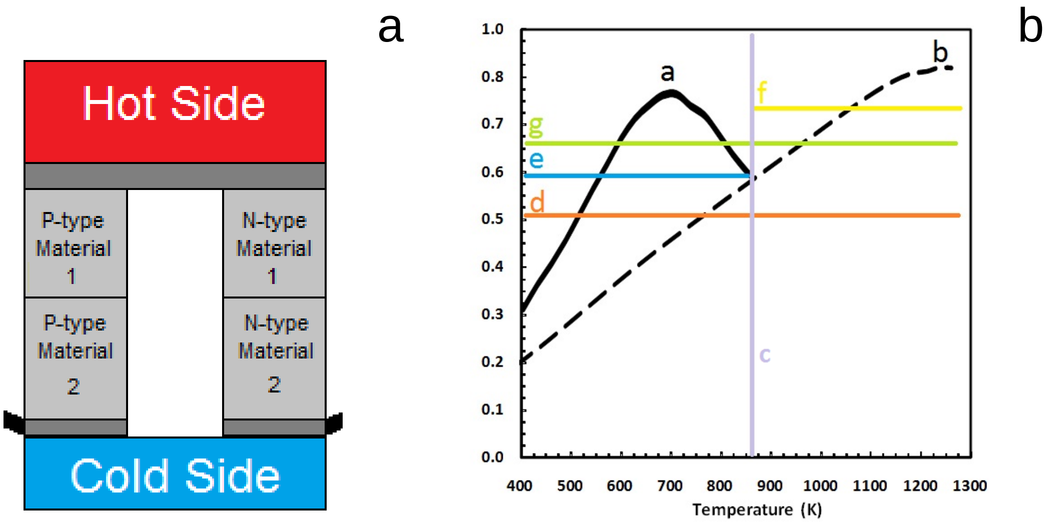

Figure 2.4. a) Schematic of a segmented thermoelectric couple. b) A ZT versus temperature plot of curve a and b as the measured ZT curve for a hypothetical Material 2 and Material 1 respectively. Line c represents the boundary temperature of 850K between Materials 1 and 2 in a segmented thermocouple. Line d shows the average ZT over between 400-1275K of an un-segmented couple made out of material 2. Line e shows the average ZT for Material 1 between 400K and 850K and Line f shows the average ZT for Material 2. Line g shows the resulting improved average ZT of the segmented leg. (Plot after Jean-Pierre Fleurial, JPL)

Thermoelectric power generators require effective thermal and mechanical integration with suitable heat sources as well as heat sink for rejecting the waste heat not converted to electricity. The heat source can be any source of heat, but in deep space applications, US missions have favored plutonium-238 dioxide which has a half-life of 87.7 years. Historically, terrestrial sources have used various forms of strontium-90 which has a half-life of 28.79 years.[3, 10] For space missions, various heat source designs have been used to provide hot side temperatures between 1000 and 1300K.[1, 2, 11] For more commercial applications, currently there is interest in using waste heat from diverse sources such as cars, waste incinerator furnaces, and jet aircraft in order to increase the efficiency of their operation.[1, 2] There have even been systems designed to use body heat to power low power personal electronics.[12] Thermoelectric materials are also being investigated for use in small scale solar-thermal ovens for remote impoverished communities.[1]

For heat rejection, most terrestrial applications use simple forced convection, conduction and radiation systems to remove waste heat to the surrounding air or water.[1, 2] Space thermoelectric power systems have typically high radiator temperatures, ranging from 450 K up to 550 K, that help both minimize radiator size and system mass, as well as provide high quality waste heat for spacecraft thermal management.[1-3, 11] In space-based systems and terrestrial systems used in extremely cold environments, the waste heat is also the means by which to accomplish effective thermal management of sensitive electronics and energy storage components, the unused heat being radiatively dispersed into space. Despite the benefit of an all solid-state device and its ability to easily integrate with a variety of heat sources and heat sinks, thermoelectric power generation is still a niche technology.

2.1.2. Performance and Competing Technologies

The rather low conversion efficiency of thermoelectric generators is the major limitation in their wider adoption. In a practical system, the MHW-RTG has a total efficiency of 6.5% producing 4.2 W/kg operating between 1300K and 400K.[3] By comparison, commercial portable mechanical systems routinely have efficiencies that approach 30% electrical efficiency using temperature differences of 700K.[2] Because of the huge potential performance gains in using mechanical cycles, NASA is developing Stirling cycle engines as an alternative to its current work on thermoelectrics. The Advanced Stirling Radioisotope Generator (ASRG) is an alternative to RTGs and has been stated to have 28% efficiencies operating between 923K and 363K producing 5.0 W/kg.[11] The obvious efficiency advantage of mechanical systems was well known since the first "System for Nuclear Auxiliary Power" device (SNAP-1) developed in the early 1960's, which was a Rankine cycle engine using mercury as a working fluid with a 10% cycle efficiency.[13] However, the reliability of such systems over the long periods of operation (10 to 30 years) typical of NASA deep space missions still remains to be demonstrated.

Another technology rival to thermoelectrics is thermionic diodes utilizing the Edison Effect. These devices achieved conversion efficiencies of up to 20% in early SNAP development. For efficient operation, these devices require high vacuums maintained at above 2000K which present significant technical and material problems.[13] Solid state devices using thermionic effects have been fabricated with some success.[14] Despite the efficiencies of mechanical and thermionic systems, the proven reliability of RTGs has uniquely enabled a number of deep space science missions, some of them still ongoing after more than 30 years of operation.[1, 3]

Modern solar panels have power densities of several hundred Watts per kilogram in Earth orbit while RTG provide power on the order of a few Watts per kilogram.[1, 3, 7] Therefore, solar modules have been the most important power source since the early space program. However, since solar intensity is inversely proportional to the square of the distance from the sun, solar panels stop being practical past Mars or for long term planetary surface missions like the Mars Science Laboratory (MSL) for which solar power alone is not practical.[1, 3] For space applications, RTGs have unique concerns which differ from terrestrial applications. The main selection criterion for any space application is generally dominated by launch costs which are about \$10,000/kg.[15] This lowers the barriers of materials costs which is critical in most terrestrial applications and emphasizes weight reduction. In addition, the cost and availability of the heat sources for space system is driving the need for higher efficiency thermal-to-electric power systems. As a result NASA is supporting advanced technology development in thermoelectric materials and conversion technology that can lead to factors of 2 to 4 in both specific power (6 to 12 W/kg) and conversion efficiency (13 to 25%) of future RTGs.

2.2. Advanced Material Systems

2.2.1. State-of-practice Thermoelectric Materials

A very telling fact about the development of thermoelectrics is that the first Multi-Mission Radioisotope Thermoelectric Generator (MMRTG) used in the MSL launched in 2011 is based on the same thermoelectric technology as the SNAP-19 RTG used in the Viking I mission launched in 1975.[1, 3, 13] In fact, most current state of practice materials were well known and identified in the 1940's-50's by work done largely in the USA and USSR.[1] Optimizing carrier concentrations as well as alloy compositions in n- and p-type PbTe, Bi_2Te_3, PbSnTe, Si-Ge, and p-type Bi-Sb systems through the 1960's allowed these systems to reach peak ZTs of 0.6 to 1.0.[1] The one exception to this was the p-type GeTe-$AgSeTe_2$ (TAGS) system with peak ZT values of about 1.2 to 1.4. It has been recently suggested that this material benefited from nano-scale structural features.[16] While marginal gains were made in the 1970's, there were no breakthroughs in material systems.[1]

In the 1980's, the research community made some progress in developing high temperatures systems which exceeded ZTs of 1.[1, 3] One advance was a modification of the Si-Ge system where the addition of GaP allowed for more stable high doping levels of n-type dopants. A peak ZT of 1.3 at 1300K was achieved.[6] Another advance was made in rare-earth chalcogenides where n-type $La_{3-x}Te_4$ exhibited a peak ZT of 1.4 at 1200K. For p-type materials, boron carbides with carrier hopping conduction were projected to have a ZT of 3 at 2000K.[6] This would have been used in combination with wide band-gap $La_{3-x}S_4$ based material which also had a projected ZT of high value. However, the lack of materials compatibility between boron carbide and rare earth chalcogenides, as well as device operation at those elevated temperatures (~ 1500K) hampered their development.[1]

2.2.2. Novel Approaches

Another general trend during the 1980's and 1990's was that of modifying microstructures to lower the thermal conductivity of established systems.[1] This modification involves "forced assembly" and "self assembly" routes. Forced assembly routes include; mechanically reducing particle sizes to a few micrometers or less, introducing defects via neutron radiation and introducing ultra fine particles.[1] Self-assembly methods generally involved using phase separation or decomposition forming fine microstructures.[1, 17] Despite large amounts of effort and great gains in understanding thermoelectric materials, there was virtually no practical advancement in the state of the art to emerge from these novel approaches.[1]

Exploration for high temperature superconductors and novel magnetic effects during the 1990's led to the next wave of thermoelectric research by discovering new phases as well as improved synthetic methods. Chevrels (i.e. $Cu_xMo_6Se_8$)[18], clathrates (i.e. $Ba_8Ge_{16}Ge_{30}$)[19], filled skutterudites ($CeFe_4Sb_{12}$)[20], and half-Heuslers (ZrCoSb)[21] are complex materials which were first identified as thermoelectrics during this period and still are of active interest. These complex materials all exhibited low lattice thermal conductivities due to their complex crystal structure.[22, 23] Filled skutterudites along with silicide materials are especially promising for terrestrial applications because they have been measured to have a higher ZT than PbTe with fewer environmental concerns and lower costs.[1, 24]

2.2.3. 14-1-11 Zintls

In 2006, Kauzlarich and Snyder published high temperature data for $Yb_{14}MnSb_{11}$ claiming a peak ZT of ~1 at 1300K.[25] This was a substantial improvement over the p-type $Si_{0.8}Ge_{0.2}$ which only has a ZT at that temperature of ~0.5.[1, 26] This value was later revised downward to 0.8 after further heat capacity measurements were made, but it still remained a remarkable increase.[27] The first report of $Yb_{14}MnSb_{11}$ synthesis involved a direct reaction of the constituent elements to a peak temperature of 1200 ^{o}C.[28] It was initially prepared in order to study its low temperature magnetic properties since $Ca_{14}MnSb_{11}$ showed evidence of the rare Ruderman-Kittel-Kasuya-Yosida (RKKY) type magnetic ordering where the ordering of Mn ions is facilitated by conduction charge carriers.[29] Little else was done with the material until the thermoelectric properties were reported.[25]

$Yb_{14}MnSb_{11}$ belongs to a wide family of materials that are isostructural with $Ca_{14}MnSb_{11}$ and often written as $A_{14}MPn_{11}$ (Pn = P, As, Sb, Bi; A = Ca, Ba, La, Sr, Yb, Eu; Mn = Mn, Al, Cd, Ga, In, Nb, Zn).[29-33] These are often referred to as “14-1-11” materials. It also is often called a “Zintl.” Strictly speaking, Zintl compounds are Alkali metals or Alkaline earths reacted with post transition metalloids or metals. In this case, rare earths and the inclusion of phosphorus, transition metals and rare earths go outside that definition.[34] However, the Zintl-Klemm concept which governs the stricter definition for the most part works well with this family of materials. This concept was first developed to describe why intermetallic compounds behaved like brittle ionic materials as opposed to being ductile metals. In the Zintl-Klemm concept, Alkali or Alkaline metals (or in this case rare earths) are treated as cations.[34] Anions are created by arranging covalently bonded post transition elements and treating unpaired electrons as donor electrons. Adding together the total charges of the cations and “Zintl anions” should predict if the material is charged balanced or has free electrons or holes.[35] This concept therefore is potentially very helpful in predicting the behavior of substitutions in $Yb_{14}MnSb_{11}$.

The structure of $Yb_{14}MnSb_{11}$ can be seen in Figure 2.5a and the post transition metal groups shown in Figure 2.5b. In Zintl-Klemm counting, the 14 Yb atoms are assumed to be Yb^{+2} ions. The 4 isolated Sb atoms are assumed to be Sb^{-3} ions. A linear chain of 3 Sb atoms with a ``three center, four electron" bonded structure is taken to be a Zintl ion of $[Sb_3]^{-7}$.[36] The next element is the $[MnSb_4]^{-9}$ cluster which can be thought of as a $[MnSb_4]^{-11}$ anion cage surrounding a Mn^{2+} cation.[28] Added together, this structure is deficient by one electron leading to a conducting hole. For $Yb_{14}MnSb_{11}$, this would lead to a hole concentration of p=1.2.10^{21} cm^{-3} which is in good agreement with the measured carrier concentration of Sn-flux grown materials.[25] In $Yb_{14}AlSb_{11}$, replacing Mn^{2+} with Al^{3+} forms $[AlSb_4]^{-8}$ clusters which should lead to a semiconductor. Studies with $Yb_{14}Mn_{1-x}Al_xSb_{11}$ have indeed shown good agreement with those counting rules. Likewise in $Yb_{14-x}La_xMnSb_{11,}$ for every La^{3+} in the structure that replaces an Yb^{2+} an extra electron is added which compensates a free hole. $Yb_{14}Mn_{1-x}Al_xSb_{11}$ and $Yb_{14-x}La_xMn_1Sb_{11}$ show an equal reduction in carrier concentration for equal values of x.[37]

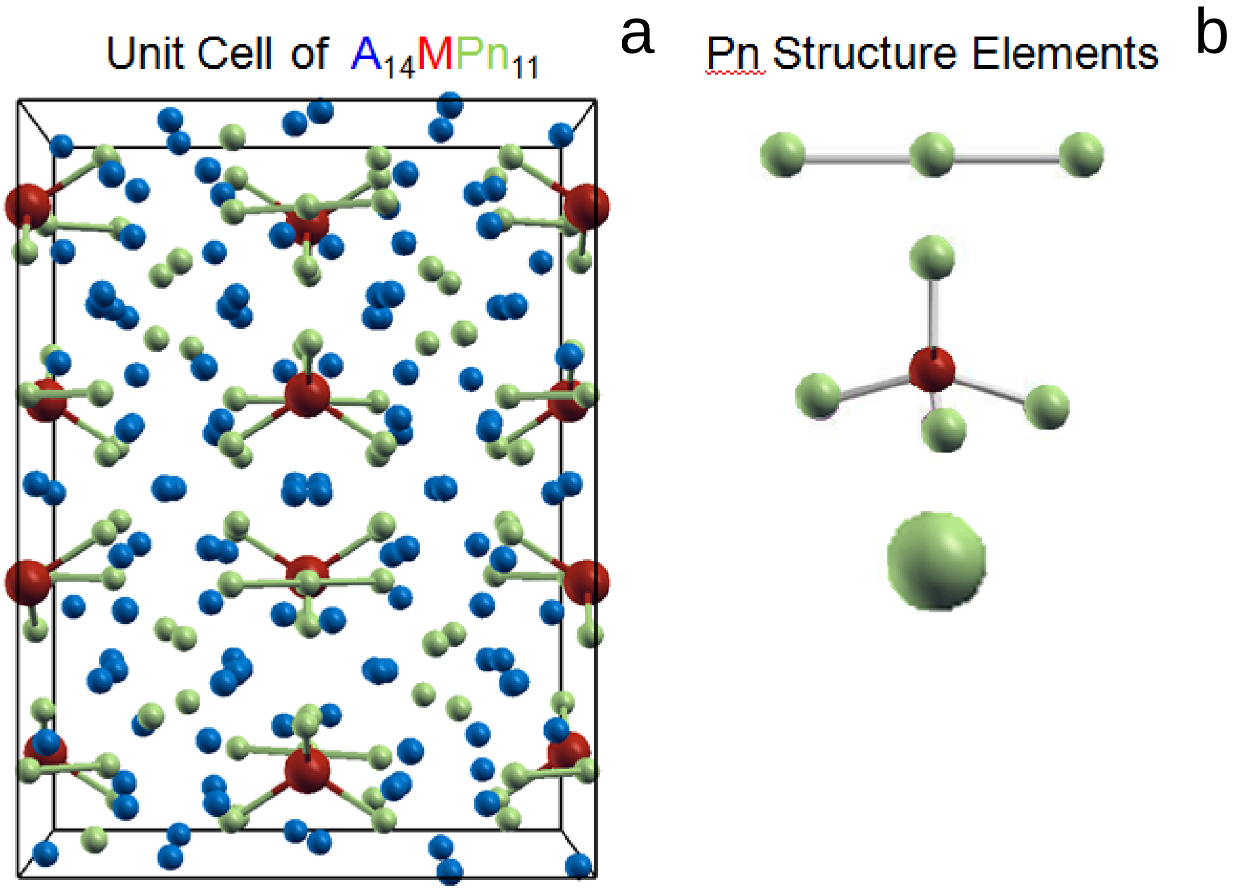

Figure 2.5. a) Unit cell of a generic $A_{14}M_1Pn_{11}$ structure. b) Zintl ions (top to bottom) $[Pn_3]^{-7}$, $[MPn_4]^{-11}$ (assuming M^{2+}) and Sb^{-3}. (Generated by Paul von Allmen, JPL)

For some members of the 14-1-11 family, this formalism does not translate as completely. Although zinc substitution should be isoelectronic with manganese, with $Yb_{14}Mn_{1-x}Zn_xSb_{11}$ there is some evidence of valence fluctuations of Yb^{+2} to Yb^{3+} for x>0.7.[38] In $Yb_{14-x}Ca_xMn_1Sb_{11}$, there is an observed decrease in carrier concentration even though the substitution of Yb with Ca should be isoelectronic.[39] In this thesis, substitutions made on the Sb site also lead to unpredicted changes in carrier concentration. Therefore, while the Zintl counting rules are a guide, the conditions do not always seem to firmly apply.

Calculating the band structure of $Yb_{14}MnSb_{11}$ is not a simple problem. Firstly, the $Ca_{14}AlSb_{11}$ type structure has a very large unit cell with 104 atoms which requires a large amount of processing time needed to undertake calculations.[40] Modeling of the ytterbium f electrons has been a great technical challenge as well as accounting for the magnetic effects on spin from the manganese atoms.[36, 40] For first principles calculations, the much simpler $Ca_{14}AlSb_{11}$ compound is used as a stand-in for $Yb_{14}MnSb_{11}$ to attempt to understand band structure.[40, 41] Furthermore, the use of $Ca_{14}AlSb_{11}$ does take into account the effects of the Jahn-Teller distortion of the $[MnSb4]^{-11}$ tetrahedra or the electro negativity difference between calcium and ytterbium. Some, earlier first principles calculations on $Ca_{14}MnBi_{11}$ which were done to validate magnetic response, indicated that a single parabolic band structure should be adequate for predicting the electrical behavior for these materials.[36] Efforts are currently underway by Vo and Von Allmen to better model the system, but calculations so far have been mostly carried out on variations of $Ca_{14}AlSb_{11}$.[40] Finally, there are few 14-1-11 compounds which have been characterized for high temperature electrical properties. With limited data, it is difficult to validate first these first principles models. Thus far, despite some insights, computational methods of determining electrical properties of 14-1-11, using concepts like the Zintl-Klemm concept, periodic table trends, single band carrier statistics and the Debye model are the primary tools to guide the search for compositions with improved ZT.

2.3. Modeling of Electronic and Thermal Transport

2.3.1. Electrical Transport

With Ohm's law, the resistivity of the material may be written in terms of the carrier concentration (n), the carrier mobility (μ) and the charge of an electron (e).

$$\rho = 1/\sigma = 1/n\mu e \qquad (2.5)$$

Furthermore, as shown in equation (2.6), the carrier mobility maybe be written in terms of the effective mass (m*), the charge of an electron and a charge carrier scattering time (τ).

$$\mu = \frac{e\tau}{m^*} \qquad (2.6)$$

The carrier concentration (n) as a function of Fermi energy in the general case given as:

$$n = \int_0^\infty g(E) F_0(E) dE \qquad (2.7)$$

Where g(E) is the density of states in the solid as a function of energy and where F_0 is the Fermi integral for n=0:

$$F_n = \int_0^\infty \frac{\eta^n}{1+\mathrm{e}^{x-\eta}} dx \qquad (2.8)$$

Commonly, the single parabolic band approximation is made so that $g(E) = m^{*3/2}\sqrt{2E}/\hbar^2\pi$ leading to the common relationship using the reduced Fermi energy ($\eta=(E_f-E_c)/k_bT$, for p-type material):

$$n = \frac{4}{\pi^{1/2}} \left(\frac{2\pi m^* kT}{h^2} \right)^{3/2} F_{1/2}(\eta) \qquad (2.9)$$

In degenerate semiconductors, the picture is more complicated than in lightly doped one. To estimate the electrical resistivity of a material, the value for τ now is variable, as a function of the reduced Fermi level in the system. The scattering time takes $\tau = \tau_0 \eta^{r-1/2}$ dependency. And the value of r varies with the type of scattering mechanism: for electron-phonon scattering r=1 ($\tau_{ph} = \tau_{0ph} \eta^{1/2}$) for electron ionized impurity scattering present in the material r=2 ($\tau_{im} = \tau_{0im} \eta^{3/2}$) and for neutral impurities r=1/2 which is energy independent.[10, 42] Models to estimate τ_{0ac} and τ_{0im} have been developed incorporating Plank's constant (h_s), speed of sound (v_s), density (d), a deformation potential relating the change in energy of a band by the deformation caused by the presence of a phonon (E_{def}), dielectric constant (ε_d) and the number of ions per volume (N_d).[42]

$$\tau_{ac0} = \frac{\pi h_s^4 v_s^2 d}{\sqrt{2} E_{def}^2 (m^* k_b T)^{3/2}} \tag{2.10}$$

$$\tau_{im0} = \frac{\sqrt{2m^*} \varepsilon_d^2 (k_b T)^{3/2}}{\pi e^4 N_d} \tag{2.11}$$

To take into account, the energy dependence of the scattering time in determining conductivity, the Mott relationship[43] is used:

$$\sigma = \int_0^\infty \sigma(E) \left(-\frac{\partial F_0(E)}{\partial E} \right) dE \tag{2.12}$$

From that relationship, Cutler and Mott derive a relationship for the Seebeck coefficient[44]:

$$S = \frac{k_b}{q\sigma} \int_0^\infty \sigma(E) \left(\frac{E - E_F}{k_b T} \right) \left(-\frac{\partial F_0(E)}{\partial E} \right) dE \tag{2.13}$$

For a degenerate system such as metals, semimetals and degenerately doped semiconductors this relationship simplifies to:

$$S = \frac{\pi^2 k_b}{3q}\frac{k_b T}{\sigma}\left(-\frac{d\{\ln[\sigma(E)]\}}{dE}\right)_{E=E_f} \tag{2.14}$$

Making further simplifications, assuming a free electron gas, the Seebeck coefficient can be written as:

$$\alpha = \frac{8\pi^2 k_b^2}{3eh^2} T m^* \left(\frac{\pi}{2n}\right)^{2/3} \tag{2.15}$$

In some cases, it has been convenient to rewrite equation (2.15) in a derivative form.[45]

$$\frac{d\alpha}{dT} = \frac{8\pi^2 k_b^2}{3eh^2} m^* \left(\frac{\pi}{2n}\right)^{2/3} \tag{2.15a}$$

Equation (2.15) is only a useful approximation in systems which are metallic. To look at more semiconducting materials, an approach which takes into account energy dependence of scattering times is necessary. Using a formulism set forth by Fistul[42], we define a parameter *b*.

$$b^2 = \frac{\tau_{0ph}}{\tau_{0imp}} \tag{2.16}$$

Using Fermi-Dirac statistics, equation (2.14) and assuming a parabolic band, the Seebeck coefficient can be written as:

$$\alpha = \frac{k_b}{e}\left(\frac{\Phi_4(\eta,b)}{\Phi_3(\eta,b)} - \eta\right) \tag{2.17}$$

$$\Phi_n = \int_0^\infty \frac{\eta^n \exp(x-\eta)}{(n^2+b^2)(1+\exp(x-\eta))^2}dx \tag{2.18}$$

$$\Phi_{n+1/2} = \int_0^\infty \frac{\eta^{n+1/2} \exp(x-\eta)}{(n^2+b^2)^2(1+\exp(x-\eta))^2}dx \tag{2.19}$$

The formula for the electrical conductivity σ, and Hall carrier mobility (μ_H), may also be defined.

$$\sigma = \frac{8\pi e^2}{3h^2 m^*}(2m^* kT)^{3/2}\tau_{ph0}\Phi_3(\eta,b) \tag{2.20}$$

$$\mu_H = \frac{e}{m^*}\tau_{ph0}\frac{\Phi_{9/2}(\eta,b)}{\Phi_3(\eta,b)} \tag{2.21}$$

In the Hall equation, when calculating carrier concentration from a measured Hall coefficient (R_H), it is often assumed that the hall factor (r_H) is unity, however it is dependent on energy dependent carrier scattering and η.

$$R_H = \frac{r_h}{n \cdot e} \tag{2.22}$$

$$R_H = \frac{3h^2}{8\pi(2m^* kT)^{3/2}}\frac{\Phi_{9/2}(\eta,b)}{[\Phi_3(\eta,b)]^2} \tag{2.22a}$$

$$r_H = \frac{3}{2}\frac{F_{1/2}(\eta)\Phi_{9/2}(\eta,b)}{[\Phi_3(\eta,b)]^2} \tag{2.22c}$$

Therefore, by measuring the Seebeck coefficient, η maybe be numerically estimated, assuming or calculating values for τ. With η and the Hall coefficient or resistivity, the effective mass of the carriers may in turn be calculated.

The thermal conductivity of a material is often written in terms of the thermal diffusivity, heat capacity and mass density of the material.

$$\kappa = \rho D_T C_p \tag{2.23}$$

The thermal conductivity of extrinsic materials with few minority carriers can be considered to consist of three contributions ($\kappa = \kappa_e + \kappa_l + \kappa_b$): the electronic term ($\kappa_e$), the lattice term ($\kappa_l$) and bipolar term ($\kappa_b$). The electronic term is largely dependent on the conductivity of the sample and can be engineered by modifying carrier concentration or the type of charge carrier scattering. The Wiedemann–Franz law ($\kappa_e = L\sigma T$) may be used to calculate this κ_e, where the Lorenz number (L) represents a measure of electron-phonon coupling. Using a free electron gas model, it can be found that L will have a value of 2.4x10^{-8} W Ω K^2. However, in the case of degenerate semiconducting materials this value has a dependence on η which for our currently discussed degenerate statistics model can be estimated as:[42]

$$L = \frac{k^2}{e^2}\frac{\Phi_3(\eta,b)\Phi_5(\eta,b)-\left[\Phi_4(\eta,b)\right]^2}{\left[\Phi_3(\eta,b)\right]^2} \tag{2.24}$$

Figure 2.6 shows the value of L calculated for JPL-producedYb$_{14}$MnSb$_{11}$ in the acoustic phonon scattering (b=0) and the ionized impurity scattering case (b>>0) versus the metallic limit of L.[46] Using the free electron model can lead to an overestimation of *L* by nearly 30% compared to the acoustic scattering case (b=0) and under estimate values of L by nearly 10% at 1200K in the case of charged defect scattering (b>>0).[23] At higher temperatures, the effects of thermally excited carriers influence the total thermal conductivity. In this case, there is, in addition to their contribution to total electrical conductivity, an enhanced heat transport effect due to the creation and annihilation of electron-hole pairs which is commonly referred to as the bipolar thermal conductivity (κ_b).

$$\kappa_b = \frac{k_b^2 T^2}{e}\frac{\sigma_p\sigma_n}{\sigma^2}\left(\alpha_p-\alpha_n\right)^2 \tag{2.25}$$

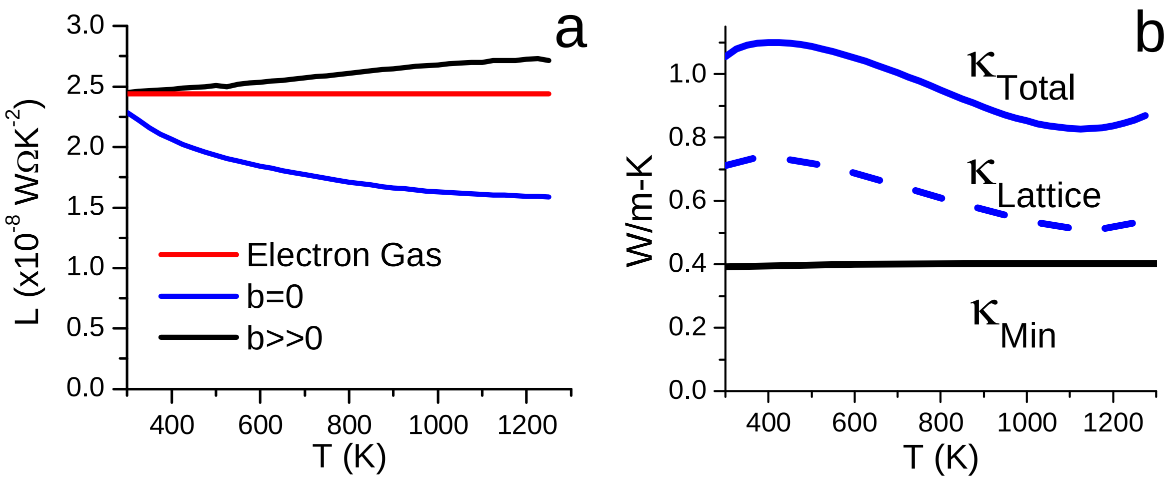

Figure 2.6. a) A graph of the Lorenz number (L) for the constant value derived from an electron gas, degenerate statistics model assuming acoustic scattering (b=0) and ion impurity scattering (b>>0) or electrons. b) Plot of thermal conductivity of JPL ball milled $Yb_{14}MnSb_{11}$ with the thermal conductivity calculated assuming b=0 ($\kappa_t - \sigma LT = \kappa_l$) and the minimum κ_l as calculated with equation (2.10).

2.3.2. Thermal Transport

The lattice thermal conductivity is dependent on the structure, mass and bonding of the atoms in the material. Assuming an average phonon velocity equal to the low frequency speed of sound(v), the lattice thermal conductivity can be written in terms of the mean free path (l) or a phonon relaxation time ($\tau = l / v$) and the heat capacity (C_v).

$$\kappa_L = \frac{1}{3} C_v v l = \frac{1}{3} C_v v^2 \tau \qquad (2.26)$$

This yields an important result since the speed of sound can be shown to be proportional to the square root of the elastic modulus divided by density ($v \propto \sqrt{\lambda / d}$). Therefore, the obvious materials for low lattice thermal conductivity are going to be “softly” bonded materials with heavy atoms which describe many of most commonly used thermoelectric material systems such as Bi-Sb, PbTe, (Pb,Sn)Te and Bi_2Te_3.[2] However, similar to the case of charge carriers, the simple situation is complicated by the quantized nature of phonons and the energy dependence of the relaxation times.

The Debye model is the most common tool used to describe lattice phonons. Assuming a linear dispersion of phonon states, the differential frequency-dependent heat capacity can be estimated.

$$C_v(\omega)d\omega = \frac{3\hbar^2\omega^2}{2\pi^2 v^3}d\omega \tag{2.27}$$

Quantizing phonons, we get the classic equation for the heat capacity of a material.

$$C_v = \frac{3\hbar^2}{2\pi^2 k_b T^2}\int_0^{\omega_m}\frac{\omega^4 e^{\hbar\omega/k_bT}}{v^3\left(e^{\hbar\omega/k_bT}-1\right)^2}d\omega \tag{2.28}$$

In the Debye model, it is assumed that the Debye frequency is equal to the maximum phonon frequency in the acoustic branch and is dependent on the speed of sound and average atomic volume (δ^3).

$$\omega_{\max} = \omega_D = \frac{\left(6\pi^2\right)^{1/3} v}{\delta} \tag{2.29}$$

This also leads to defining a Debye temperature ($k_b\theta_D=\hbar\omega_D$) that in practice leads to the temperature where the heat capacity approaches the Dulong-Petit heat capacity ($C_v=3k_bM$). Similar to charge carriers, heat capacity, phonon velocities and relaxation times need to be treated as a frequency dependent dispersion to be estimated in this model.[47, 48]

$$\kappa_L = \frac{1}{3}\int_0^{\omega_{\max}} C_v(\omega)v(\omega)^2\tau(\omega)d\omega \tag{2.30}$$

Given the heat capacity frequency dependence of equation (2.30) and a frequency-independent speed of sound, a formula to estimate the lattice thermal conductivity can be stated with τ of unknown dependence.[49]

$$\kappa_L = \frac{k_b}{2\pi^2 v}\left(\frac{k_b T}{\hbar}\right)^3 \int_0^{\omega_{\max}} \frac{\omega^4 e^{\hbar\omega/k_b T}}{\tau^{-1}\left(e^{\hbar\omega/k_b T}-1\right)^2} d\omega \qquad (2.31)$$

The determination of the relaxation constants has many parallels to scattering times of phonons. The relaxation time of phonons is a parallel process as is the case with charge carriers. Likewise there is an energy dependence which in the case of phonons we write now in terms of phonon frequency ($\tau = \tau_0\ \omega^{-2r}$). For r=0, we have the case for boundary scattering of phonons (τ_b=L/v) in which bulk material is rarely a consideration. Engineering relaxation time is generally considered to be the main cause of measured reduction in the thermal conductivity of micro- and nano-structured materials.[22] Phonon-electron scattering can be described by r=1/2. This is often assumed to be negligible as this scattering is most active for frequency phonons well below ω_D.[2] For r=1, this is the case of Umklapp scattering of phonons (τ_u) and while models vary about the exact formulation of this term but it can be generally be said that $\tau_u^{-1} \propto \omega^2\gamma^2 T\delta \big/ \overline{M} v^2$.[22] This indicates that the term is temperature dependent as well as strongly dependent on the Grüneisen parameter (γ), which relates change in lattice volume to vibrational properties of the lattice. The average atomic mass in the compound is denoted by $\overline{\mathrm{M}}$. The inverse temperature dependence of this term is why lattice thermal conductivity generally exhibits a negative linear slope with temperature in most materials. Point defect scattering features a frequency dependence of r=2. Point defect scattering can be considered due to the mass difference between an impurity and its host, as well from the strain caused by a scattering parameter (Γ).[50]

$$\tau_{pd} = \frac{\delta^3}{4\pi v^3}\omega^{-4}\Gamma \tag{2.32}$$

The term Γ is calculated by taking into account mass and volume fluctuations in the bulk. For the purposes of this thesis, a quaternary system is considered ($A_aB_bC_cD_d$). Important parameters include $\overline{M}$ and the average atomic mass on a particular site ($\overline{M}_i$), the mass of the substitution (M_i), the proportion of an atom (i=A,B,C,D) on a specific site (f_i^X, f_B^A in the case atom B on site A) and the proportion of an element in the compound (p_i, i.e. $p_A = a/\left(a+b+c+d\right)$).[51, 52]

$$\Gamma_X^M = \sum_i f_i^X\left(1-\frac{M_i}{\overline{M}_A}\right)^2 \tag{2.33}$$

To calculate the volumetric parameter (Γ^v), atomic radius of the atom on a particular site (r_i), the average atomic radius of that site ($\overline{r}_x$) and a strain parameter (ε_X) are required.

$$\Gamma_X^V = \sum_i f_i^X\varepsilon_X\left(1-\frac{r_i}{\overline{r}_X}\right)^2 \tag{2.34}$$

$$\overline{r}_X = \sum_i f_i^X r_i \tag{2.35}$$

The strain parameter is normally used as a fitting factor with typical values between 10 and 100.[51] The sum of the scattering parameter due to mass (Γ^m) and volume (Γ^v) is considered for each of the sites.[51, 52]

$$\Gamma = \sum_i p_i\left(\left[\frac{\overline{M}_i}{\overline{M}}\right]\Gamma_i^M + \Gamma_i^V\right) \tag{2.36}$$

To get a good estimate to what effect substitutions might have on the lattice thermal conductivity of the material, it is useful to look at methods developed by Klemens and Calloway and Von Bayer.[50-52] In this model, the lattice thermal conductivity ($\kappa_{L,alloy}$) of an alloy may be estimated from the unalloyed lattice thermal conductivity ($\kappa_{L,pure}$) without detailed knowledge of the Umklapp and boundary scattering processes.[50-52]

$$\kappa_{L,alloy} = \frac{\tan^{-1}(u)}{u}\kappa_{\mathrm{L,pure}} \tag{2.37a}$$

$$u = \sqrt{3\mathrm{G}\Gamma\kappa_{\mathrm{L,pure}}} \tag{2.37b}$$

$$G = \frac{\pi^2\theta_D\delta^3}{3hv^2} \tag{2.37c}$$

The mass scattering approach does not take into account that there is an ultimate limit to the minimum value for the lattice thermal conductivity. In a solid, the minimum meaningful mean free path between atoms becomes the inter-atomic spacing. Taking this fact into account, a minimum value for thermal conductivity, often called the glassy limit, can be calculated.[49]

$$\kappa_{L,\min} = \left(\frac{\pi}{6}\right)^{1/3} k_b N^{2/3} \sum_i v_i \left(\frac{T}{\theta_i}\right)^2 \int_0^{\theta_i/T} \frac{x^4 e^x}{\left(e^x - 1\right)^2} dx \tag{2.38}$$

Here the cut off temperature (θ_i) is calculated in the same manner as θ_D but using the longitudinal speed of sound (v_l) to calculate the contribution of the longitudinal branch and transverse speed of sound (v_t) to calculate the contribution of the two traverse branches. The calculated minimum lattice thermal conductivity for $Yb_{14}MnSb_{11}$ is plotted in Figure 2.6b and stays fairly constant at ~0.4 W.m^{-1}K^{-1}. This limits the maximum “allowable” total drop to 40% at room temperature. In the same graph, the 1/T behavior due to Umklapp scatter is apparent in the calculated lattice thermal conductivity and at 1100K approaches that 0.4 W.m^{-1}K^{-1} limit which is within the 25% apparent limits of this estimate as described by Cahill.[49]

It is important to note that the Debye model has important limitations since it only regards the system as having just acoustical phonons. The Debye model is most accurate in simple materials with one lattice point per unit cell. From a practical standpoint, there are 3(N-1) optical modes for every lattice point N. In $Yb_{14}MnSb_{11}$ with 104 atoms per unit cell, this yields 303 optical modes which in practical modeling are often ignored but have some contribution to the system since their group velocities are very low.[22] While efforts have been made to improve modeling of optical modes, work is continuing on developing accurate models for complex semiconductors.

When a system shows good parabolic band behavior, ZT can be successfully modeled. Assuming Umklapp scattering ($\kappa_l = \kappa_{0l}/T$), ZT may be written as:[5, 53]

$$ZT = \frac{\left[\Phi_4(\eta,b) - \eta\Phi_4(\eta,b)\right]^2}{\Phi_3(\eta,b)\left[\Phi_3(\eta,b) + C\right] - \left[\Phi_4(\eta,b)\right]^2} \tag{2.39}$$

$$C = \frac{3h^3}{8\pi\sqrt{2}(kT)^{7/2}} \frac{\kappa_{0L}}{\tau_{0ph}(m^*)^{1/2}} \tag{2.40}$$

From equation (2.39) and (2.40), assuming the acoustic phonon scattering of electrons (b=0) and for a fixed η, it can be seen that a material that has long charge carrier scattering times (or high carrier mobility values by equation (2.6) and high effective masses lead to higher ZTs. However in a system where only band structure and not physical properties change, equation (2.10) shows that τ_{0ph} has a strong $m^{*-3/2}$ dependence, meaning C in this case is proportional to m* and therefore ZT increases with lower m* values. In order to illustrate variability of η and *b*, example results of ZT versus carrier concentration using equations (2.9) through (2.11), (2.39) and (2.40) are plotted in Figure 2.7 assuming N_d=n and an arbitrary set of physical properties. An increase with lower m^* for a given temperature will optimize at lower carrier concentrations. Also, higher temperatures leads to higher ZTs but the peak is shifted to higher carrier concentrations.

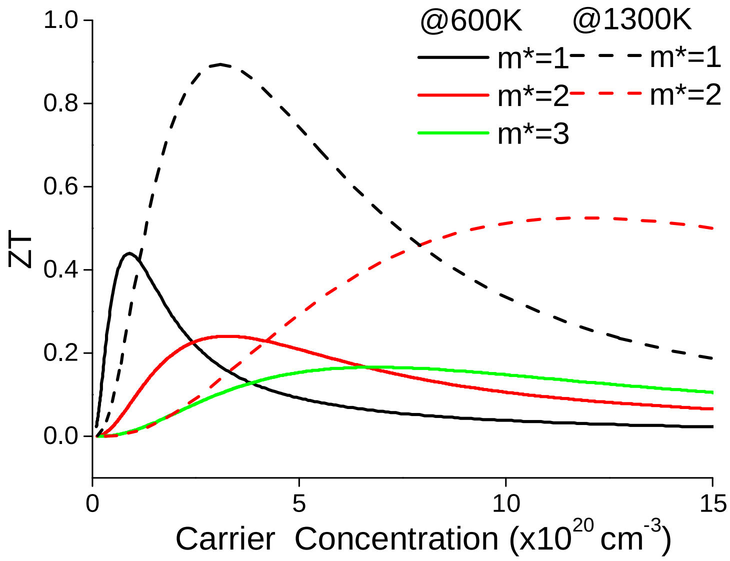

Figure 2.7. ZT versus carrier concentration for the degenerate statistics model with calculated τ_{im0} and τ_{ac0} for different values of m* and temperature.

Chapter 3: High Energy Ball Milling Synthesis of $Yb_{14}MnSb_{11}$ and Derivatives.

3.1. High Energy Ball Milling

Ball milling techniques have become one of the most popular synthetic techniques for developing thermoelectric materials.[1, 26, 54-57] It is unique because it provides a rapid low temperature route to synthesize a wide variety of materials in what is generally called mechanochemical synthesis.[58] It is a fairly new synthesis technique. In its relevance to materials, ball milling techniques which mix fine ceramic particles into metal matrixes have been commercially important since 1966.[58] It was not reported until 1989 that ball milling could be used to synthesize intermetallic compounds.[59] It was later used to synthesize rare-earth sulfides for thermoelectric materials in 1995 by Gschneidner.[60] Since then, the technique has been used in conjunction with high temperature uniaxial pressing and other consolidation techniques to synthesize a wide variety of systems such as silicides, Si-Ge alloys[26, 61], $Yb_{14}MnSb_{11}$[54], La_3Te_4[56], and filled Skutterudites[62]. Mechanochemical synthesis has been a successful synthesis method for a wide variety of thermoelectric materials.

Ball milling processes greatly speed up the rate at which solid state reactions occur. Often, in solid state reactions a product layer forms between two particles.[58] Diffusion through that product becomes slower as the reaction moves to completion, requiring high temperature and long times to ensure complete reaction. Generally in a ball milling process, that reaction layer is continuously broken by grinding, making diffusion distances much shorter.[58] The localized heating by the collision of the balls and the material is often sufficient to cause a gradual conversion of the material. A good example of this is Si-Ge alloying where the heat of formation is very low and yet alloying can occur in just a few hours.[26] Alternatively, if the reaction enthalpy is sufficiently high, a self-propagating combustion reaction may occur. As is the case with this thesis, the difference in enthalpy between a compound and its constituent elements is very large and therefore very favorable.[58] Initially in a grinding/mixing mode brittle components are milled down to small sizes and incorporated or brought into contact with ductile components. At some time, the reactants reach a small enough size that the energy of impact of the balls sets off a self-propagating combustion reaction.[58] These reactions can happen very quickly, on the order of seconds.

Although many Zintl materials were initially synthesized using a tin flux approach, this process is difficult to scale up to the production level of many hundreds of grams of material necessary to fabricate a device. Where it takes several days to produce a few grams of material from a Sn flux process, ball milling can produce hundreds of grams of material in a few hours from a single vial. Because of the reactivity of rare earths, high temperature synthesis routes such as direct reaction and vapor transport are technically challenging to scale up as well.[6] This is opposed to ball milling where the equipment is commercially available. Since there is no flux and no cleaning steps required, contamination is minimized, although some contamination from the vial and grinding media is unavoidable.[58] This process for some materials has the added benefit of creating fine grains at the micro and even nano scale.[26, 58, 61]

In mechanochemical synthesis, two primary methods are commonly used; Spex™ mixer milling and planetary ball milling. Other types of common commercial mills such as vibratory, rod and attritor, lack energies high enough to initiate reactions or sustain them at a reasonable rate.[63] Spex milling is a proprietary system developed and manufactured by Spec Certiprep Group, Inc. which uses a “figure 8” motion to shake the vial.[58, 63] This system has limited scaling potential since vials are limited to 50 ml volumes. This system is capable of developing ball impact energies of up to a Joule with a fixed rate of 1060 cycles per minute.[58, 63] This limits processing variables to vial and ball material as well as the number and size of balls in addition to the mass of the reactants. Planetary milling has the potential to allow for much larger loads, up to 500 ml, and adding variability in rotational frequency while matching the amount of energy per impact of Spex™ mills.[63] It has been demonstrated that the synthesis of several material systems can be transferred from Spex™ mills to larger planetary mill.[9]

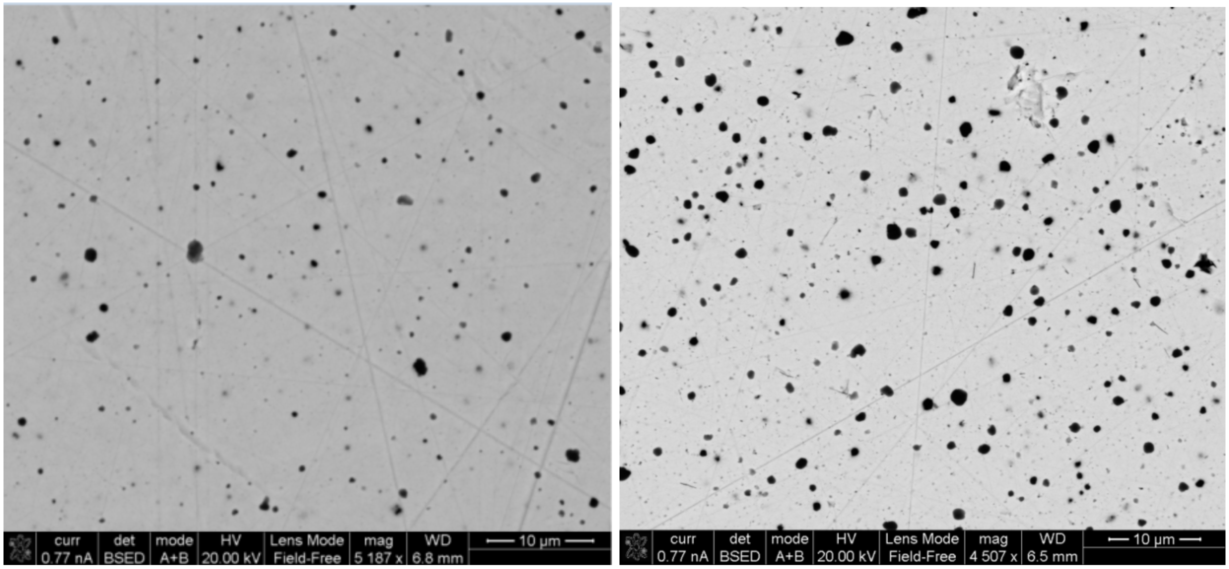

Figure 3.1. SEM micrographs of $Yb_{14}MnSb_{11}$ with sub-micron metallic inclusion formed during the initial reaction (left) and Silicide in an $Yb_{14}MnSb_{11}$ derivative with pre-synthesized particles dispersed in the bulk through ball milling (right).

Ball milling is very amenable to forming composite materials through either a forced assembly or self-assembly route. The first important use of ball milling dates back to the 1960's when it was originally used to disperse fine oxides to strengthen super-alloys.[58] This is being expanded upon to include new thermoelectric materials for improvement of both electrical properties and mechanical properties.[10] In Figure 3.1a, a micrograph is shown of a Zintl matrix with metallic inclusions which were formed in situ during the reactive milling process in a type of self-assembly process. Figure 3.1b shows a micrograph of a pre-reacted silicide which was then added to a pre-reacted Zintl and then mixed at reduced energies. Both show well distributed particles of a micrometer or less.

3.2. Conditions for Synthesis of $Yb_{14}MnSb_{11}$ and Derivatives.

In this dissertation all samples presented, except where noted, were synthesized from the elements via high energy ball milling (Spex™ 8000 mixer-mill). A visual outline of the steps in the synthesis process using the Spex™ process is illustrated Fig. 4.2. Ytterbium ingots (Alfa-Aesar, 99.9%+, rare earth oxide basis) and other rare earth metals were cut by hand after having surface oxidation removed by physical abrasion. Manganese powder (Alfa-Aesar, 99.99%, 325 mesh) and antimony shot (Alfa-Aesar, 99.999%) were used as received. The components were added in stoichiometric ratios to the compounds that were to be formed. Milling times were in the range of 30 minutes to 4 hours, with ball-to-mass ratio ranging from 1:1 to 5:1. Both stainless steel and tungsten carbide vials were used. Prior to hot pressing, all materials were handled under argon atmosphere or vacuum except for the transfer of dies from the glove box into the hot press. Consolidation of the resulting powders was done under Argon in a uniaxial hot press using high-density graphite dies at temperatures ranging from 1200 K to 1300 K. The mass density of the compacted samples was consistently in excess of 97% of the theoretical density. It was found that the powder could be left in a loaded die for tens of minutes without negatively affecting the thermoelectric properties of the pressed puck. It was also found that the formation of the final 14-1-11 phase was only completed during the hot-pressing.

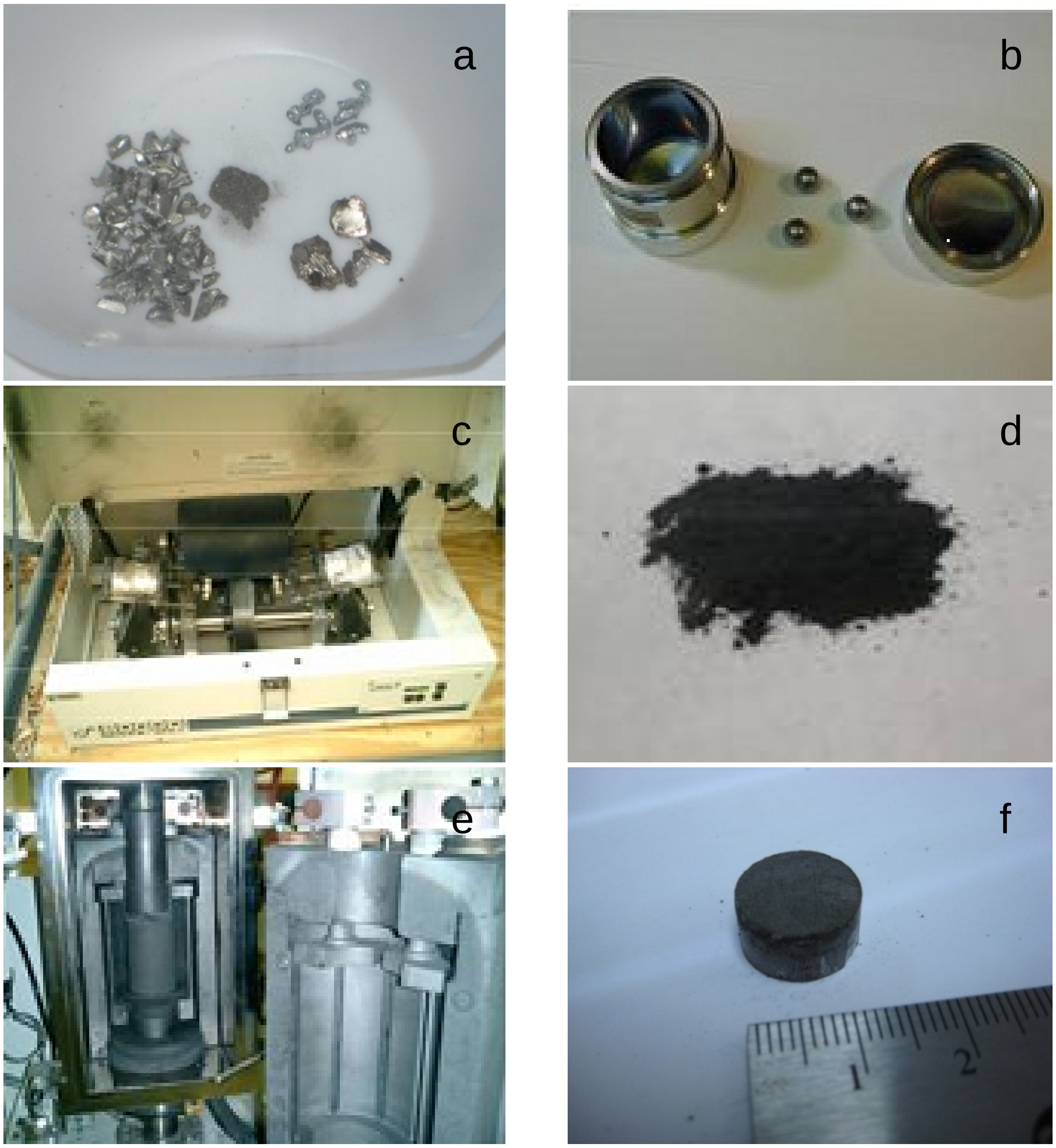

Figure 3.1. In the ball milling processes, (a) first precursors are prepared for milling and weighed. b) Materials are loaded into vials and then run in a (c) Spex™ Mixer Mill. d) The powder is then extracted in a glove box and loaded into a die. e) The die is loaded into a uniaxial hot press and then heated and cooled while pressure is applied under an inert atmosphere. f) After running in the hot, the puck resulting from the compacted powder can be then used for measurement. (Photos from Sabah Bux and Billy Li at JPL)

Chapter 4. Modifying $Yb_{14}MnSb_{11}$ by Group IV substitutions

4.1. Introduction

As discussed in Chapter 2, the wide variety of 14-1-11 compounds brings a large number of possible elements that may be used to fine tune the electrical and thermal properties of $Yb_{14}MnSb_{11}$ or to produce a compound with completely different element constituents. In approaching this search, it was useful to apply methods which have been attempted in similar complex material systems. $CoSb_3$ (Skutterudite) provides an immediate prototype to base a search for useful substitutions in the 14-1-11 system. Skutterudites have a large unit cell with 32 atoms and can be understood under the expanded Zintl-Klemm formulism which was used to describe the 14-1-11 system.[20, 64] There exists a wide variety of compounds which share a similar structure to $CoSb_3$ such as $CoAs_3$ and $CeFe_4Sb_{12}$. This family of compounds has been the object of intensive research for two decades and various strategies have been applied to maximize their thermoelectric performance.[20, 51, 62, 64]

One of the first approaches employed was alloying with isostructural binary compounds. Generally, the primary motivation for alloying is the inclusion of mass and volume defects into the crystal structure which scatter phonons. However, this approach is typically coupled with a negative effect on charge carrier mobility. Nonetheless, this approach can be successful and leads to meaningful improvement over the base material as the success of Bi_2Te_3-Sb_2Te_3 and Si-Ge alloys points out.[1, 3, 6, 26]

The theoretical model of Callaway and Von Baeyer has been successfully used to describe alloy scattering in the Skutterudite systems. This work demonstrated that substantial reductions in lattice thermal conductivity can be realized and predicted using a fairly simple model given the phonon band structure of a complex material.[20, 51] The simple result of this work was that guest atoms with larger mass and atomic radius values made for more effective scatterers even in these complex materials.[20, 51] However, it is important to note that the most common approach used to date to lower thermal conductivity of high performance Skutterudites has not been through the introduction of substitution of defects but through the introduction of interstitial "filler" ions.[9, 20, 23]

Preliminary calculations considered convenient substitutions in $Yb_{14}MnSb_{11}$ alloys with $Yb_{14}AlSb_{11}$, $Yb_{14}MnBi_{11}$, $Yb_{14}MnAs_{11}$ and $Ca_{14}MnSb_{11}$.using the Callaway and Von Baeyer model, equations (2.32) through (2.37). A Ca substitution for Y was chosen because of its chemical similarity to Ytterbium and large mass difference. For substitutions on the antimony sites, the Group V elements immediately above (As) and below (Bi) Sb were chosen. In this calculation, the volume fluctuation terms were ignored because of the complexity of the oxidation states and the ambiguity in determining the strain parameter. For $Yb_{14}MnSb_{11}$, the Debye temperature has been measured by low temperature heat capacity measurements to be 160 ± 10K.[65] The application of strain field in these complex materials becomes difficult since in complex Zintl compounds, the pnicogen atom sits on different sites so deciding on whether to use an ionic radius or covalent or some average is difficult. Figure 4.1 is a plot of modeled κ_L with alloy fraction for the various substitutions. Neglecting strain effects and at about ~300K, substitution of ytterbium with calcium yields the largest theoretical impact with a potential ~75% drop. Possible substitutions of antimony with bismuth and arsenic yield a ~50% and ~40% drop, respectively. Even though aluminum substitution of manganese represents a very small change in the mass of the compound, a ~10% drop is predicted. Hence, potentially great gains in lowering the thermal conductivity of $Yb_{14}MnSb_{11}$ seem to be achievable.

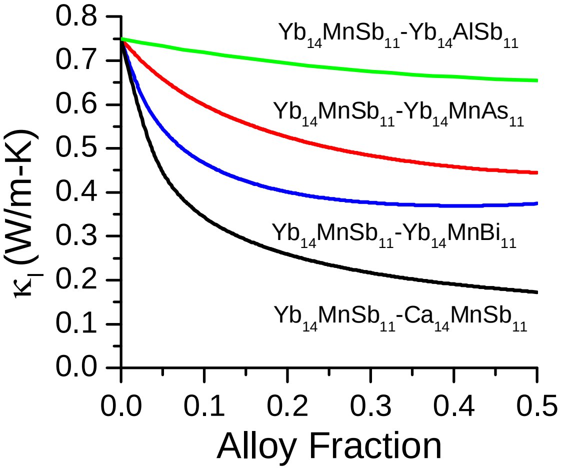

Figure 4.1. The calculated lattice thermal conductivity of $Yb_{14}MnSb_{11}$ alloyed with $Yb_{14}AlSb_{11}$, $Yb_{14}MnBi_{11}$, $Yb_{14}MnAs_{11}$ and $Ca_{14}MnSb_{11}$ using Eqs. 2.32-37c.

For comparison, it is important to note that the minimum glassy limit of $Yb_{14}MnSb_{11}$ as described by equation (2.38) was calculated to be 0.39 W/mK at room temperature. It was calculated that this limit would be reached with a 17% alloy of $Yb_{14}MnBi_{11}$ in $Yb_{14}MnSb_{11}$ using the Callaway and Von Bayer model, equations (2.32) through (2.37), assuming only mass scattering effects. For $Yb_{14}MnSb_{11-x}As_x$ substitutions the same calculation shows a reduction that remains above the glassy limit. Because of the large ionic radius difference between Sb and As, As substitution would exhibit greater scattering due to volume fluctuations which has not been taken into account due to the difficulty in determining the parameters in equation (2.34). The only attempts to modify the Group V site has been a small substitution of Sb with Te and Ge in an attempt to modify the carrier concentration in the material.[66, 67]

4.1.1. Bi Substitution

$Yb_{14}MnBi_{11}$ was first synthesized by Kauzlarich, et al. in 1998.[28] This work was focused on low temperature magnetic effects only. There have not been any studies of solid solutions of $Yb_{14}MnBi_{11}$ and $Yb_{14}MnSb_{11}$. Sb and Bi exhibit similar bonding as they are similar in electro-negativity. Also, the differences in Sb-Sb and Bi-Bi bonding distances in $Yb_{14}MnSb_{11}$ and $Yb_{14}MnBi_{11}$are small (~3% difference) which is well within the 15% suggested by the Hume-Rothery rules.[28, 68] Therefore a solid solution is expected.

In using Skutterudites as a model system, it is important to note that Skutterudites lack a bismuth analog compound.[51] Bi should serve as a better phonon scattering center with less of an effect on mobility due to the relatively close size and electro-negativity of Bi to Sb as compared to Sb and As or P.[69]

Bismuth substitution also had several additional potential benefits in addition to being a good phonon scattering defect. The addition of Bi increases both the density of the material and the potential for "softer bonding" of the material. Such bonding lowers the speed of sound which, as previously discussed, is a fundamental method for reducing thermal conductivity. Bi is also less toxic than Sb or As, and its heavy mass should increase the material's resistance to radiation damage. These factors made the exploration of $Yb_{14}MnBi_{11}$ and its alloys with $Yb_{14}MnSb_{11}$ attractive research targets.

4.1.2. As Substitution

Substitution of As for Sb in $Yb_{14}MnSb_{11}$ has not been explored. The compound $Yb_{14}MnAs_{11}$ has not been reported. $Ca_{14}MnAs_{11}$, $Sr_{14}MnAs_{11}$, and $Eu_{14}MnAs_{11}$ have all been successfully synthesized, but have only been investigated for low temperature magnetic properties.[29, 70] Even if $Yb_{14}MnAs_{11}$ does not exist, based on the relatively small differences between group V bond distance (~10%) in $Ca_{14}MnAs_{11}$ and $Ca_{14}MnSb_{11}$, some alloying should be expected even if the Yb arsenide compound is not stable.[29] As substitution also has good potential for increasing the performance of $Yb_{14}MnSb_{11}$. General trends in III-V semiconductors would suggest that the addition of As would lead to a wider band gap semiconductor.[7, 71] $Yb_{14}MnSb_{11}$ has a fairly narrow band gap of ~0.5 eV, so that at reduced carrier concentrations thermally excited carriers start to negatively impacting the ZT at high temperatures (~1000K).[27, 37, 72] A wider band gap would allow for the effect to be minimized. First principles density of states calculations done by Paul van Allmen and Trinh Vo at JPL showed that, overall, there was an increase in the calculated Seebeck coefficient for all As substitutions over that of the pure antimonide phase.[40] As previously discussed, the calculations were limited to the simpler non-rare earth-based $Ca_{14}AlPn_{11}$ system. To determine if there were any enhanced effects due to site specific substitutions, calculations were performed on the end compounds as well as for substitutions on the four unique pnicogen sites (Figure 2.5b). A large enhancement in Seebeck values was calculated in the case where As replaced all tetrahedral sites due to a spike in the density of states.[40] Therefore, the addition of As should yield increased thermoelectric efficiency provided carrier mobility values were not negatively impacted in addition to the benefits of a wider band gap material.

4.2. Experimental

4.2.1. Synthesis

$Yb_{14}Mn_1Sb_{11-1}Bi_y$ (y = 0.5, 2, 3, 4.5, 5, 6.5, 7.5 and 11) samples were synthesized from the elements via high energy ball milling using a Spex 8000 mixer-mill. Ytterbium ingots (Alfa-Aesar, 99.9%+, rare earth oxide basis) were hand cut, while manganese powder (Alfa-Aesar, 99.99%, 325 mesh), antimony shot (Alfa-Aesar, 99.999%) and bismuth chunks (Alfa-Aesar 99.999%) were used as received.

Synthesis of $Yb_{14}MnSb_{11-x}As_x$ was challenging due to the ready formation of YbAs which did not anneal out at the pressing conditions for ball milled $Yb_{14}MnSb_{11}$. The Yb in the material was pre-reacted with Sb and Mn and then As powder (Alfa-Aesar, 99.999%) was added. This limited the maximum value of x to 1 in $Yb_{14}MnSb_{11-x}As_x$. All other variables in synthesis were similar to those for $Yb_{14}MnSb_{11}$.

4.2.2. Characterization

The synthesized samples were characterized by X-ray diffraction (XRD) using a Panalytical X'Pert diffractometer. This was done on a solid fully dense puck as the reactivity of materials made powder diffraction experiments impractical. Electron microprobe analysis was done with a JEOL JXA-8200 using Bi_2S_3, FeAsS, Mn, Sb and $YbPO_4$ standards. Approximately 9 sampling points were taken for each sample and averaged. The typical analytical error was ~0.5% for Yb and Sb, ~10 % for Mn and As, and ~1% for Bi. .

Electrical resistivity and Hall carrier concentrations measurements were carried out using a four point van-der-Pauw method in a custom high temperature vacuum Hall-effect system.[73] Low Hall resistances, due the metallic behavior of the samples, lead to data spread in excess of the standard errors. The error was calculated using a linear fit of data from 400K to about 700K and then calculated from a standard deviation from the mean. Tests were done under vacuum of 10^{-5} Torr or better and Hall measurements used 100 mA current with an 8000 Gauss field. For simplification, the Hall factor was assumed to have a value of one. Small ΔT Seebeck measurements were also carried out under vacuum (>10^{-6} Torr) in a custom built system.[74] Thermal diffusivity measurements were conducted under dynamic vacuum in a Netzsch LFA 457 system using a Pyroceram standard. In previous publications the Dulong-Petit value of heat capacity had been used since the measured Debye temperature of this material is about 143K.[45] The molar heat capacity for the $Yb_{14}Mn_{1-x}Al_xSb_{11}$ series was taken from reference 27 and was assumed to be valid for the entire range for all samples. Experimental data for $Yb_{14}MnSb_{11}$ (x = 0) was provided by the Jet Propulsion Laboratory.[46]

Typical error in Hall-effect measurements is estimated to be about ~3% do to inaccuracies in the placement of the probes and errors in measuring sample thickness. Machine error due to measurement noise is typically <1% for resistivity and <5% in measuring the hall coefficient at room temperature for resistive samples (>2 mΩ-cm).[73] Error in Seebeck measurement has been measured to be practically 5%.[74] Thermal conductivity error is estimated to be ~10%. This includes uncertainty the thickness of an applied light absorbing coating, error in measurement of sample thickness and stated machine error.[74] Error in molar heat capacity is not considered. This leads to approximately a 10% error in power factor determination and a 20% error in ZT calculation.

4.3. Results and Discussion

4.3.1. Yb$_{14}$Mn$_1$Sb$_{11-y}$Bi$_y$

Figure 4.2a shows representative XRD patterns for the synthesized pucks. Calculated lattice parameters showed a good agreement (Figures 4.2b-c) with the expected values of the lattice constants using Vegard's law, using previously published values of the lattice constants for the end line compounds. There were no second phases observed in the patterns.

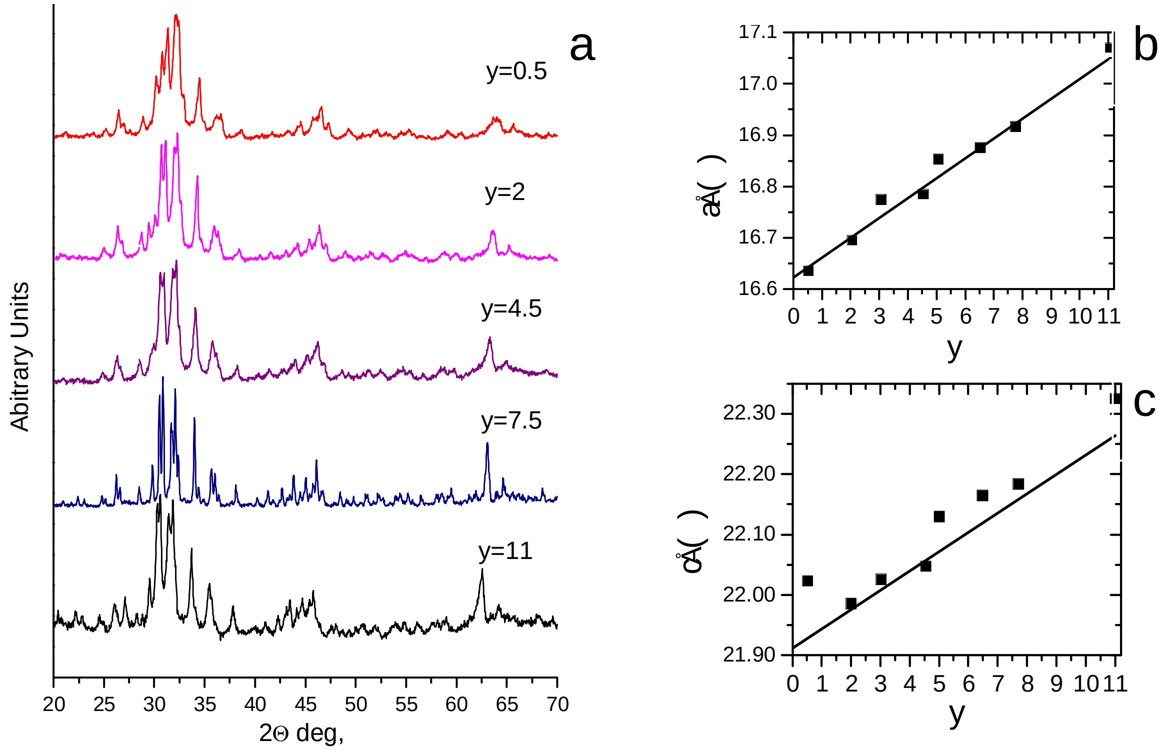

Figure 4.2. a) Representative XRD patterns of Yb$_{14}$MnSb$_{11-1}$Bi$_y$ and the calculated (b) lattice parameters a and (c) c. The tie lines represent Vegard's law for values of the lattice constants from reference 28.

The atomic compositions determined by electron microprobe analysis using known standards are shown in Table 4.1. The deviations in Yb composition from the expected values do not seem to follow a systematic trend and are likely due to the effect of surface oxidation. Back scattered electron microscope micrographs showed no obvious second phases and thus confirmed the initial XRD findings.

Table 4.1. Microprobe composition of synthesized of $Yb_{14}Mn_{1}Sb_{11-1}Bi_{y}$. Nine data points were taken per sample. Standard deviation appears in brackets.

y_{nom}	Microprobe Compositions
0	$Yb_{13.41(10)}Mn_{1.13(4)}Sb_{10.99(2)}Bi_{0.01(1)}$
0.5	$Yb_{14.39(5)}Mn_{1.09(5)}Sb_{10.46(5)}Bi_{0.53(3)}$
2.0	$Yb_{14.03(4)}Mn_{1.08(3)}Sb_{8.94(5)}Bi_{2.06(3)}$
3.0	$Yb_{13.62(5)}Mn_{1.17(5)}Sb_{7.92(5)}Bi_{3.08(5)}$
4.5	$Yb_{13.88(8)}Mn_{1.10(5)}Sb_{6.36(4)}Bi_{4.66(4)}$
5.0	$Yb_{13.99(12)}Mn_{1.08(4)}Sb_{5.84(3)}Bi_{5.16(7)}$
6.5	$Yb_{13.73(15)}Mn_{0.98(2)}Sb_{4.42(5)}Bi_{6.58(7)}$
7.5	$Yb_{13.68(9)}Mn_{1.13(4)}Sb_{3.51(5)}Bi_{7.49(7)}$
1	$Yb_{13.91(3)}Mn_{1.05(3)}Sb_{0.02(6)}Bi_{10.98(8)}$

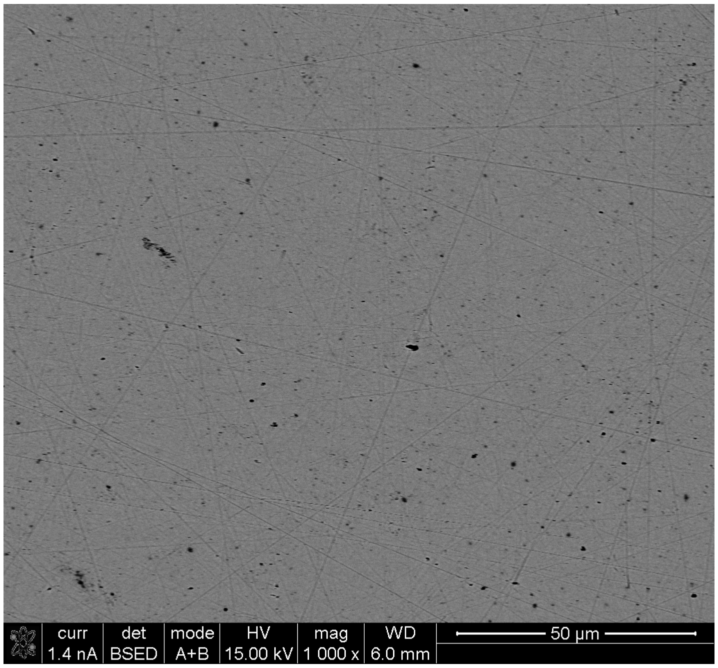

Figure 4.3. A representational SEM image of nominal y=4.5 for $Yb_{14}Mn_1Sb_{11-1}Bi_y$

Increasing Bi content (y) in $Yb_{14}Mn_1Sb_{11-1}Bi_y$ led to an increasing metallic behavior for the alloy. Room temperature (~300K) resistivity tests found that the values continuously decreased from 1.97 mΩ-cm for $Yb_{14}MnSb_{11}$ to 0.85 mΩ-cm for $Yb_{14}MnBi_{11}$, which is similar to values reported for single crystal Sn flux-grown crystals.[28] Measured electrical resistivity versus temperature curves for all the compositions synthesized are shown in Figure 4.4a. At 1173 K, the resistivity values for the end compounds were 4.72 mΩ-cm for $Yb_{14}MnSb_{11}$ and 1.2 mΩ-cm for $Yb_{14}MnBi_{11}$, confirming the room temperature trend of increased metallic transport with increasing Bi substitution. Seebeck coefficient measurements made over the same alloying range are shown in 4.4b and show a similar trend in more metallic behavior or reduced Seebeck coefficient with increasing bismuth (y) content. Neither resistivity nor Seebeck coefficient curves show turning points indicative of thermally activated mixed carrier conduction. The room temperature Seebeck coefficient showed a similar trend to that of the resistivity with room temperature values between 46 μV/K for the pure antimonide falling to about 10 μV/K for the pure Bismuth compound. At 1173K, these values rose to 180 and 70 μV/K respectively.

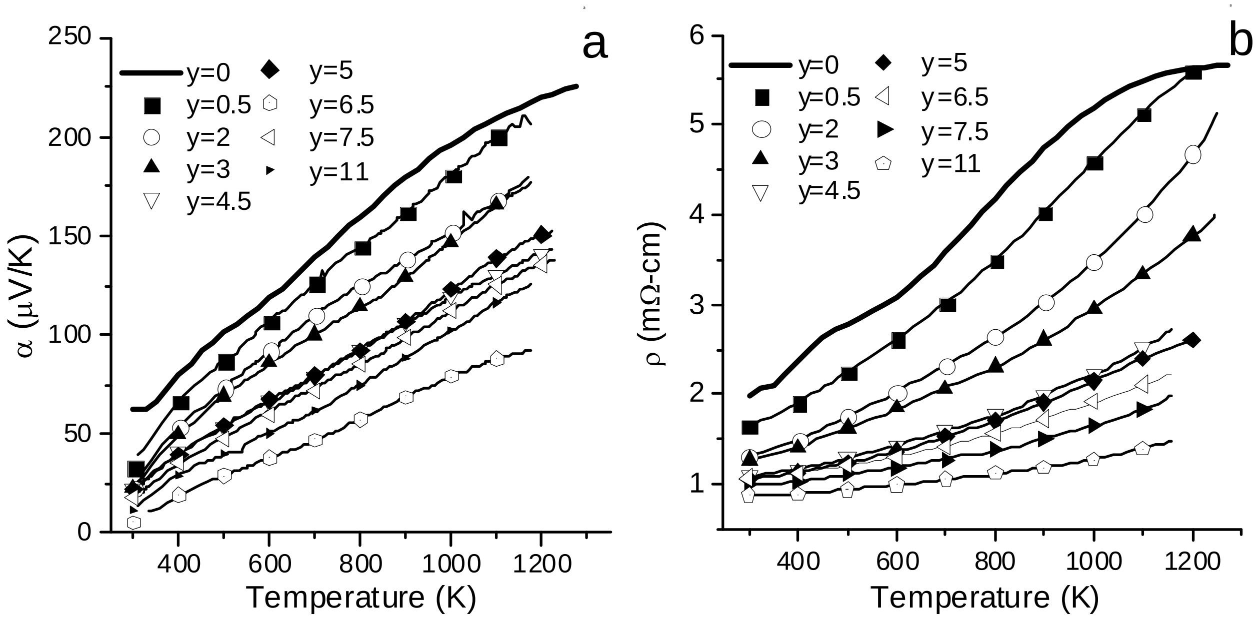

Figure 4.4. a) Resitivity (ρ) and (b) Seebeck (α) coefficient with temperature plots for $Yb_{14}Mn_{1}Sb_{11-1}Bi_{y}$ samples.

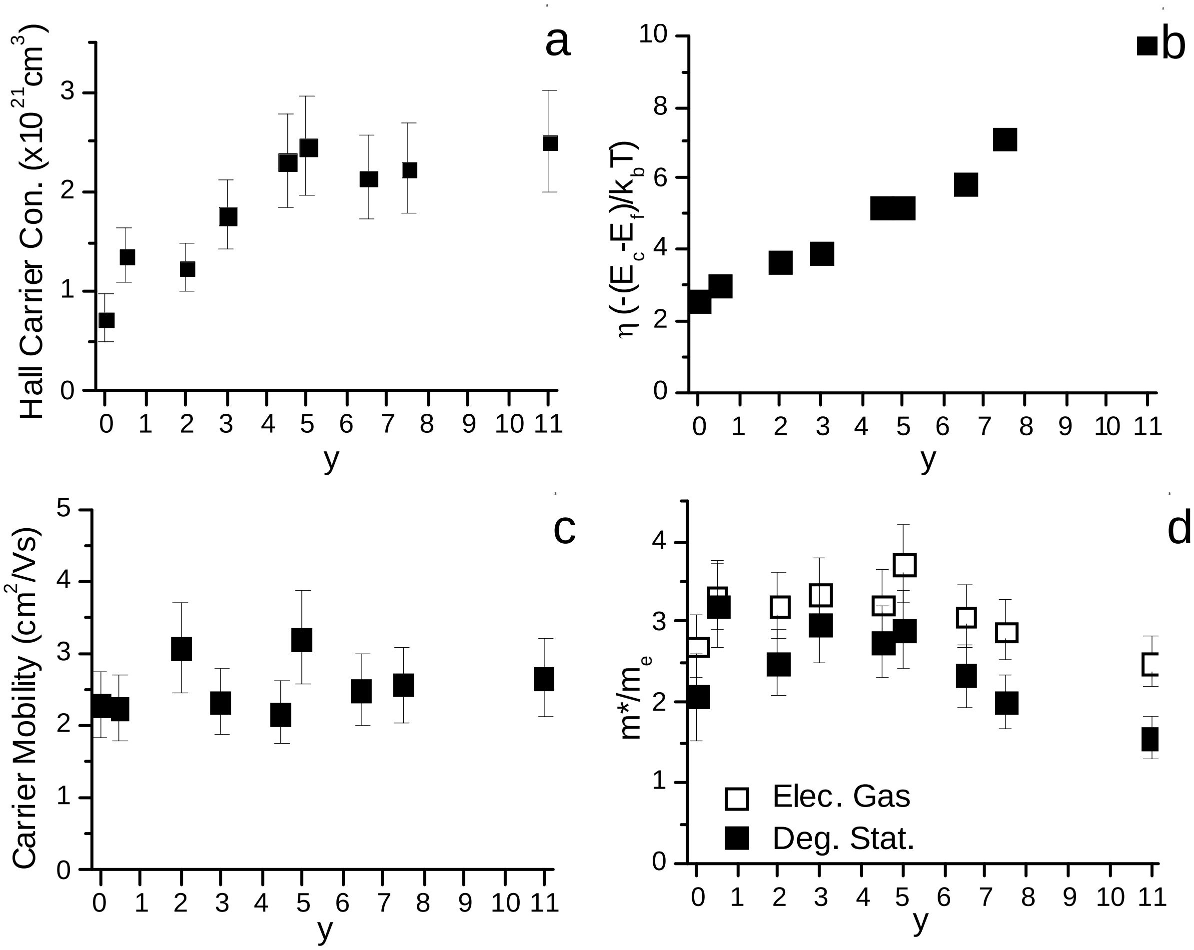

Figure 4.5. a) For $Yb_{14}Mn_1Sb_{11-1}Bi_y$, carrier concentration and (b) estimated reduced Fermi energy increased with increasing Bi content (y) while (c) carrier mobility and (d) effective mass (up to about y=5.5) stay constant with regards to y.

Figure 4.5a, shows carrier (hole) concentration for each composition at around 600K as determined from Hall measurements. The carrier concentrations increased from $0.8x10^{21}$ cm^{-3} to 2.4 $x10^{21}$ cm^{-3} as y increases. This trend contrasts with what is expected from the Zintl-Klemm concept which predicts a carrier concentration close to $1.3x10^{-21}$ cm^{-3} regardless of temperature and composition. It is possible that the extra carriers could come from Yb vacancies in this material since such defect structures have been reported.[75] However, this trend is not apparent in the microprobe compositions (below the detection limit). The presence of metallic inclusions may also cause such an anomalous behavior in Hall carrier concentration; however these inclusions have yet to be detected. In $Yb_{1-x}CaZn_2Sb_2$, it has been hypothesized that the differences in electronegativity of Yb and Ca result in a variation of carrier concentration despite being isoelectronic.[76, 77] In this case, the differences in electro-negativity between Sb and Bi are minimal making this an unlikely mechanism to explain the change in carrier concentration.[39] There could possibly be a shift from the "three center four electron" $[Bi_3]^{-7}$ to $[Bi_3]^{-6}$ where the central atom is double bonded to each end atom. However, this hypothesis runs contrary to previous first principles calculations done on $Ca_{14}MnBi_{11}$ which predicted one carrier per formula unit.[78] Valence shifts of Yb and Mn would not lead to an increase in hole concentration since they are considered to be already in their lowest oxidations states of Yb2+ and Mn^{2+} and higher oxidations states would only lead to lower carrier concentrations.[28, 79] It also stands that from trends in the periodic table of elements that compounds which have one element lower in the same group are more metallic. Despite the increase in carriers, the measured Hall mobility for this system stays at a constant value of ~2.5 cm^2/Vs (Figure 4.5c). This is consistent with what is expected from the $n^{-1/3}$ dependence of carrier mobility in a free electron gas model, as factor of 2 in carrier concentration would not dramatically impact carrier mobility if effective masses remain constant.[45]

Because of the unexpected change in carrier concentration, material parameters were estimated for the samples in order to better compare their potential performance. The reduced Fermi energy (η) was numerically calculated from the value of the Seebeck coefficient (α) at 600K using equation (2.17) for each sample. Purely acoustic phonon scattering (b=0) was assumed to be dominant as this is has been a typical assumption for other systems.[18] At 600K, the value of the reduced Fermi energy (Figure 4.5b) increases almost linearly with increasing y from a value of 2.4 for the antimonide to 10 for the bismuthide. This increase in calculated reduced chemical potential is consistent with the more metallic trends seen in higher carrier concentration and lower resistivity with increasing bismuth content (y). The effective masses for the holes in this material were calculated by two methods. The first method was applied in reference 45 for a Zintl material, using the electron gas model describe in equation (2.15b). In the second degenerate statistical approach method, equation (2.22a) and the Hall coefficient (R_H) are used to calculate m* using η calculated from α and equation (2.17). In Figure 4.5d it is shown there is reasonable agreement between the effective mass calculated using both methods which is expected as the two methods should converge at high values of reduced Fermi energies. Both models show that the effective mass remains relatively constant (~2 m_e for the degenerate statistical approach or ~3 for the free electron model) until y=~5 and then decreases to about ~1.5 m_e calculated with degenerate statistics or ~2 m_e with the electron gas model for the full Bismuth compound.

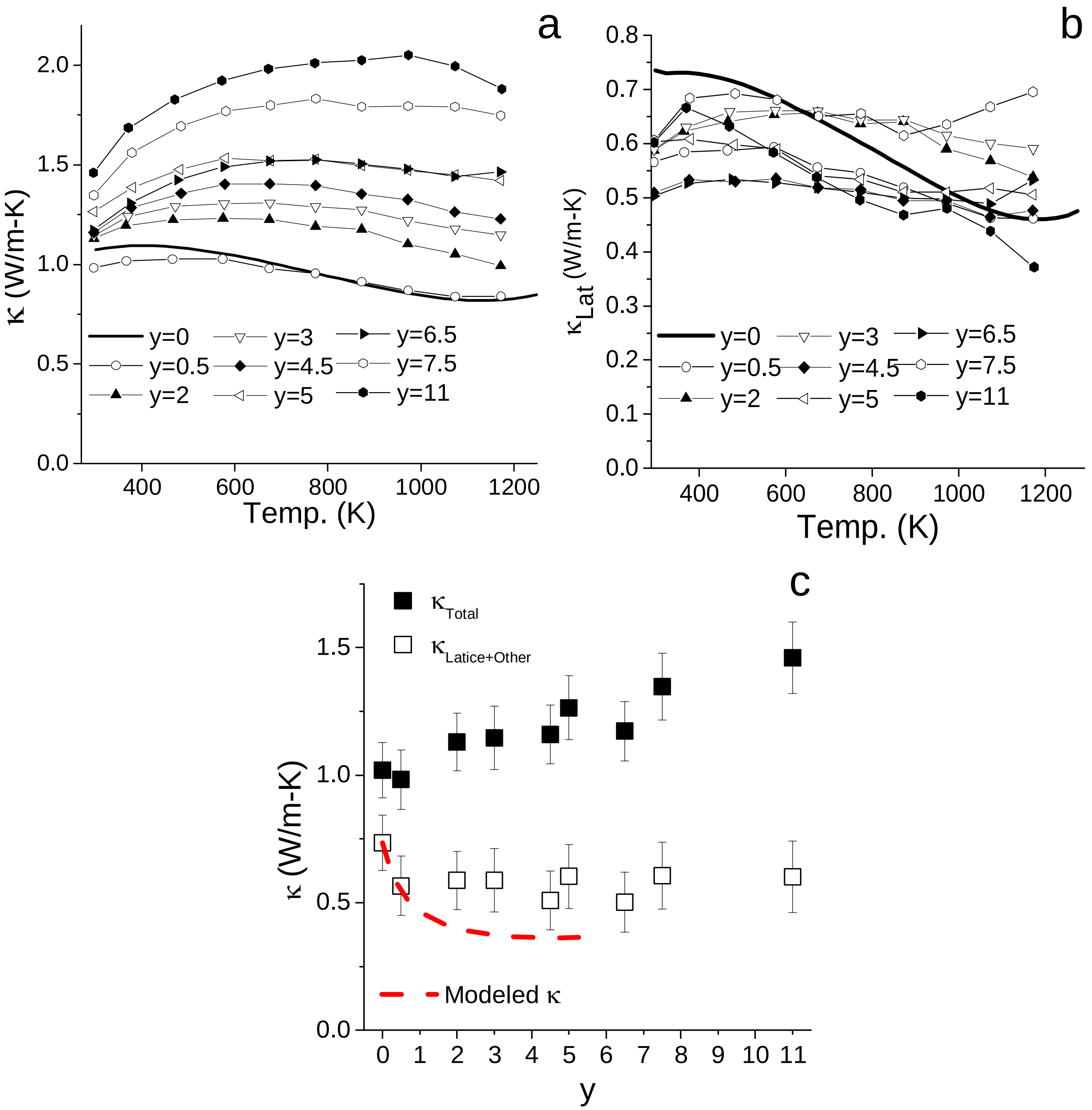

Figure 4.6. a) Total measured thermal conductivity and (b) calculated lattice thermal conductivity versus temperature of $Yb_{14}Mn_1Sb_{11-1}Bi_y$ samples. c) Measured ~300K values of total thermal conductivity, calculated lattice thermal conductivity values with error bars and theoretical Callaway-Von Bayer lattice conductivity versus Bi content (y) in $Yb_{14}Mn_1Sb_{11-1}Bi_y$ samples.

As seen in Figure 4.6a in a plot of total thermal conductivity (κ) with temperature, the total thermal conductivity displayed an increasing trend with increased Bismuth content (Figure 4.6a). This result is consistent with the corresponding decrease in electrical resistivity with increasing Bismuth content. To determine if the lattice thermal conductivity in this system decreased as predicted from increased point defect phonon scattering, κ_{lat} was estimated via the Wiedemann-Franz law. The Lorenz factor (L) was calculated using (2.24), η being calculated first from fitted values of α (Figure 4.6b) using equation (2.17). Again, the carrier scattering mechanism was assumed to be only due to acoustic phonon scattering (b=0). The κ_{lat} calculated was using fitted values of κ and is plotted versus temperature in Figure 4.6b. The values of κ_{lat} have little change compared to the dramatic increase in κ_e. In the case of $Yb_{14}MnBi_{11}$ at 1000K, the κ_e contribution is 1.5 W.m^{-1}K^{-} while in $Yb_{14}MnSb_{11}$ the contribution it is only 0.4 W.m^{-1}K^{-1} to the total. Overall, even though there is a decrease of κ_{lat} by alloying, this is more than counteracted by an increase in the electronic contribution due to the increasing metallic character of material with bismuth content.

The resulting κ_{lat} curves are consistent with an expected 1/T dependence due to Umklapp scattering. This suggests that the increase in the thermal conductivity below 600K for most samples is due to LT increasing faster than ρ. About that temperature, L saturates while the rate of increase in ρ continues leading to a decrease in thermal conductivity greater than that shown in κ_{lat}.

In Figure 4.6c, the thermal conductivity and the calculated κ_{lat} at ~300K have been plotted against y, assuming ±10% measurement error. A significant decrease in calculated κ_{lat} is observed, from 7.5 mW/cm-K to 5.0 mW/cm-K or a ~30% decrease at 300K. This is compared to a maximum decrease of ~50% calculated using the Callaway-Von Bayer model, shown in

Figure 4.6, but considerably above the glassy minimum thermal conductivity ($\kappa_{l,min}$, equation (2.38)) calculated for $Yb_{14}MnSb_{11}$of 0.39 W.m^{-1}K^{-1}.[47, 51, 52] In the Skutterudite system, both over and underestimations based on this model were observed.[51] Two samples (y=4.5 and 6.5) were calculated to have significantly lower thermal conductivity than $Yb_{14}MnSb_{11}$. In Figure 4.6b, it can be seen that for y=0.5, 2 and 7.5 above 500K, the calculated lattice thermal conductivity exceeds that of $Yb_{14}MnSb_{11,}$ but these values are not outside the expected experimental error. Other samples seem to approach the glassy limit with increasing temperature as expected. Cahill noted that his approach in determining κ_{lat} was accurate to about 25% of measured values, therefore the observed 4.8 W.m^{-1}K^{-1}floor might be the κ_{min} of $Yb_{14}MnSb_{11}$.[49] $Yb_{14}MnBi_{11}$ which does appear to reach a lower limit would be expected to have a lower κ_{min} compared to $Yb_{14}MnSb_{11}$ thanks to its higher density and likely speed of sound.

The bismuth dependence of the power factor at 600K, 900K and 1173K is shown in Figure 4.7a. Calculated data points are superimposed on the curve for 900K. A similar set of curves for ZT as a function of Bi content (y) are shown in Figure 4.7b. The power factors tended to decrease with increasing bismuth content, however this effect was not as pronounced at higher temperatures when the presence of additional carriers in the Bi-containing materials suppresses the mixed conduction effects due to thermally created carriers and leads to a power factor of .83 mWcm K^{-2} which is nearly independent of composition. Because of higher overall thermal conductivity values, the ZT decreased monotonically with bismuth content for all alloy compositions. According to equation (2.39) and (2.40), if materials parameters are minimally impacted by the addition of Bi, a gain in ZT might be made if the reduced Fermi potential could be adjusted to lower levels by counter doping.

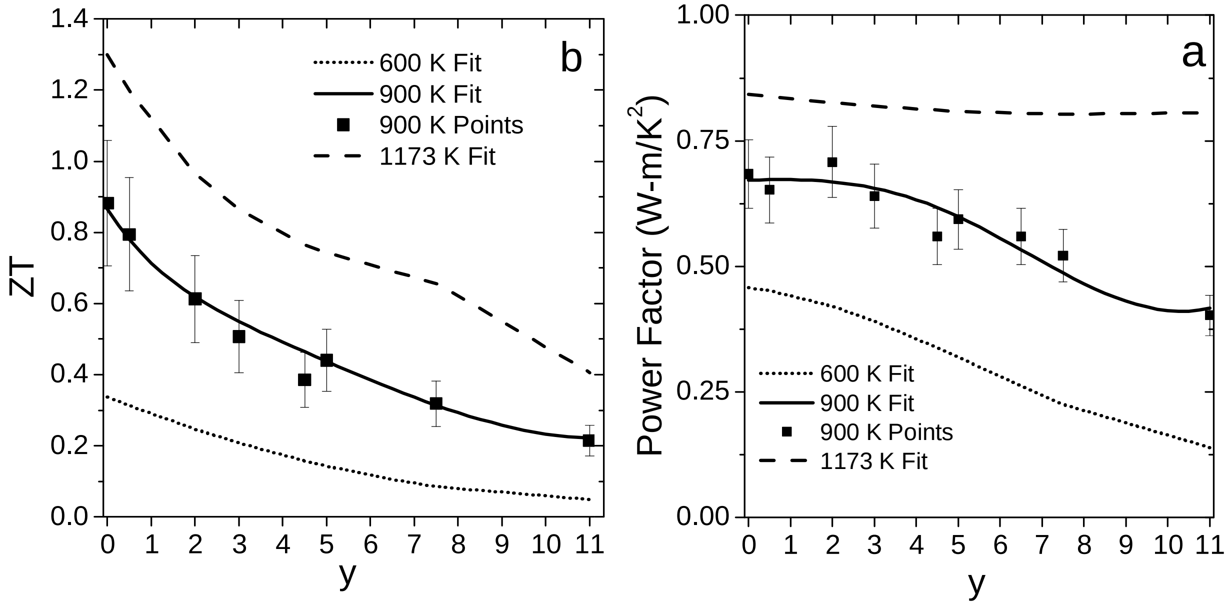

Figure 4.7. a) power factor and (b) ZT with bismuth substitution (y) at 600K, 900K and 1173K.

4.3.2. $Yb_{14}MnSb_{11-y}As_y$

Electron back scattered images showed no evidence of other phases. The sample with an as-synthesized composition of $Yb_{14}MnSb_{11}As_1$ was measured by electron microprobe to have a composition of $Yb_{13.63}Mn_{1.16}Sb_{9.98}As_{1.16}$. Lattice parameters obtained from XRD measurements on the pressed puck were determined to be 16.35Å (a) and 21.75Å (c). The XRD pattern and reference pattern for $Yb_{14}MnSb_{11}$ are shown in Figure 4.8d. Since, the end compound $Yb_{14}MnAs_{11}$ has not been synthesized, other isostructural antimonides and arsenides must be used as a guide. Between $Eu_{14}MnSb_{11}$ and $Eu_{14}MnAs_{11}$ single crystal data at 130K, the lattice showed a reduction of 5.7% along the a axis and 4.7% reduction along the c axis.[30, 70] Following Vegard's law, this would lead to $Yb_{14}MnSb_{10}As_1$ having lattice parameters of 16.53Å (a) and 21.86 Å (c) which overestimates changes in experimentally determined lattice parameters.

The electrical resistivity and Seebeck coefficient measurements obtained for the As-doped materials gave values close to those of $Yb_{14}MnSb_{11}$ as shown in Figure 4.8a. Room temperature carrier concentration was measured to be $1.5x10^{21}$ cm^{-3}, slightly higher than $1.1x10^{21}$ cm^{-3} for ball milled $Yb_{14}MnSb_{11}$ and $1.3x10^{21}$ cm^{-3} as expected from electron counting in the structure using the Zintl-Klemm formalism. The Hall mobility at 300K for the As-containing alloy was determined to be 2.0 cm^2/Vs, which is comparable to 2.3 cm^2/Vs for the antimonide. The value of the effective mass calculated using the degenerate statistics method, as outlined earlier, yielded an effective mass of $3.5m_e$ which is higher than the value of 2.4 m_e calculated for $Yb_{14}MnSb_{11}$ and closer to the value calculated from Sn flux- grown samples.[72]

Figure 4.8b shows the total thermal conductivity and the calculated lattice thermal conductivity as a function of temperature. The lattice thermal conductivity is lower for the As-substituted sample than for the pure antimonide up to 773K and then is apparently higher. However, values are within the estimated total experimental error of 10% in κ.[80] At room temperature, the κ_{lat} was calculated to be ~0.65 W/m-K. This is reasonable compared to the Callaway and Von Baeyer model (Figure 4.1), taking into account just mass fluctuations, which predicts a value of 0.57 mW/m-K, again well within the error of the measurement.[47, 51, 52] Calculated power factor and ZT as a function of temperature are shown in Figure 4.9c. There is a slight increase in the calculated power factor of $Yb_{14}MnSb_{11}As_1$ that is not significantly above the expected error of the experiment. ZT does not show any significant change and peak ZT was calculated to be 1.2 at 1200K. Above 900K, the increase in power factor over $Yb_{14}MnSb_{11}$ is offset by a higher total thermal conductivity.

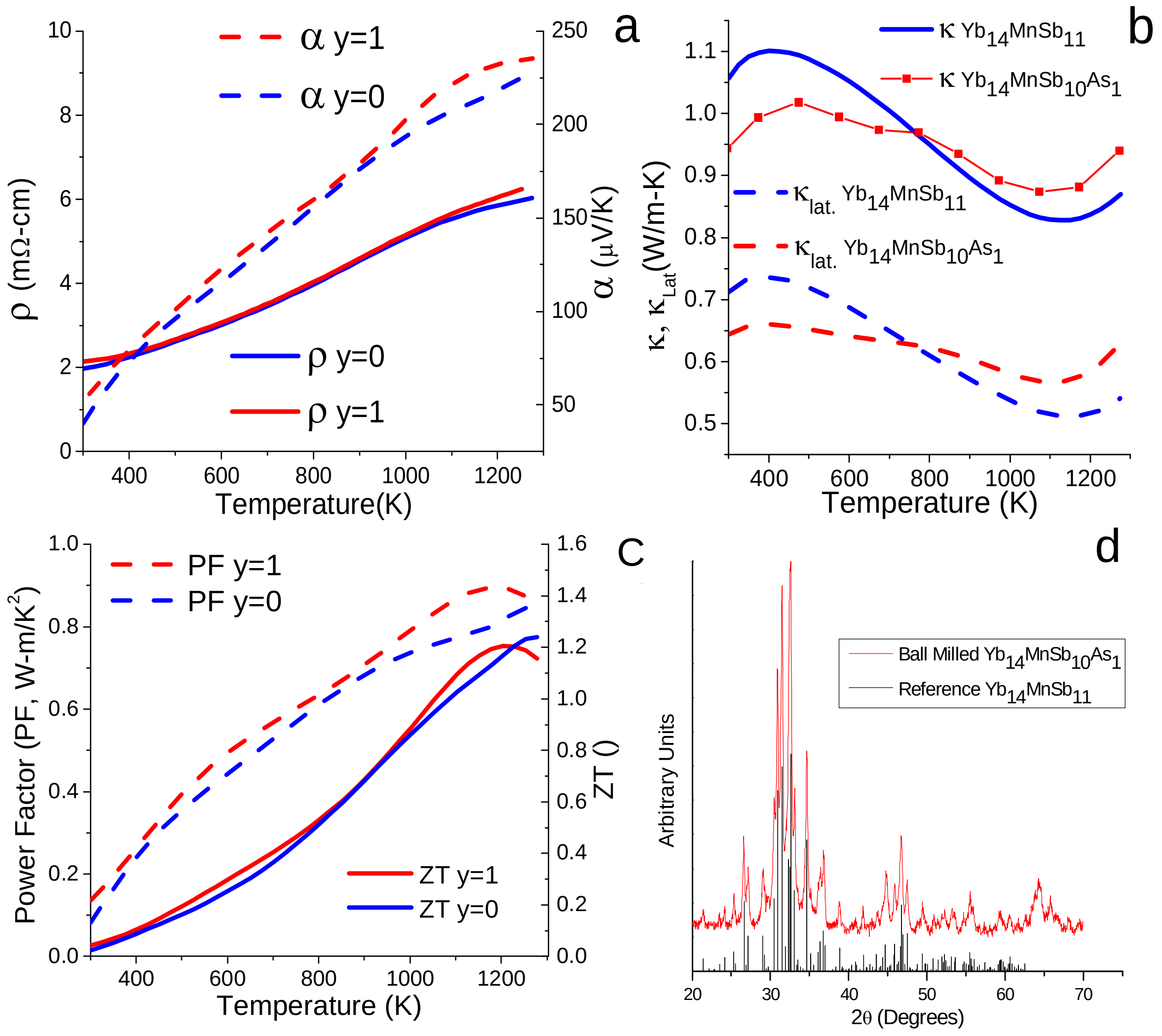

Figure 4.8. a) Resistivity(ρ) and Seebeck coefficient (α), b) Total measured thermal conductivity and calculated lattice thermal conductivity and (c) power factor (PF) and ZT versus temperature for ball milled $Yb_{14}MnSb_{10}As_1$ and $Yb_{14}MnSb_{11}$ ($Yb_{14}MnSb_{11-y}As_y$). d) XRD pattern for $Yb_{14}MnSb_{10}As_1$ with reference pattern for $Yb_{14}MnSb_{11}$.

4.4. Conclusions

A full range of alloys in the $Yb_{14}Mn_1Sb_{11-y}Bi_y$ system were synthesized using high energy ball milling techniques. Up to y=5 for $Yb_{14}Mn_1Sb_{11-y}Bi_y$. , the calculated values for carrier mobility (μ) and effective mass (m*) were similar to those observed for the pure antimonide (x=0).A significant decrease in lattice thermal conductivity, by as much as 33% of the pure antimonide value, was observed but not to the extent predicted by the Callaway and von Baeyer model, when only scattering effects due to point defect mass fluctuations were considered. Carrier concentrations were observed to increase with increasing Bi content, a departure from what the Zintl-Klemm rules predict. It is not clear if these are due to the presence of multiple bands or due to the presence of another acceptor defect. As a consequence the reductions in lattice thermal conductivity values were offset by the increased electronic contribution to the lattice thermal conductivity, and depressed the power factor due to the presence of the excess carriers. According to the predictions of a degenerate statistical model, gains in ZT can only be achieved for alloy compositions that will exhibit much lower carrier concentrations, allowing for getting the full benefit of increased point defect phonon scattering..

To start testing this approach, the $Yb_{14}MnSb_{11-y}As_y$ system, was explored. Due to a challenging synthesis, only $Yb_{14}MnSb_{10}As_{1,}$ was synthesized using the ball milling technique. The sample's measured thermal and electrical transport properties were within the error limits of the values obtained for $Yb_{14}MnSb_{11}$. This is not unexpected given that first principles calculations for $Ca_{14}Mn_1Sb_{11-y}As_y$ do not predict an increase to the Seebeck coefficient until carrier concentrations are reduced and higher As substitution levels are achieved (y equal to 4 or higher).

Chapter 5. Carrier and Band Engineering in $Yb_{14}MnSb_{11}$ and $Yb_{14}MnSb_{11-y}Bi_y$

5.1. Introduction

As described in the previous section, carrier concentration tuning is an important part of optimizing thermoelectric materials. It was found by Snyder, et al., that doping in $Yb_{14}MnSb_{11}$ can be achieved in this material with the substitution of Al on the Mn site.[27, 45] The formal charge of Mn in that site is given to be Mn^{+2} and replacing it with Al^{+3} results in the elimination of a hole from the material. Using a free electron model, they were able to model an observed 30% increase in peak ZT with an optimum hole concentration of $2.2x10^{-20}$ cm^{-3}.[45] This material was synthesized via the tin flux technique which is not practical for synthesizing materials for the production of devices.[54] JPL- synthesized $Yb_{14}MnSb_{11}$ developed for advanced RTG projects has been demonstrated to have a peak ZT of 1.2 which is higher than values for even carrier concentration optimized $Yb_{14}Mn_{1-x}Al_xSb_{11}$ synthesized through the Sn flux method.[1, 9, 46] Therefore, there is motivation to reproduce these results using a more production capable method like high energy ball milling.

In Chapter 4, alloys of $Yb_{14}MnSb_{11-1}Bi_y$ were calculated to have reduced lattice thermal conductivity values combined with minimal changes to hole mobility and effective mass up to ~y=5.5 compared to $Yb_{14}MnSb_{11}$. However, the inclusion of Bi leads to a rise in carrier concentration away from the optimal values. To move to lower carrier concentrations in this system, substitution of Yb by La or Mn by Al in $Yb_{14}MnSb_{11-1}Bi_y$ are considered. Higher ZT compositions in the quaternaries $Yb_{14}Mn_{1-x}Al_xSb_{11-1}Bi_y$ or $Yb_{14-x}La_xMnSb_{11-1}Bi_y$ might be found by modifying both thermal conductivity and carrier concentration. In this initial investigation, the value y=5.5 was selected as a starting point since it should maximize the amount of phonon-defect scattering possible as calculated in Chapter 2.

5.2. Synthesis and Characterization

5.2.1. Synthesis

Samples with nominal compositions $Yb_{14}Mn_{1-x}Al_xSb_{11}$ (x = 0.4, 0.7, 0.8, 0.95) were synthesized from the elements via high energy ball milling (Spex 8000 mixer-mill) as discussed in Chapter 3.2. Samples with nominal compositions $Yb_{14}Mn_{1-x}Al_x Bi_{5.5} Sb_{5.5}$ (x = 0.8, 0.95) and $Yb_{13.4}La_{0.6}MnBi_{5.5} Sb_{5.5}$ were also synthesized with Bi chunks (Alfa-Aesar 99.999%) and hand cut La (Alfa-Aesar, 98%+ rare earth oxide basis). Synthesis techniques were similar to those used for the pure antimonides, except that processing and measurement temperatures were reduced to avoid excess sublimation of Bi.

5.2.2. Characterization

The synthesized samples were characterized by electron microprobe analysis utilizing a JEOL JXA-8200 using Al_2O_3, Bi_2S_3, Mn, Sb and $YbPO_4$ standards. Approximately 9 sampling points were taken for each sample and averaged. The typical analytical error was ~4 % for Al, ~1% for Bi, ~10 % for Mn and ~0.5% for Sb and Yb. In previous publications, the Dulong-Petit value of heat capacity has been used since the measured Debye temperature of this material is about 143K.[45] Molar heat capacity for the $Yb_{14}Mn_{1-x}Al_xSb_{11}$ series was taken from reference 27 and was assumed to be valid for the entire range for all samples. Experimental data for high temperature Hall, Seebeck coefficient and thermal conductivity measurements for "pure" $Yb_{14}MnSb_{11}$ (x = 0) was provided by samples previously produced by the Jet Propulsion Laboratory using high energy ball milling.[46] The values for $Yb_{14}MnBi_{5.5}Sb_{5.5}$ were linearly extrapolated from the values of polynomial fits for high temperature Hall, Seebeck coefficient and thermal conductivity measurements of compositions of the compositions of $Yb_{14}MnBi_ySb_{11-y}$ of x= 4.5, 5 and 6.5 described in Chapter 4.

5.3. Results and Discussion

5.3.1. Microprobe Results

Table 5.1. Doped $Yb_{14}Mn_1Sb_{11}$and $Yb_{14}Mn_{0.6}Al_{0.4}Sb_{11}$ microprobe compositions. The typical analytical error was ~4 % for Al, ~1% for Bi, ~10 % for Mn and ~0.5% for Sb and Yb.

Nominal	Microprobe Compositions
$Yb_{14}MnSb_{11}$	$Yb_{14.08}Mn_{1.04}Sb_{10.88}$
$Yb_{14}Mn_{0.6}Al_{0.4}Sb_{11}$	$Yb_{13.98}Mn_{0.78}Al_{0.39}Sb_{10.93}$
$Yb_{14}Mn_{0.3}Al_{0.7}Sb_{11}$	$Yb_{14.03}Mn_{0.33}Al_{0.71}Sb_{10.93}$
$Yb_{14}Mn_{0.2}Al_{0.8}Sb_{11}$	$Yb_{14.10}Mn_{0.22}Al_{0.79}Sb_{10.86}$
$Yb_{14}Mn_{0.05}Al_{0.95}Sb_{11}$	$Yb_{14.12}Mn_{0.049}Al_{0.92}Sb_{10.89}$
$Yb_{14}Mn_{0.2}Al_{0.8}Bi_{5.5}Sb_{5.5}$	$Yb_{13.94}Mn_{0.26}Al_{0.80}Bi_{5.60}Sb_{5.51}$
$Yb_{14}Mn_{0.05}Al_{0.95}Bi_{5.5}Sb_{5.5}$	$Yb_{13.90}Mn_{0.061}Al_{0.94}Bi_{5.48}Sb_{5.60}$
$Yb_{13.4}La_{0.6}Mn_1Bi_{5.5}Sb_{5.5}$	$Yb_{13.27}La_{0.59}Mn_{1.16}Bi_{5.56}Sb_{5.42}$

Table 5.1 gives a summary of the samples of $Yb_{14}Mn_{1-x}Al_xSb_{11}$ (x = 0.4, 0.7, 0.8, 0.95), $Yb_{14}Mn_{1-x}Al_x$ $Bi_{5.5}$ $Sb_{5.5}$ (x = 0.8, 0.95) and $Yb_{13.4}La_{0.6}MnBi_{5.5}$ $Sb_{5.5}$ and their compositions as

determined by electron microprobe. For comparison, JPL provided a sample of $Yb_{14}MnSb_{11}$used in their Advanced Thermoelectric Converter (ATEC) Project. The microprobe composition of this sample suggests either an under counting of Sb or a deficit of Sb in the material. In light of this, microprobe compositions show good agreement with expected values and for the most part close to the microprobe's calculated measurement error. In electron backscattered images, there were no secondary phases detected. The Yb content seems to be higher with Al content because of an overlap between Yb Mα and Al Kα lines leading to an overestimate of Yb content. For Bi - containing samples, the trend of underestimating Yb content is possibly due to surface oxidation resulting from the increased reactivity of these compounds. For several samples, the Mn content was measured to exceed the 10% analytical error; this result has also been reported in previously published microprobe data on Sn flux-prepared materials of similar composition.[27]

Chapter 5.3.2. Doped $Yb_{14}MnSb_{11}$

Figure 5.1a shows, the Hall carrier concentration as a function of Al content (x) at ~ 300K. The samples show a good fit with the Zintl-Klemm formulism with each Mn yielding one free hole per Mn atom. Ball milled $Yb_{14}MnSb_{11}$ is experimentally measured to have a slightly lower than expected carrier concentration of $1.1x10^{21}cm^{-3}$ versus the predicted $1.3x10^{21}cm^{-3}$. Room temperature mobility values of lower carrier concentrations (x>0.4) samples tend to be higher than the $n^{-1/3}$ dependence fit for mobility from reference 45 for Sn flux-grown samples as shown in Figure 4.2c.

However, this picture changes at elevated temperatures as shown in figure 5.1b where carrier concentration decreases linearly in temperature in $Yb_{14}Mn_1Sb_{11}$ and $Yb_{14}Mn_{0.8}Al_{0.2}Sb_{11}$ until the effect of thermally excited carriers clearly occurs. This is contrary to the Sn flux material in which no change in carrier conductivity was reported.[45] At 600K, ball milled bulk material is measured to have a Hall carrier concentration of 8.8x10^{20}cm^{-3}. It is possible that at these higher temperatures fluctuations in the valence states of Yb^{+2} or Mn^{+2} are occurring or some other thermally activated charged defect is being formed. As previously stated, there are many examples of 14-1-11 compounds which do not follow the Zintl counting rules.[39, 81]

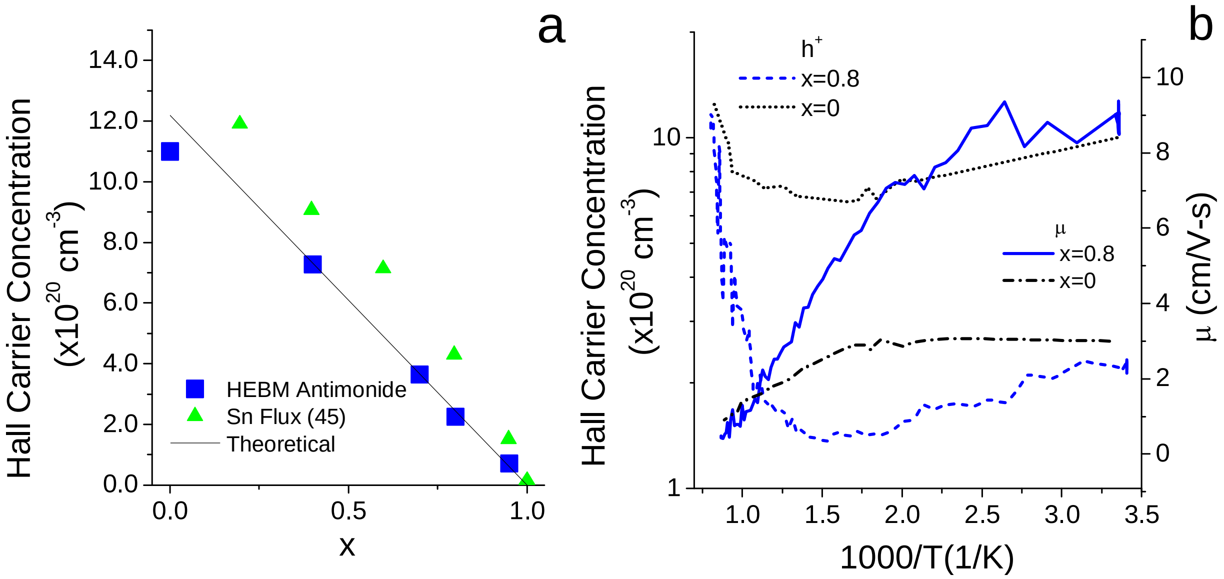

Figure **5.1.** a) Plot of measured hall carrier concentration with aluminum content (x) at 300K for high energy ball milled (HEBM) samples and published Sn Flux-grown $Yb_{14}Mn_{1-x}Al_xSb_{11}$ materials from reference 45. b) Plot of carrier concentration and mobility versus temperature in ball milled $Yb_{14}Mn_{1-x}Al_xSb_{11}$ with temperature for x=0 and 0.8.

In Figure 5.2a, electrical resistivity values are plotted versus temperature for the samples of $Yb_{14}Mn_{1-x}Al_xSb_{11}$. As expected, as carrier concentrations are reduced, electrical resistivity values keep on increasing. At high temperature (> 900 K), the resistivity values decrease with temperature due to the effect of thermally activated charge carrier pairs, with the peak in resistivity values shifting to lower temperatures for increased Al content and decreased carrier concentration. In Figure 5.3b, Seebeck coefficient values are plotted versus temperature with similarly increasing values and lower turnover temperatures with increasing Al content. A simple analysis of the relative simultaneous changes in Seebeck and electrical resistivity values compared with the baseline pure antimonide shows that these changes are indeed reasonably consistent with the observed variations in carrier concentration, except perhaps at the highest Al concentrations,, implying that no major changes in electronic band structure are involved. Moreover, an estimation of the band gap of a material may be written as a function of α_{max} and T_{max} which are the maximum Seebeck (α_{max}) and the temperature (T_{max}) at which that maximum occurs.[35, 45, 82]

$$E_g = 2e\alpha_{\max}T_{\max} \tag{4.3}$$

As shown in Figure 5.3b, the ball milled material has an average band gap of about 0.6 eV. This is fairly consistent with the Sn flux-grown material which has a slightly lower band gap 0.5 eV. In both cases, the band gap seems to be independent of aluminum content, confirming the combined Seebeck and resistivity transport analysis.[45]

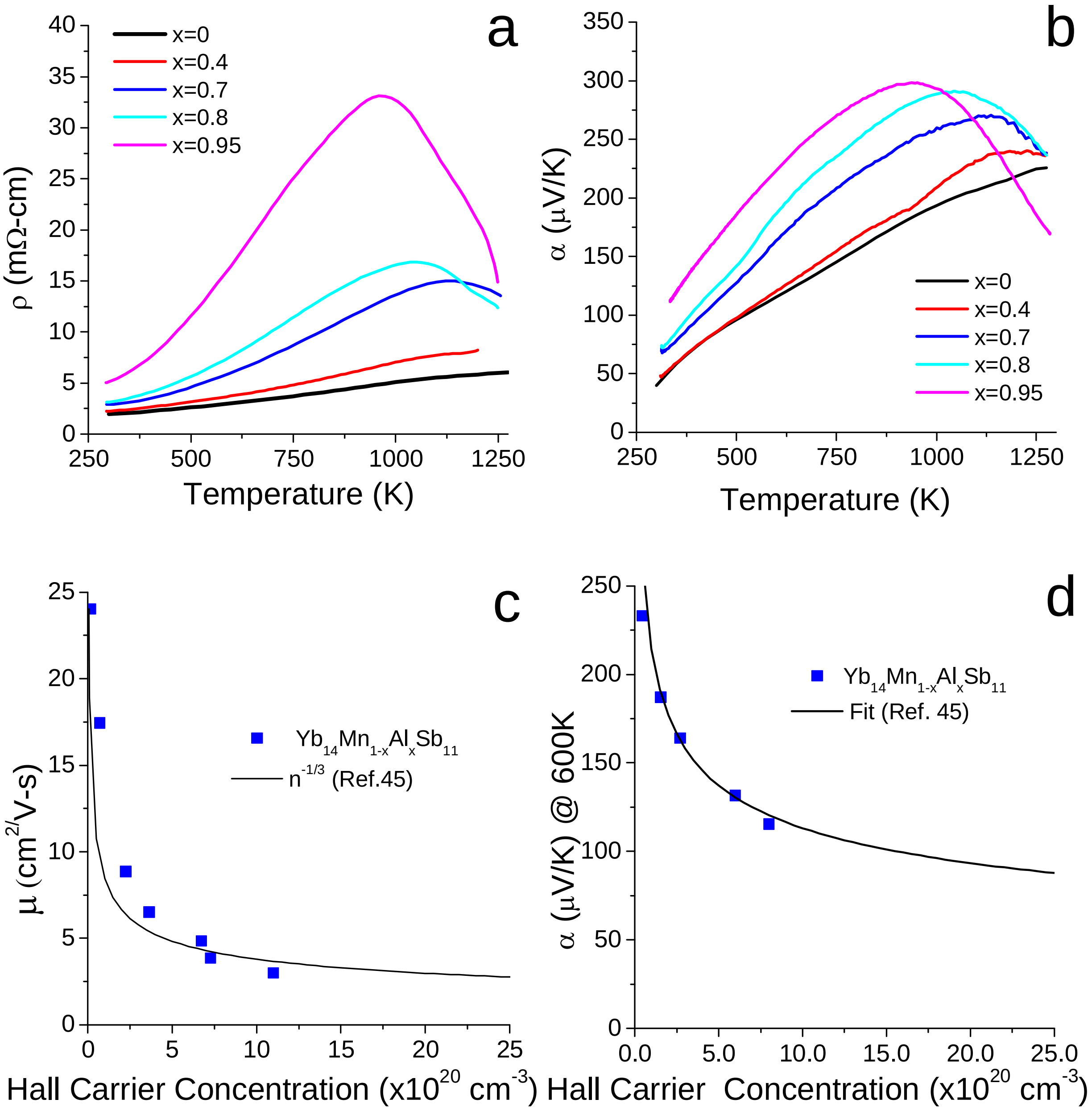

Figure 5.2. Plot of (a) resistivity and (b) Seebeck coeficient in regards to temperature for $Yb_{14}Mn_{1-x}Al_xSb_{11}$. c) Mobility versus carrier curve for $Yb_{14}Mn_{1-x}Al_xSb_{11}$ at ~300K with a fit line from reference 45. d) A Pisarenko curve at 600K for $Yb_{14}Mn_{1-x}Al_xSb_{11}$ with a fit line from reference 45.

In order to use the degenerate statistical approach to model the system, an estimation of the relative magnitudes of the acoustic phonon (τ_{ac0}) and impurity (τ_{im0}) carrier scattering times at the band edge should be made. This can be done by using equations (2.10) and (2.11). The speed of sound and density for $Yb_{14}Mn_1Sb_{11}$ have been measured to be 1970 m.s^{-1}[46] and 8.367 g.cm^{-3}.[28] Carrier effective mass values have been determined by various methods to range between 3 m_e[72] and 17.4 m_e[83]. The deformation potential (E_{def}) is normally on the order of a few eV ranging from ~10 eV for Si[84] to 3 eV for Bi_2Te_3. Since E_{def} is related to the stiffness in the material and therefore speed of sound, $Yb_{14}Mn_1Sb_{11}$ is assumed to fall into that range.[10, 85] For impurity scattering, it is assumed that scattering centers are equal to the number of carriers. Since, there are no DC dielectric permittivity measurements published, a range between $10\varepsilon_o$ to $100\varepsilon_o$ is assumed. Fitting for resistivity, Seebeck coefficient and carrier concentration between 500 and 700K and combining equation (2.17), (2.20) and (2.21) gave values of $m^*=\sim 2\ m_e$, $\varepsilon_{DC} = 30\ \varepsilon_o$ and $E_{def} = 5$ eV. At 500K, this leads to b=0.83 and at 700K this gives b=0.22 which validates the assumption that acoustic phonon scattering is dominant in this material at high temperatures (T>700K). These values for ε_{DC} and E_{def} were then used to estimate the effective masses of the other samples (Figure 5.3a). For comparison, effective mass values calculated with Eqs. 2.15a and 2. 5b are also shown as well as the published effective masses from reference 72 using equation (2.15b) for Sn flux-grown materials. These effective masses are in good agreement with one another except that the effective mass calculated from the slope of the Seebeck coefficient, equation (2. 15b), was offset higher than either the electron gas approximation method or the degenerate statistical method via a single point Seebeck coefficient. The Sn flux-grown $Yb_{14}MnSb_{11}$ material was calculated to have a higher effective mass (of $m^*=\sim 3m_e$) compared with that of the ball milled material ($m^*=\sim 2.5m_e$). Overall, the ball milled material showed a gradual decrease in measured effective mass regardless of the method of calculation as opposed to the sharp drop for materials with Al content x>0.8 as seen in Figure 5.3a.

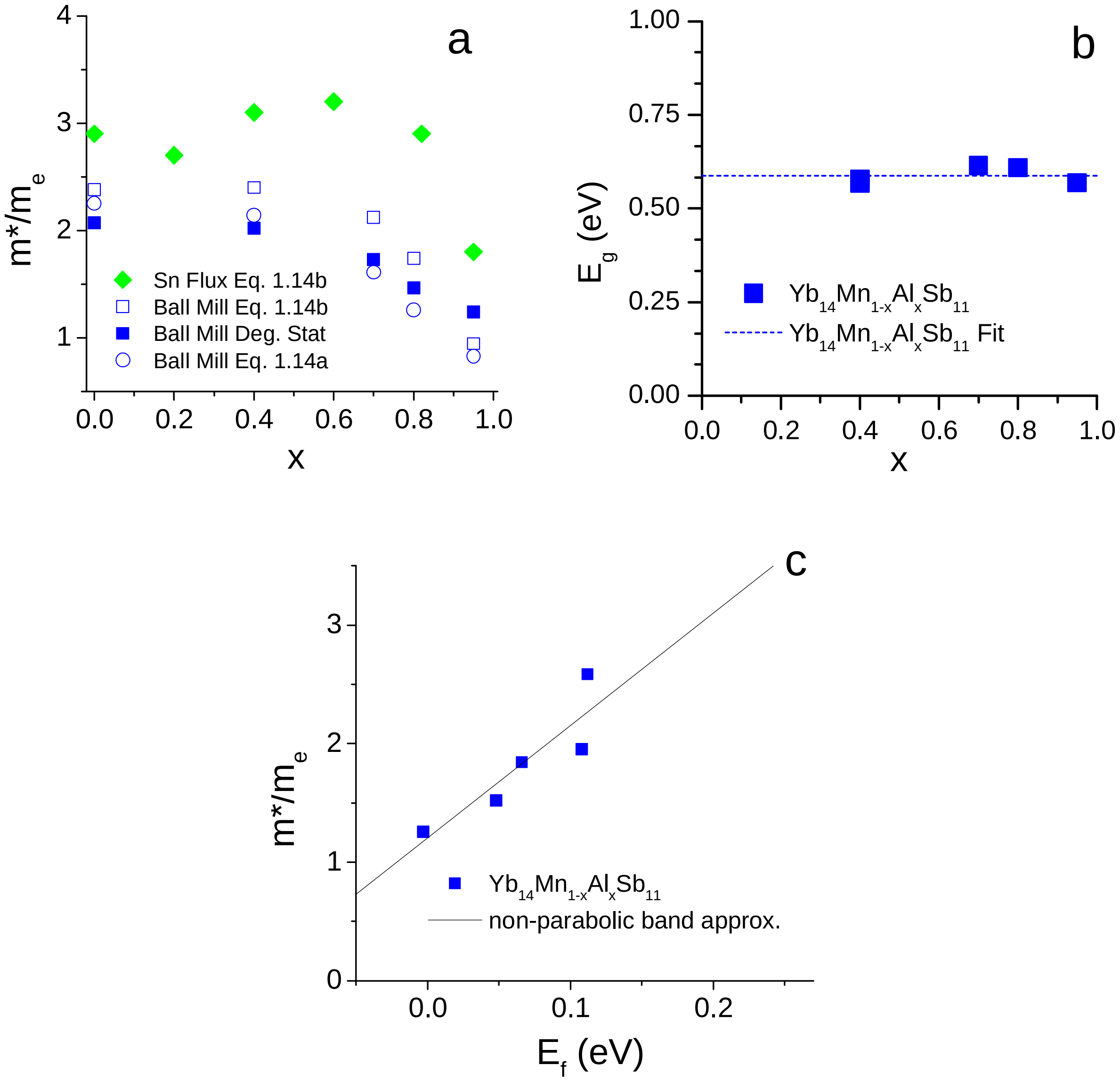

Figure 5.3. a) Effective masses for $Yb_{14}Mn_{1-x}Al_xSb_{11}$ using equations (2.15a) and (2.15b) as well as the degenerate statistical approach assuming only phonon-electron scattering. Also plotted are effective masses for Sn flux grown $Yb_{14}Mn_{1-x}Al_xSb_{11}$ from reference 45 using equation (2.15a). b)Band gaps calculated from peak Seebeck coefficient values for $Yb_{14}Mn_{1-x}Al_xSb_{11}$. c) Calculated effective mass for $Yb_{14}Mn_{1-x}Al_xSb_{11}$ samples versus calculated Fermi energy including the linear fit for calculating non-parabolic band bending parameters.

The apparent change in m* has two possible sources which might be explained by multiple band effects or non-parabolic band structure. Band calculations for $Ca_{14}Mn_1Bi_{11}$ clearly showed the presence of a single band close to the top of the main valence band and then several bands ~0.5 eV away from the band edge.[78] As $Ca_{14}Mn_1Bi_{11}$ is a semi-metal, the Fermi level was calculated to be below the edges of these other bands and some multi-band effects might be expected. As this is a narrow band gap semiconductor, it might be assumed here that non-parabolic behavior is responsible for this apparent effect. For an initial top of the band m*, wave vector (k), energy level (E) and a set of band bending parameters (a, b, etc.), non-parabolicity of the band can expressed as:[86, 87]

$$E(1+aE+bE^2+...)=\frac{\hbar^2 k}{2m_0^*} \tag{5.1}$$

It can be shown using first order approximation of the band bending parameters, that the apparent effective mass can be estimated as:[87]

$$m^*=m_0^*(1+\frac{10}{3}aE) \tag{5.2}$$

Values are typically on the order of the inverse of the band gap of the material. For example, silicon has a value of *a* about 0.6 eV^{-1} and an inverse band gap of 0.9 eV^{-1}.[87] Figure 4.3c show a good linear fit to the calculated effective mass values and the Fermi energy. From this fit m_0* was calculated to have a value of 1.24m_e and the band bending parameter was calculated to be 2 eV^{-1}. This is reasonable compared to the inverse of the estimated thermal band gap as calculated here from equation (5.1) to be 1.7 eV^{-1}.

With values available to more accurately describe the system, the hall constant (r_h) was calculated to determine its effect on the hall carrier concentration using equation (2.22b). Using the estimated values of scattering times in equations (2.10) and (2.11) and η as determined from the Seebeck coefficient and equation (2.17), the values were calculated to be r_h=1.095 at 300K and r_h=1.02 at 500K. While not insignificant, this is not enough to explain this ~20% drop in carrier concentration to 8.8x10^{20}cm^{-3} at 500K from 1.1x10^{21}cm^{-3} at 300K.

Figure 5.4a shows the temperature dependence of the total thermal conductivity for the $Yb_{14}Mn_{1-x}$ Al_xSb_{11}samples. Thermal conductivity values increasingly drop at room temperature with increased Al content. Also apparent is the tail at high temperatures due to the increase of the bipolar term resulting from thermally activated charge carrier pairs. Using the Wiedemann-Franz law and assuming acoustic phonon scattering (b=0) to calculate the Lorenz number (L), equation (2.24), and then the electronic contribution to the total thermal conductivity, lattice thermal conductivity values were estimated. Figure 4.3b shows the results of the lattice thermal conductivity as a function of temperature for the samples after the electronic contribution has been subtracted. The drop in lattice thermal conductivity shows a 1/T dependency as expect. LT/ρ is approximately constant, total thermal conductivity decrease is due to Umklapp scattering. At high temperatures and for low carrier samples, bipolar effects arise due to increased mixed conduction, leading to a sharp apparent increase in the calculated lattice thermal conductivity. [27, 45, 72] Calculated lattice thermal conductivity decreased at room temperature with increased aluminum content which is significant compared to the assumed 10% inherent error. For x=0.95, the calculated lattice thermal conductivity actually approaches the glassy minimum value of 0.39 W.m^{-1}K^{-1} which is lower than the minimum of ~0.5 W.m^{-1}K^{-1} which was found for $Yb_{14}MnSb_{11-y}Bi_y$. It is important to note that for the x=0.95 sample, because of a negligible contribution to the electronic contribution, the total thermal conductivity approaches this value until the bipolar term become apparent around 900K. (Figure 5.4b) However, this reduction is unexpected since $Yb_{14}AlSb_{11}$ is expected to have more ionic bonding overall, which should increase the speed of sound and Debye temperature and therefore lead to higher thermal conductivity than $Yb_{14}MnSb_{11}$. Comparison to Sn Flux synthesized materials is impractical as a fixed L was used to calculate lead to values for κ_{lat} which are unreasonably low compared to the calculated glassy minimum.[45] The reason for this unexpected result is unclear but could be due to several factors. At 500K, the variation of L between that calculated using only acoustic phonon scattering and the mixed scattering value previously calculated for $Yb_{14}MnSb_{11}$ with b=0.8, is less than 5% so this is not a likely source for the observed effect. However, this approach does not take into account non-charged scattering mechanism and which may affect the value of L. Point defect phonon scattering effects due to replacing Mn with Al are only projected to give a modest reduction of ~0.5 $W.m^{-1}K^{-1}$ units (Figure 4.1) without taking into account volume fluctuation effects. However, for $x>0.7$, thermal conductivity decreases as composition gets closer to the end point composition which is the opposite behavior from the "bath tub" trend which is predicted. Besides point defect scattering, other scattering modes could be enhanced. As the material gets increasingly less metallic, it becomes more brittle and that could lead to a finer microstructure which more effectively scatters certain frequencies not scattered by alloys.[58, 62] Also, the more ionic Al-Sb bonding might similarly tune the rattling frequencies of the Sb tetrahedral to better scatter un-scattered frequencies of phonons as well. There is also some uncertainty in the determination of the heat capacity of these samples. Laser flash diffusivity requires an accurate determination of heat capacity while the electronic thermal conductivity is calculated independently of heat capacity. If the heat capacity is not correctly determined, scaling issues in the resulting κ_{lat} terms will occur. .

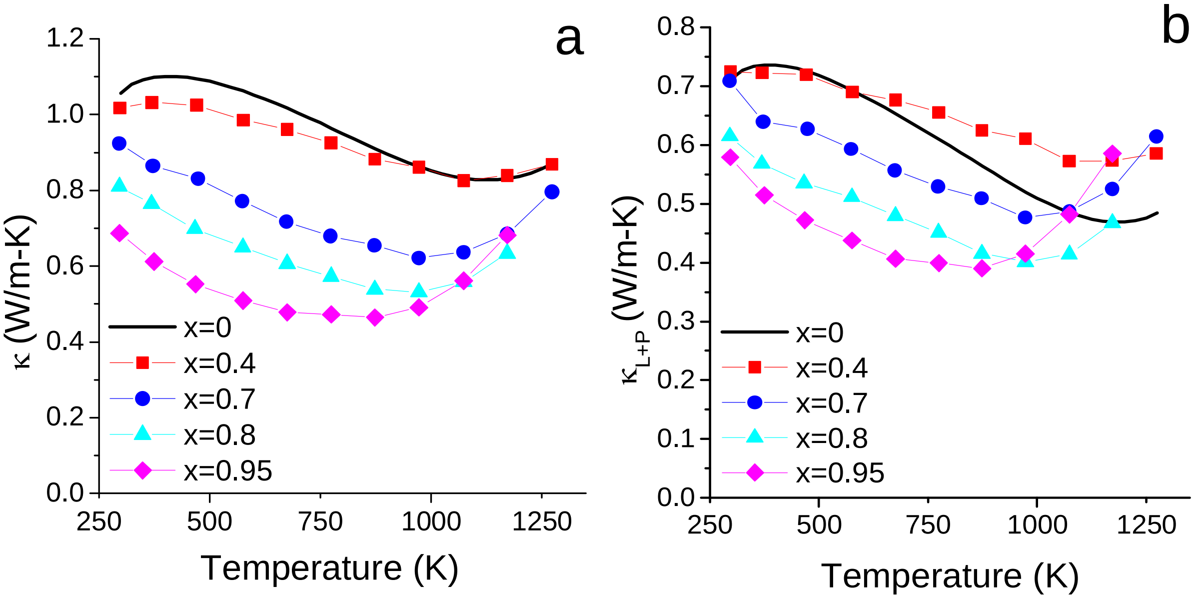

Figure 5.4. a)Total lattice thermal conductivity and thermal conductivity with electronic term versus temperature for $Yb_{14}Mn_{1-x}Al_xSb_{11}$ using molar heat capacity from reference 27.

Figure 5.5a plots power factor versus temperature for the ball milled $Yb_{14}Mn_{1-x}Al_xSb_{11}$ samples. Except for the lowest carrier concentration (x=0.95) below 500K, there is no improvement in power factor over $Yb_{14}Mn_1Sb_{11}$. At higher temperatures, power factor is negatively impacted by mixed conduction. As illustrated in Figure 4.4c, the power factors for ball milled and Sn flux-grown samples of x=0 show a similar temperature dependence, however the Sn flux material does not seem to be as impacted by thermally created carriers at higher temperatures. Figure 5.5b shows the high temperature ZT curves for the ball milled $Yb_{14}Mn_{1-x}Al_xSb_{11}$ samples. The peak ZT for this material did not increase. For x=0.8 and 0.95, there was some improvement in ZT over $Yb_{14}Mn_1Sb_{11}$ below 1000K. In Figure 4.4d, the ZT curves of $Yb_{14}Mn_2Al_{0.8}Sb_{11}$ for ball milled and Sn flux-grown material from reference 45 as well as ball milled $Yb_{14}Mn_1Sb_{11}$ are plotted. For $Yb_{14}Mn_2Al_{0.8}Sb_{11}$ synthesized through both methods, there was very good agreement up to 1000K in ZT values. Above 1000K, the Sn flux synthesized material's ZT out performs the ball milled material due to a degraded power factor as shown in Figure 5.5c. However, this Sn flux sample does not improve upon the baseline ball milled "pure" $Yb_{14}MnSb_{11}$ which has a higher ZT.[45]

A possible source in the discrepancy in performance between ball milled and Sn flux-synthesized $Yb_{14}Mn_{1-x}Al_xSb_{11}$ samples is the presence of secondary phases. Some metallic Sn has been shown to remain in pellets made from Sn Flux grown $Yb_{14}Mn_{1-x}Al_xSb_{11}$ samples.[27] While Sn has not been shown to be present in the bulk 14-1-11 phases, solubility into the structure improve at higher temperatures. If Sn substituted for Sb, Sn having one fewer electron would be a p-type dopant. In the case of $Yb_{14}Mn_2Al_{0.8}Sb_{11}$, Sn p-type doping counteracts the effect of thermally produced carrier pairs and leads to improved power factor. In the case of $Yb_{14}MnSb_{11,}$ extra carriers would shift the carrier concentration further away from the optimal level. This is in addition to the deleterious effects of having a metallic element negatively impart overall ZT.[88] Furthermore, all the room temperature Seebeck coefficient values appear to intercept each other at 300K at around 46 μV/K in the Sn Flux synthesized samples.[45] For ball milled materials the expected trend is more apparent, the Seebeck coefficient increases from 46 μV/K for x=0 to 115 μV/K for x=0.95 at 300K. However, at 600K both systems appears to be a good fit for the Seebeck coefficient Pisarenko curve (Figure 5.2b) calculated according to equation (2.15).[45] The uptake of metallic Sn into the Zintl phase may help explain that trend since at low temperatures a metal-semiconductor composite will have reduced α values compared to the semiconductor.[88] It also has been reported that $Yb_{14}MnSb_{11}$ is capable of some degree of nonstoichiometry so that this uptake of Sn might not lead to a loss of Sb.[89]

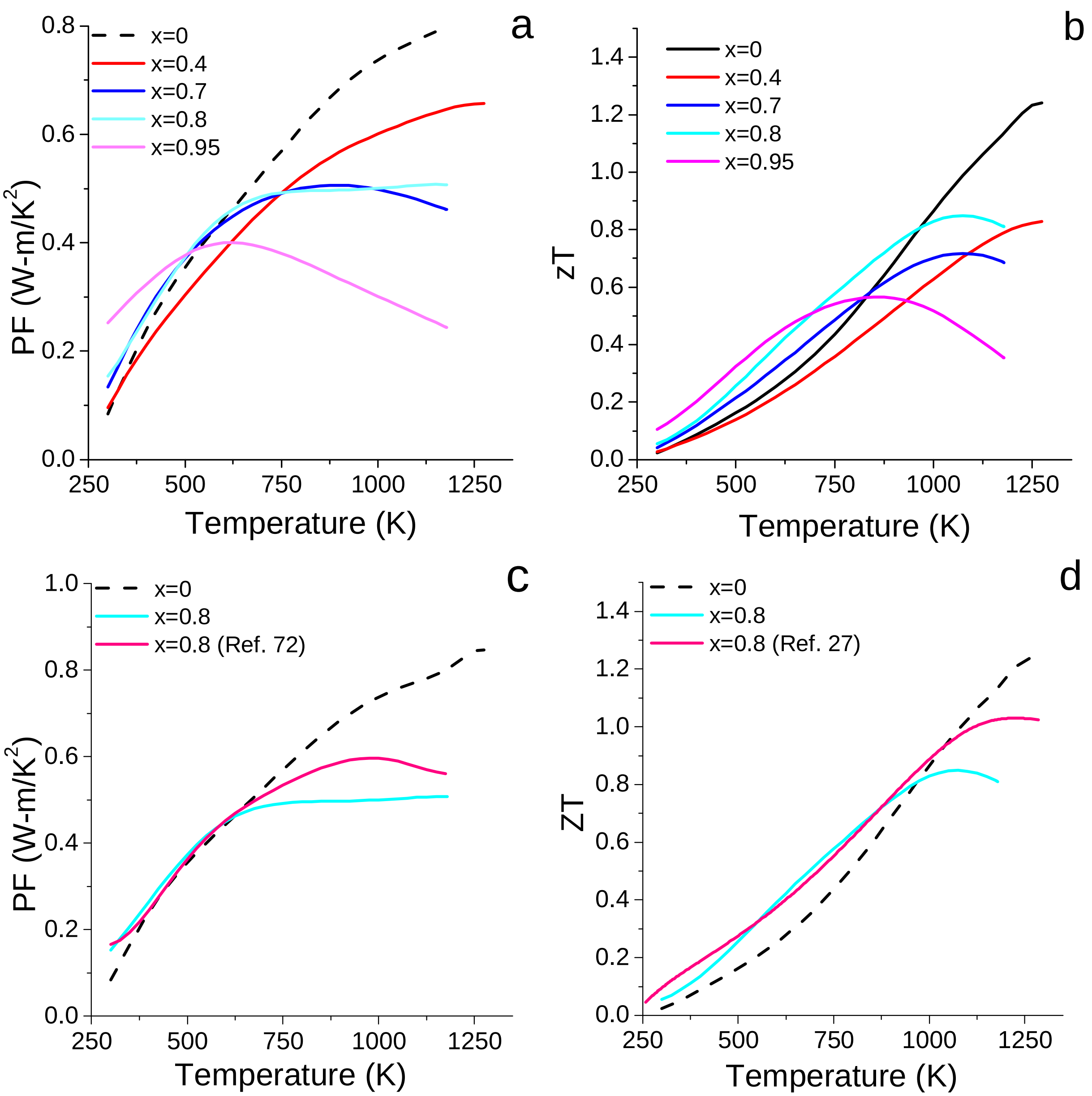

Figure 5.5. a) Power factor and (b) ZT versus temperature curves for ball milled $Yb_{14}Mn_{1-x}Al_xSb_{11}$. c) Power factor and (d) zT versus temperature curves for ball milled and Sn Flux $Yb_{14}Mn_{0.2}Al_{0.}8Sb11$ from references 72 and 27 respectively and ball milled $Yb_{14}Mn_1Sb_{11}$.

5.3.3. Doped $Yb_{14}MnBi_{5.5}$ $Sb_{5.5}$

The same methods of analysis applied to $Yb_{14}Mn_{1-x}Al_xSb_{11}$ were used for doped $Yb_{14}Mn_1Bi_{5.5}$ $Sb_{5.5}$. The Hall carrier concentration as a function of x is shown for $Yb_{14}Mn_{1-x}Al_xBi_{5.5}Sb_{5.5}$ and $Yb_{14-x}La_xMnBi_{5.5}Sb_{5.5}$, in Figure 5.6.Instead of the elimination of one hole per added substitution of La or Al, the trend suggests the removal of two per substitution. This suggests the possibility that there is some second carrier-producing defect tied to the total carriers in the system. Room temperature mobility values for the reduced carrier concentrations, as shown in Figure 5.9a, are higher than in the antimonide series or the reported Sn flux samples.

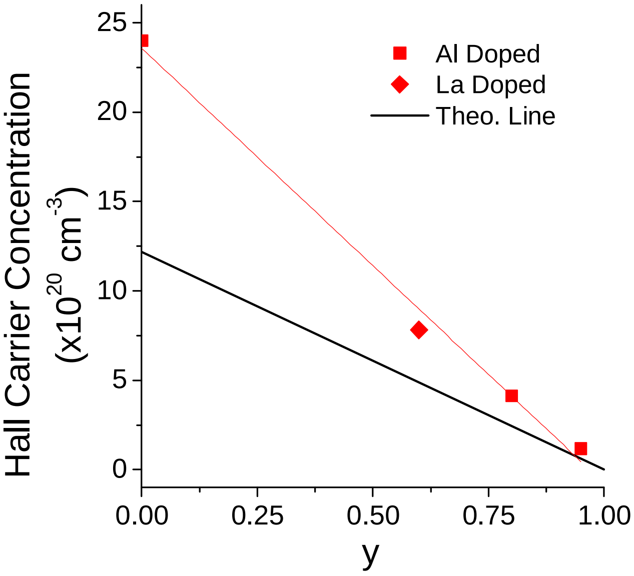

Figure 5.6. Plot of measured hall carrier concentration with Al or La content x for $Yb_{14}Mn_{1-x}Al_x$ $Bi_{5.5}$ $Sb_{5.5}$ and $Yb_{14-x}La_xMnBi_{5.5}$ $Sb_{5.5}$ ball milled samples.

High temperature resistivity plotted Figure 5.7a for $Yb_{14}Mn_{1-x}Al_xBi_{5.5}$ $Sb_{5.5}$ samples shows similar trends to those observed for $Yb_{14}Mn_{1-x}Al_xSb_{11}$, exhibiting a more semiconducting behavior as x increases. Increasing α and ρ with increasing Al content is also seen on the plot of Seebeck coefficient with temperature, as shown in Figure 5.7b, confirming the same shift to more semiconducting behavior seen in the antimonide. Estimated band gaps shown in Figure 5.7c and indicate a band gap of ~0.4 eV. A linear extrapolation from $Yb_{14}Mn_{1-x}Al_xSb_{11}$ yields a band gap for $Yb_{14}MnBi_{11}$ of ~0.2 eV.

Using the degenerate statistical method described in the previous section, the effective mass was calculated for the Al doped samples at 500K. Calculated values for effective mass as a function of η can be found in Figure 5.7d For x=0.8, resistivity below 650K is comparable to $Yb_{14}MnSb_{11}$ and yet the measured Seebeck coefficient is considerably lower due the much lower effective mass. Plotting the calculated m* values with η is shown in Figure 5.7d with a linear fit. From equation (5.2), a value of *a* is calculated to be 2 eV^{-1} and a m_0*of 0.2m_e. A summary of derived parameters for Al-doped $Yb_{14}Mn_{1-x}Al_x$ $Sb_{11}$and $Yb_{14}Mn_{1-x}Al_xBi_{5.5}$ $Sb_{5.5}$ alloy is found in Table 5.2.

Table 5.2. A comparison between parameters for $Yb_{14}Mn_{1-x}Al_x$ Sb_{11} and $Yb_{14}Mn_{1-x}Al_x$ Sb_{11} sample series for band gap (E_g) calculated from equation (5.3), fitted band edge effective mass (m_0*) and first order bending parameter (*a*) and for comparison the band gap inverse (E_g^{-1}).

Compositions	E_g (eV)	m_0* (m_e)	*a* (eV^{-1})	E_g^{-1} (eV^{-1})
$Yb_{14}Mn_{1-x}Al_x$ Sb_{11}	~0.6	1.2	2	1.7
$Yb_{14}Mn_{1-x}Al_xBi_{5.5}$ $Sb_{5.5}$	~0.4	0.2	2	2.5

Thermal conductivity is shown in Figure 5.8a for the $Yb_{14}Mn_{1-x}Al_xBi_{5.5}$ $Sb_{5.5}$ system. The trends are similar to those described for $Yb_{14}Mn_{1-x}Al_xSb_{11}$where the thermal conductivity drops with increasing aluminum content, and the appearance of the bipolar term appears at lower temperatures with increasing aluminum content. Figure 5.8b shows the estimated value for κ_{lat} as a function of temperature after the electron contribution has been subtracted from κ using the same values for heat capacity and assuming phonon-electron scattering in determining L. The calculated values of κ_{lat} show the same trend towards decreasing values above 300K and are lower at similar values of x than $Yb_{14}Mn_{1-x}Al_xSb_{11}$ as expected due to the increased point defect scattering from Bi. However, the values do not as closely approach the glassy limit, most likely because of the onset of the bipolar term at lower temperatures caused by the narrower band gap.

Overall there was unfortunately no substantial improvement in the thermoelectric performance over $Yb_{14}MnSb_{11}$. The temperature dependence of the power factor for $Yb_{14}Mn_{1-x}Al_xBi_{5.5}Sb_{5.5}$ and $Yb_{14}MnSb_{11}$ compositions is shown in Figure 5.8c. The power factors for the samples of $Yb_{14}Mn_{1-x}Al_xBi_{5.5}Sb_{5.5}$ do not substantially change with carrier concentration and are negatively impacted at high temperatures where thermally excited have a greater impact due to reduced band gap values. Thos impacts performance at high temperatures where the 14-1-11 materials get their largest ZT values. Finding 14-1-11 materials with larger band gaps are therefore preferable in order to take advantage of alloy scattering effects on κ_{lat}. Figure 3.7d shows ZT versus temperature for $Yb_{14}Mn_{1-x}Al_xBi_{5.5}Sb_{5.5}$ samples and $Yb_{14}MnSb_{11}$. However, due to the reduced thermal conductivity, these reduced carrier concentration alloys provide improvements over $Yb_{14}MnBi_{5.5}Sb_{5.5}$ with the sample of x=0.8 managing to improve ZT over the entire temperature range. These samples also match the ZT of $Yb_{14}MnSb_{11,}$ but for a reduced temperature range. Despite a calculated lower κ_{lat}, a reduced power factor for $Yb_{14}Mn_{1-x}Al_xBi_{5.5}Sb_{5.5}$ results in no substantial overall gain in ZT over $Yb_{14}MnSb_{11}$.

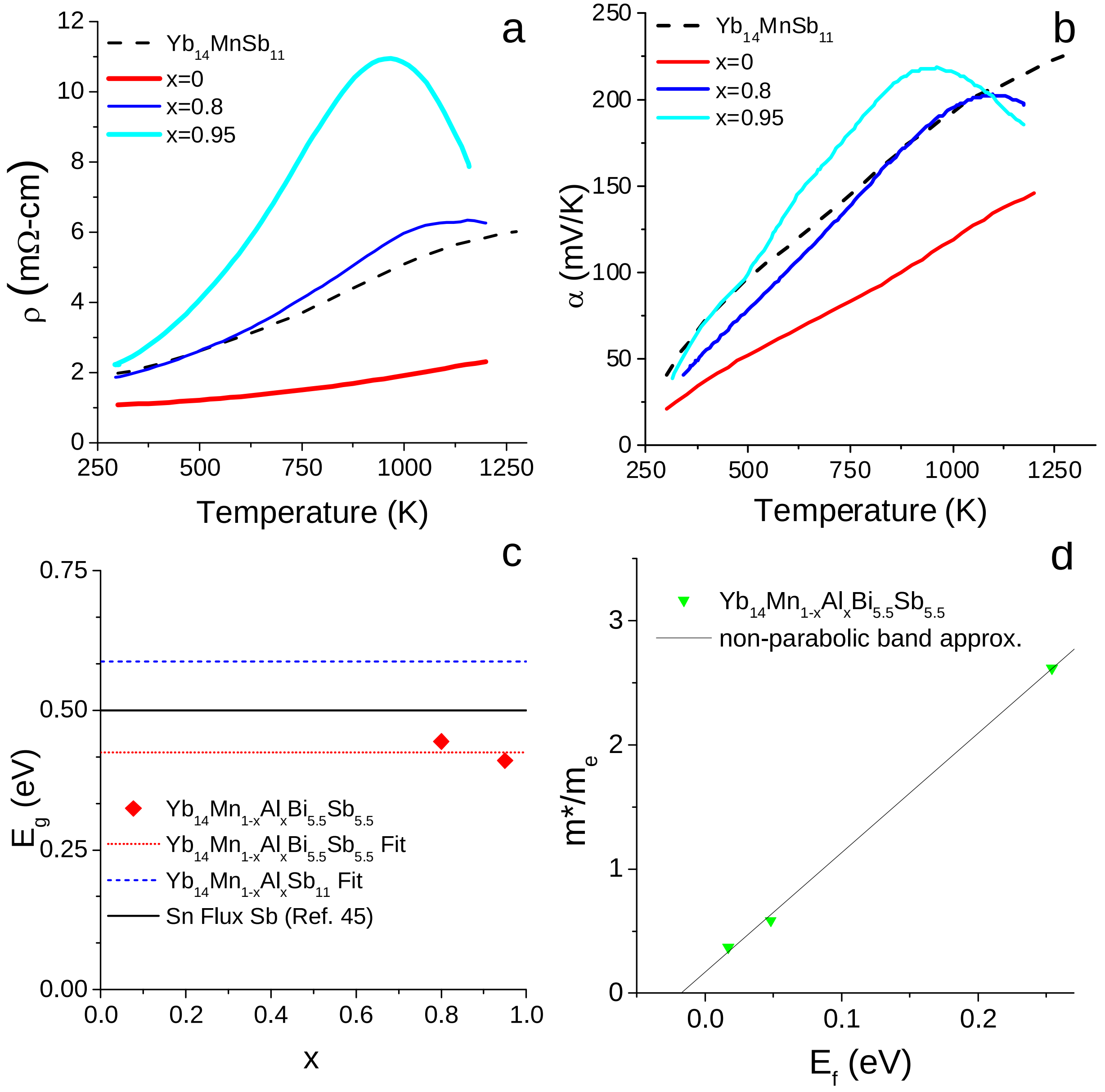

Figure 5.7. Temperature dependence for (a)Resistivity and (b) Seebeck coeficient for $Yb_{14}Mn_{1-x}Al_x$ $Bi_{5.5}$ $Sb_{5.5}$. c) Band gaps calculated from peak Seebeck coefficient values for $Yb_{14}Mn_{1-x}Al_x$ $Bi_{5.5}$ $Sb_{5.5}$ and the mean value from reference 45 and ball milled $Yb_{14}Mn_{1-x}Al_xSb_{11}$. d) Calculated effective mass for $Yb_{14}Mn_{1-x}Al_x$ $Bi_{5.5}$ $Sb_{5.5}$ samples versus calculated Fermi energy including the linear fit for calculating non-parabolic band bending parameters

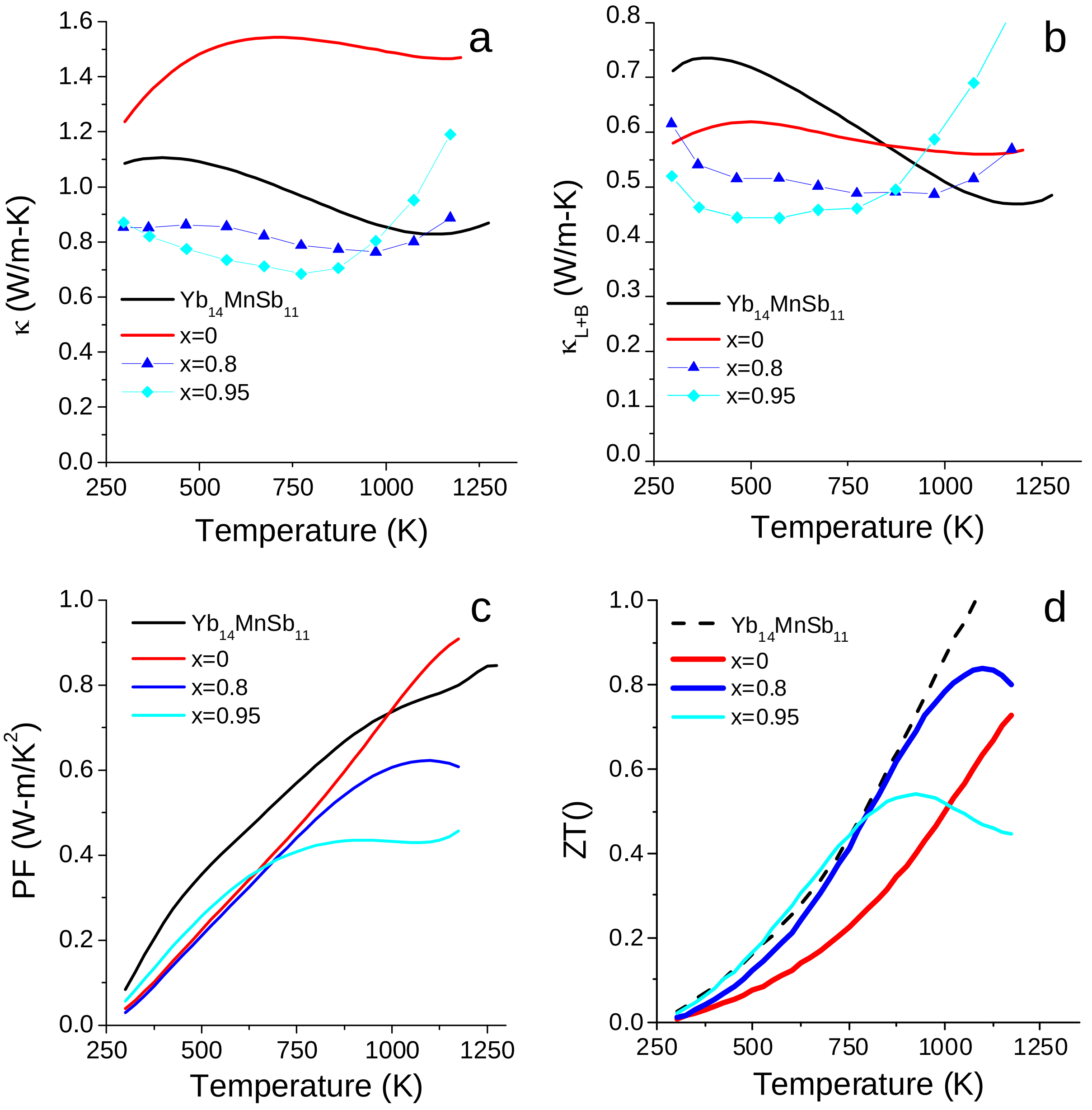

Figure 5.8. a) Total lattice thermal conductivity and thermal conductivity with electronic term versus temperature for $Yb_{14}Mn_{1-x}Al_x\ Bi_{5.5}\ Sb_{5.5}$ using molar heat capacity from reference 27. c) Power factor and (d) ZT versus temperature curves for ball milled $Yb_{14}Mn_{1-x}Al_x\ Bi_{5.5}\ Sb_{5.5}$.

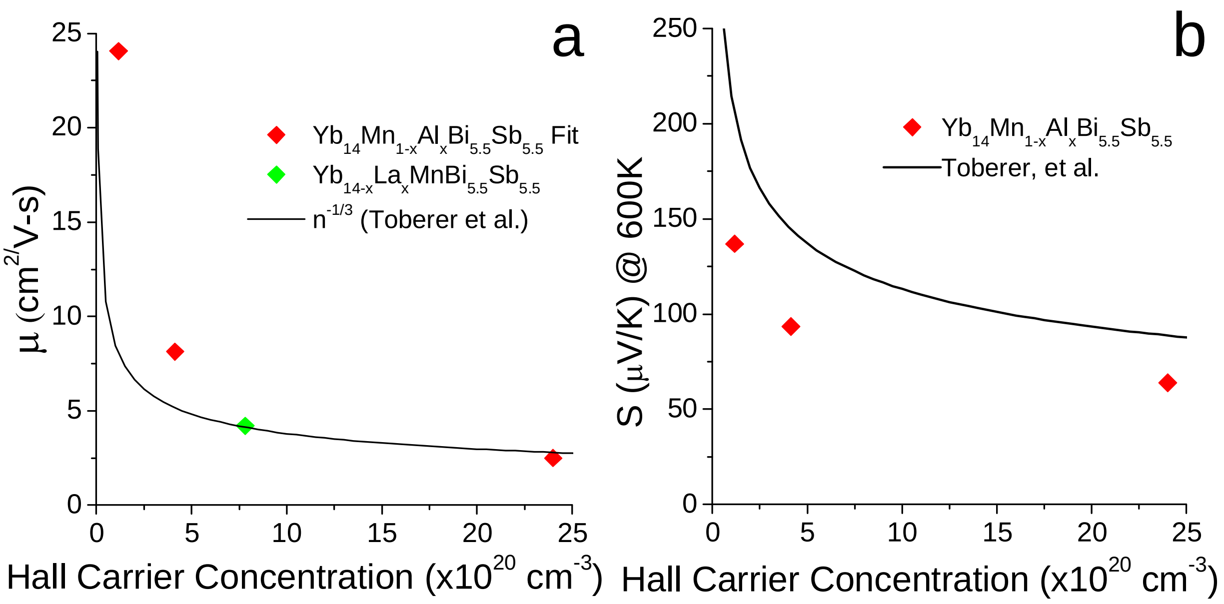

Figure 5.9. a) Mobility versus carrier curve for $Yb_{14}Mn_{1-x}Al_x$ $Bi_{5.5}$ $Sb_{5.5}$ and $Yb_{14-x}La_xMnBi_{5.5}$ $Sb_{5.5}$ at ~300K. b) A Pisarenko curve at 600K for $Yb_{14}Mn_{1-x}Al_xSb_{11}$ and $Yb_{14}Mn_{1-x}Al_xBi_{5.5}$ $Sb_{5.5}$ with a fit line from reference 45 for $Yb_{14}Mn_{1-x}Al_xSb_{11}$.

5.4. Conclusions

Reduced carrier concentration versions of $Yb_{14}Mn_1Sb_{11-y}Bi_y$ were synthesized, mostly by replacing Mn^{2+} with Al^{3+}. Using degenerate Fermi statistics, several material parameters were estimated. In $Yb_{14}Mn_{1-x}Al_xSb_{11}$, a calculated decrease in m* with increasing Al content was calculated and was consistent with effects due to non-parabolic band behavior. Because of this and the effects of thermally created carriers, and in spite of a marked decrease in lattice thermal conductivity, only limited improvement was obtained over the ZT of $Yb_{14}MnSb_{11}$. For $Yb_{14}Mn_{1-x}Al_xBi_{5.5}Sb_{5.5}$, the same non-parabolic behavior of m* was observed. Due to reduced power factor values, ZT did not improve over $Yb_{14}Mn_{1-x}Al_xSb_{11}$ in spite of lower κ_{lat}.

Because of effects of thermally created carrier pairs in these materials, materials in the 14-1-11 with wider band gaps should be explored. Additionally other doping methods should be investigated in an attempt to determine if different types of dopants can favorably influence band structure.

Chapter 6. The Effect of the Substitution of Yb on $Yb_{14}MnSb_{11}$.

6.1. Introduction

In Chapter 5, it was demonstrated that ball milling techniques could be used to synthesize 14-1-11 materials with variable carrier concentrations in the $Yb_{14}Mn_{1-x}Al_xBi_y Sb_{11-y}$ system. While some limited improvements in ZT were realized, reduction of the apparent effective mass at lower carrier concentrations limited overall improvement. In Chapter 4, substitutions of the Group V site replacing Sb with Bi and As, yielded no immediate improvement in ZT. Other options for modifying the structure could focus on either substituting on the Yb site or exploring other transition metals to substitute on the Mn site.

In the preceding chapter, it was suggested that $Yb_{14}Mn_{1-x}Al_xSb_{11}$ showed a reduction in the effective mass (m^*) which could be effectively modeled using a non-parabolic band behavior. Previously discussed calculations in Chapter 2 for $Ca_{14}AlSb_{11-x}As_x$ indicated that the bonds that had the greatest contribution to the valence band in the material were the group V atoms in the $[AlPn_4]^{-10}$ tetrahedra.[40] However, some drop in m^* at lower concentrations might also be due to the replacement of Jahn-Teller distorted $[MnSb_4]^{-11}$ tetrahedra with symmetrical $[AlSb_4]^{-10}$.[25, 27, 28, 45, 90] There is also the large difference in electronegativity between Al and Mn which might affect local bonding.[91] Therefore, modifying carrier concentration outside of altering the Group V tetrahedra would be useful in clarifying the correlation between carrier concentration and m^* independently of modifying the tetrahedra.

It was previously determined that Ca substitution in $Yb_{14}MnSb_{11}$ should be a very effective phonon scatterer using the Callaway-Von Bayer model. For $Yb_{14-x}Ca_xMnSb_{11}$, phonon scattering due to simple mass fluctuation leads to a dramatic reduction in $Yb_{14-x}Ca_xMnSb_{11}$ which approaches the glassy limit of thermal conductivity of $Yb_{14}MnSb_{11}$ around x=1 as shown in Figure 4.1. Previous work done on the system determined that the practical solubility limit of Ca in $Yb_{14}MnSb_{11}$ was about x=2.[92, 93] Above that, the samples exhibited signs of segregation of calcium and solid state synthesis of single phase coupons was difficult. Good solubility was expected because Ca^{2+} and Yb^{2+} have ionic radii which are within 2%.[91] In spite of the limited solubility range experimentally achieved, one should expect to see substantial reductions in the lattice thermal conductivity (κ_l).

Previous work in synthesizing this material has been done using Sn flux techniques as well as solid state reactions. Published thermoelectric results using $Yb_{14-x}Ca_xMnSb_{11}$ materials grown by the Sn flux technique have not shown improved peak ZT values over ball milled $Yb_{14}MnSb_{11}$ (ZT=1.2).[92] Materials synthesized using a direct solid state approach show some improvement over Sn flux-grown materials, but still do not achieve better ZT values. In both approaches, a $Yb_{11-x}Ca_xSb_{10}$ secondary phase negatively impacted carrier mobility, so that only peak ZT values of ~1 were obtained.[93]

In violation of a simple application of the Zintl-Klemm formulism, it has been shown that the addition of Ca leads to a significant reduction in carrier concentrations. A similar trend has been seen in $Yb_{1-x}Ca_xZn_2Sb_2$, another Zintl material.[76, 77] From $YbZn_2Sb_2$ to $CaZn_2Sb_2$, measured Hall hole concentrations decreased from ~3 x 10^{20} holes/cm^3 to ~1.5 x 10^{20} holes/cm^3.[76, 77] It was claimed that since Ca is more electropositive than Yb, Ca more fully transfers its valence electrons than Yb, leading to the compensation of holes.[77] More recently it has been suggested that the source of these defects is vacancies.[76]

There have been several attempts at modifying carrier concentration by modifying the alkali/rare earth site or the Group V site. $Yb_{14-x}La_xMnSb_{11}$ has been demonstrated to have comparable thermoelectric performance to $Yb_{14}Mn_{1-x}Al_xSb_{11}$ when synthesized via a Sn flux technique.[37] Attempts to modify the Group V site through doping have shown inconclusive results by substituting Sb with Ge or Te.[66, 67] $Ca_5Al_2Sb_6$ is a material understood through the Zintl-Klemm formulism to be a semiconductor and has shown carrier control with the substitution of Ca with Na. This substitution was found to be effective but it is limited by the solubility of Na. In $Yb_{14-x}La_xMnSb_{11}$, the substitution of Yb^{+2} with La^{+3} yields an electron which compensates for the hole from the $[MnSb_4]^{-11}$ cluster.[37, 83] In $Yb_{14-x}Na_xAlSb_{11}$, substitution of Yb^{+2} with Na^{+1} yields a hole that might conduct through the material since $Yb_{14}AlSb_{11}$ should be a charged balanced semiconducting compound.

Since there are differences in the performance of Sn flux-grown and ball-milled materials, a comparison of calculated properties is useful to identify these differences. The Sn flux growth conditions of $Yb_{14-x}Tm_xMnSb_{11}$ can be found in reference 94. Tm is expected to have similar properties to La in reducing carrier concentration. The material was calculated to have a modest improvement over Sn flux-grown $Yb_{14}MnSb_{11}$.[94] Data for $Yb_{14-x}Tm_xMnSb_{11}$ was analyzed using degenerate statistical methods to calculate values of effective mass and lattice thermal conductivity in order to compare with ball milled materials.

Models have been developed which have been used to predict the thermoelectric properties of heavily doped semiconductors.[10, 42, 95] Carrier mobility, Seebeck coefficient, power factor and ZT were modeled using parameters derived from $Yb_{14}Mn_{1-x}Al_xSb_{11}$. Better modeling will hopefully lead to a better understanding of 14-1-11 material systems and provide a better guide for future optimization.

6.2. Experimental

6.2.1. Synthesis

$Yb_{13.6}$ $La_{0.4}MnSb_{11}$, $Yb_{13.8}Na_{0.2}AlSb_{11}$ and $Yb_{12}Ca_2MnSb_{11}$using the process described in Chapter 3. The synthesis of Yb_{14-x} Tm_xMnSb_{11} via a Sn flux method is described in reference 94.

6.2.2. Characterization

The synthesized samples were characterized using the same methods and instruments as in previous chapters with the addition of albite ($NaAlSi_3O_8$) and anorthite ($CaAl_2Si_2O_8$) used for microprobe standardization. The typical microprobe analytical error was ~0.5% for Yb and Sb, ~5% for La and Ca, and ~10 % for Mn and Na. The characterization of Yb_{14-x} Tm_xMnSb_{11} is described in reference 94.

6.3. Results and Discussion

6.3.1. Yb_{14-x} Ca_xMnSb_{11}

The sample with a nominal composition of Yb_{12} Ca_2MnSb_{11} was measured by microprobe and the determined composition of $Yb_{12.04}Ca_{2.15}Mn_{1.01}Sb_{10.80}$ shows reasonably good agreement.. No secondary phases were apparent in back scattered electron SEM micrographs (Figure 6.1). In Figure 6.2d, the XRD pattern from the puck is shown with the ICDD reference pattern for $Yb_{14}MnSb_{11}$ and no secondary phases were detected. Lattice parameters were determined to be 16.621(5) Å (a) and 22.04(1) Å.

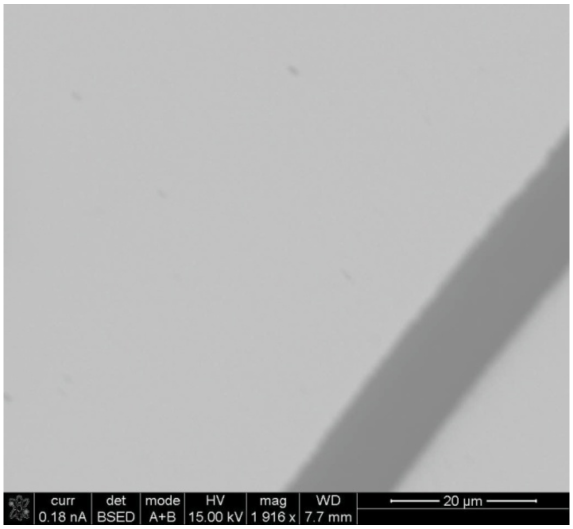

Figure 6.1. Backscattered SEM micrograph of the sample with a nominal composition of Yb_{12} Ca_2MnSb_{11}

Electronic transport properties at ~300K show slightly more resistive properties than ball milled $Yb_{14}MnSb_{11}$. Room temperature Seebeck coefficient was measured to be 48.6 µV/K and resistivity was measured to be 2.5 mΩ-cm. Room temperature Hall hole concentration was measured to be 8±1 x 10^{20} cm^{-3} which is within the error of the values in reference 92 for this composition. The Hall hole mobility was determined to be 3.0±0.4 cm^2/Vs.

Figure 6.2a shows a graph of Seebeck coefficient and resistivity for ball milled Yb_{12} Ca_2MnSb_{11} and the baseline reference $Yb_{14}MnSb_{11}$. Both the Seebeck coefficient and resistivity for the Ca-doped material were slightly higher than for $Yb_{14}MnSb_{11.}$ At higher temperatures there was no significant change in carrier concentration. At 500K, m^* was calculated using degenerate statistics using estimations of carrier scattering times due to ionized impurity and acoustic phonons as discussed earlier in Chapters 3 and 4. This calculation resulted in m^* of ~2.5m_e which is higher than the ~2m_e that was calculated for $Yb_{14}Mn_{0.6}Al_{0.4}Sb_{11}$. Carrier concentrations decreased slightly to 7±1 x 10^{20} at 500K. As illustrated by Figure 6.2c, the net result of the rise in resistivity and Seebeck coefficient results in little net change in the power factors between $Yb_{12}Ca_2MnSb_{11}$ and $Yb_{14}MnSb_{11}$.

Figure 6.2b shows thermal conductivity as a function of temperature for $Yb_{12}Ca_2MnSb_{11}$ and $Yb_{14}MnSb_{11}$. Values for thermal conductivity were close to each other and within the 10% experimental error. Values of thermal conductivity are comparable for direct synthesis materials and Sn flux-grown materials, however, ball milled $Yb_{12}Ca_2MnSb_{11}$ and $Yb_{14}MnSb_{11}$ showed less apparent bipolar effect.[92] The lattice thermal conductivity (κ_l) was estimated using the degenerate statistical method, assuming only acoustic phonon scattering. At ~300K, values for κ_l were 6.5 mW/cm-K for $Yb_{12}Ca_2MnSb_{11}$ compared to 7.5 mW/cm-K for $Yb_{14}MnSb_{11}$; this is not the substantial drop in thermal conductivity predicted from the Callaway and Von Bayer model.[47, 51, 52] This reduction is similar to the reduction of κ_l in un-doped $Yb_{14}MnSb_{11-1}Bi_y$ discussed in Chapter 4.

When ZT is plotted with temperature for both samples in Figure 6.2c, there is no substantial change in ZT. Despite increased m^* values at lower carrier concentrations, the degraded carrier mobility combined with a lack of reduction in lattice thermal conductivity lead to no net gain. This substitution does have some benefits in that it produces a boost in specific power of a device since the material is less dense and replaces expensive Yb.

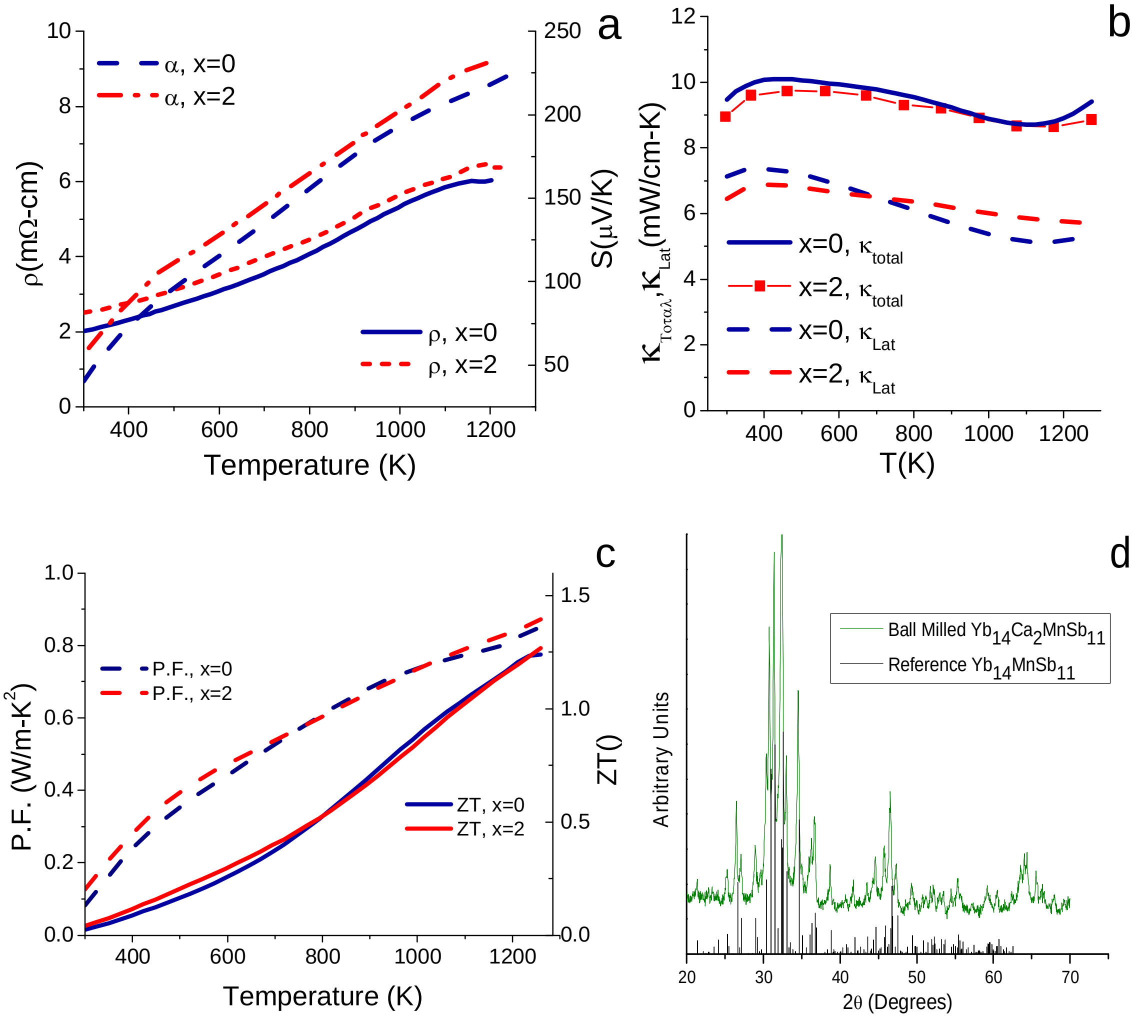

Figure 6.2. a) Resistivity and Seebeck coefficient, b) Total measure thermal conductivity and calculated κl and (c) power factor and ZT versus temperature for ball milled $Yb_{14}MnSb_{10}$ and Yb_{12} Ca_2MnSb_{11} ($Yb_{14-x}As_x$ Mn_1Sb_{11}). d) XRD pattern for the Yb_{12} Ca_2MnSb_{11} with reference pattern for $Yb_{14}MnSb_{11}$.

6.3.2. Yb_{14-x} La_xMnSb_{11} and Yb_{14-x} Na_xAlSb_{11}

Samples with the nominal compositions of $Yb_{13.6}$ $La_{0.4}MnSb_{11}$ and $Yb_{13.8}Na_{0.2}AlSb_{11}$ were characterized using electron microprobe and majority phase compositions were found to be $Yb_{13.63}La_{0.41}Mn_{1.08}Sb_{11.01}$ and $Yb_{12.04}Ca_{2.15}Mn_{1.01}Sb_{10.80}$ which is close to the expected values.

Backscattered electron micrographs (Figure 6.3b) showed secondary phases for $Yb_{13.6}La_{0.4}MnSb_{11}$ and $Yb_{13.8}Na_{0.2}MnSb_{11}$ which were less than 2 µm in diameter and comprised only about ~4% by volume of the material. Because sampling volume of beams used (acceleration voltages of 30 KeV) was estimated to be larger than particles, lower un-calibrated EDS measurements using lower acceleration voltages of 10 KeV gave the stoichiometry of the phase close to Yb_3LaSb_4. This is similar to $Yb_{14-x}Tm_xMnSb_{11}$ materials which found $Tm_{1-x}Yb_xSb$ to be a major second phase.[94] $Yb_{13.8}Na_{0.2}MnSb_{11}$ showed similar good agreement with expected values for the majority phase. Sub-micron secondary phases are apparent in backscattered electron micrographs as shown in Figure 6.3a and estimated to be only ~1% of the volume.

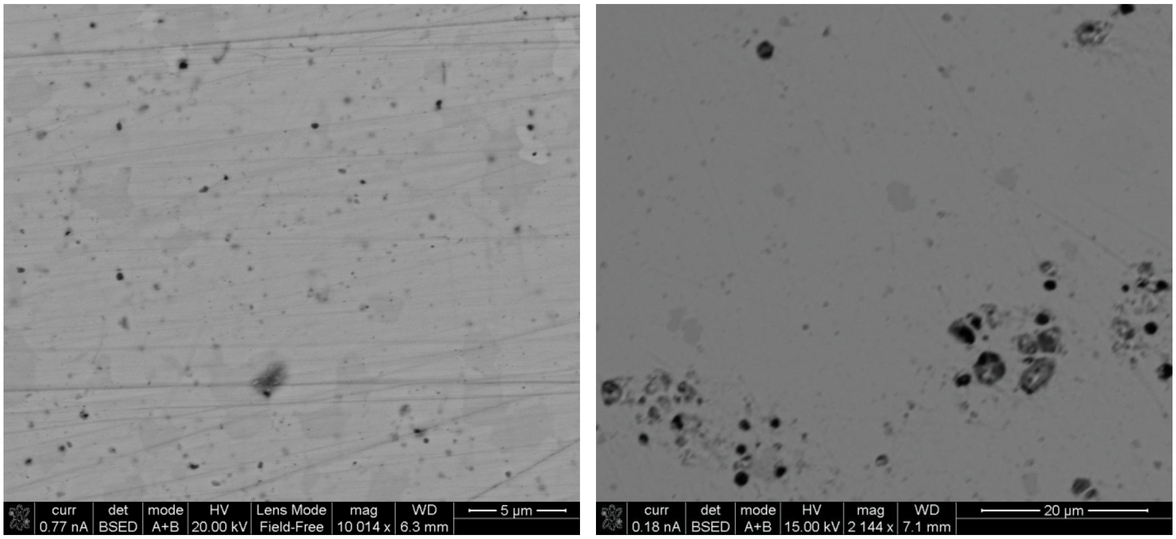

Figure 6.3. Back scattered electron micrographs of (left) $Yb_{13.8}Na_{0.2}MnSb_{11}$ and (right) $Yb_{13.6}La_{0.4}MnSb_{11}$. For $Yb_{13.6}La_{0.4}MnSb_{11}$, the dark spots are porosity. For $Yb_{13.8}Na_{0.2}MnSb_{11}$ darker grey areas were due to oxidation.

A summary of room temperature properties is shown in Table 6.1 comparing $Yb_{13.6}La_{0.4}MnSb_{11}$ and $Yb_{13.8}Na_{0.2}AlSb_{11}$ with ball milled $Yb_{14}Mn_{1-x}Al_{0.4}Sb_{11}$. Electrical resistivity values for La- and Na-doped samples around ~300K were 1.92 mΩ-cm and 2.7 mΩ-cm respectively. Hall hole concentration for the La doped material was 7.2±0.4x10^{20} cm^{-3} which is close to predicted the results seen in Sn flux grown material.[37] Na was a somewhat less effective dopant with a 1.4±0.2x10^{20} cm^{-3} hole concentration but this is not unexpected given the effects seen in $Ca_5Al_2Sb_6$.[96] The room temperature Seebeck coefficient was measured to be 42 μV/K which is lower than the 46 μV/K measured in $Yb_{14}MnSb_{11}$ and 52 μV/K for the $Yb_{14}Mn_{0.6}Al_{0.4}Sb_{11}$. This would suggest that the secondary phase is likely metallic. For the Na-doped sample, the room temperature Seebeck was 70 μV/K, which is close to the value for $Yb_{14}Mn_{0.2}Al_{0.8}Sb_{11}$.

Table 6.1. Summary of measured and calculated properties at 300K for Yb substituted doped materials. Added electrons per formula unit (e/F.U.) describe how many electrons are added to the system relative to $Yb_{14}MnSb_{11}$ as described by the Zintl-Klemm formulism. Errors in Hall carrier concentration (p^+ Hall) and mobility (μ) were derived from the standard deviation of measured hall resistance. Resistivity (ρ) was measured and measured errors estimated to be less than 3%. Measured Seebeck coefficient (α) is expected to have errors of 5%. Effective mass (m*) was estimated using the degenerate statistical approach and material properties at 500K.

Composition	e_-/F.U.	p^+ Hall (cm^{-3})	M ($cm^2V·s$)	ρ (mΩ·cm)	α (μV/K)	m* (m^*/m_e)
$Yb_{14}MnSb_{11}$	0	1.1±0.1x10^{21}	2.5±0.2	1.9	46	2.6
$Yb_{13.6}$ $Tm_{0.4}MnSb_{11}$ (TM2, Sn Flux Reference 94)	0-0.4*	1.1±1x 10^{21}	2.5±0.3	2.2	48	2.0
$Yb_{13.6}$ $La_{0.4}MnSb_{11}$	0.4	7.2±0.1 x10^{20}	4.6±0.1	1.9	42	1.9
$Yb_{14}Mn_{0.6}Al_{0.4}Sb_{11}$		7.5±0.3x10^{20}	3.5±0.1	2.2	52	2.0
$Yb_{14}Mn_{0.2}Al_{0.8}Sb_{11}$	0.8	2.2±0.1x10^{20}	8.7±0.3	3.1	72	1.5
$Yb_{13.8}Na_{0.2}AlSb_{11}$		1.4±0.2 x10^{20}	10.4±2	5.2	70	1.2

*It is uncertain whether Tm takes on a Tm^{+2} or Tm^{+3} state or some mixed valence.

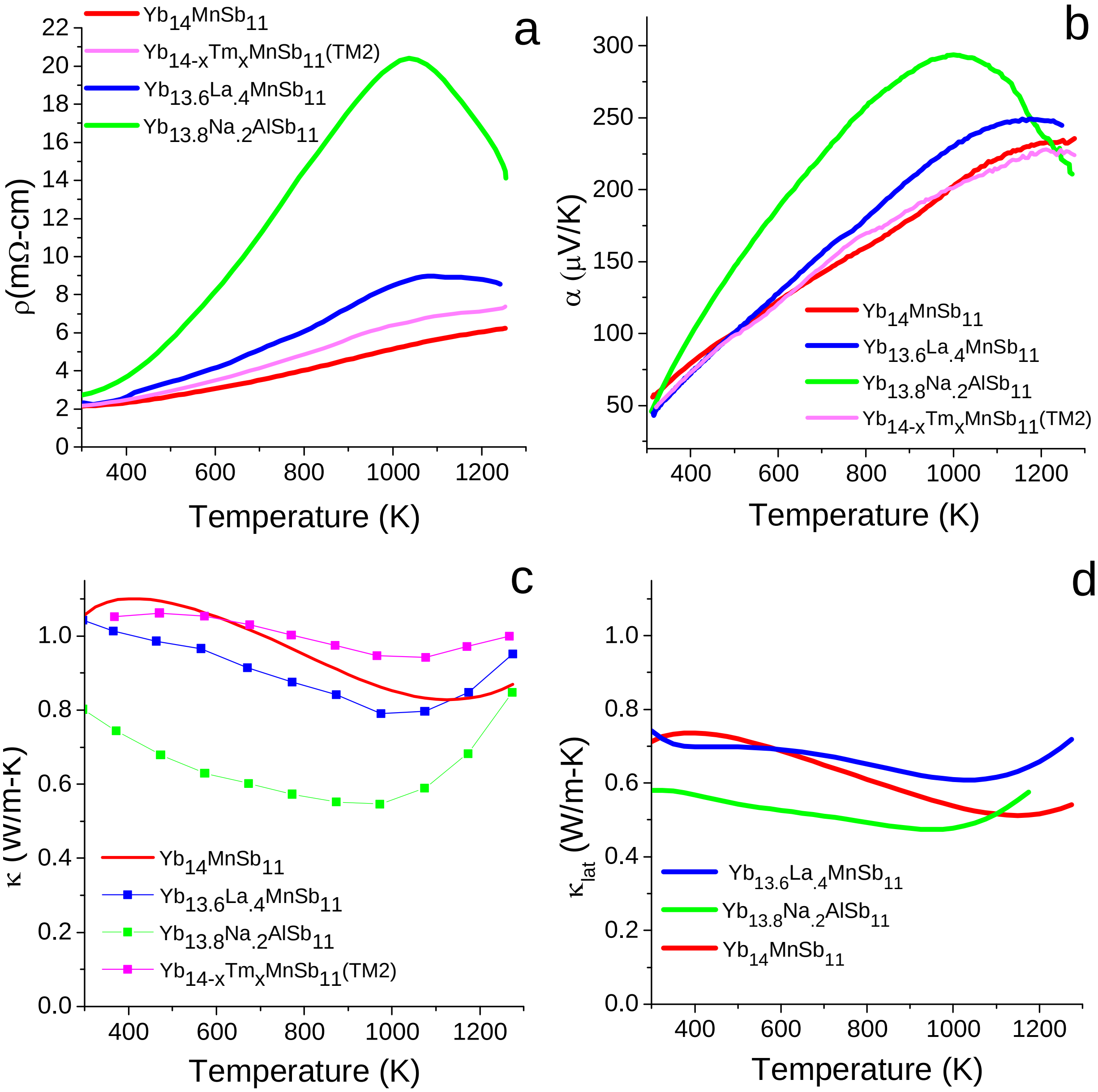

Figure 6.4. Plot of (a) resistivity, (b) Seebeck coeficient and (c) thermal conductivity with temperature for ball milled Yb$_{13.6}$ La$_{0.4}$MnSb$_{11}$, Yb$_{13.8}$Na$_{0.2}$MnSb$_{11}$, Yb$_{14}$MnSb$_{11}$, and Sn flux Yb$_{13.6}$Tm$_{x0.4}$MnSb$_{11}$ samples. d) Thermal conductivity with subtracted estimated electronic thermal conductivity with temperature for ball milled samples.

High temperature electrical resistivity and Seebeck coefficient curves are shown in Figure 6.4a-b. Both follow trends of semiconducting behavior with decreased carrier concentration. Also, the bipolar transport effect becomes apparent at higher temperatures for lower carrier concentration samples. The Hall hole concentration values measured at 500K, for La- and Na-doped materials were determined to be $5.0\pm1x10^{20}$ cm^{-3} and $1.0\pm0.2x10^{20}$ cm^{-3}, respectively. Using the estimated scattering time method described in Chapter 3, the m^* values were calculated to be ~1.9 m_e for $Yb_{13.6}La_{0.4}MnSb_{11}$ and ~1.2 m_e for $Yb_{13.8}Na_{0.2}MnSb_{11}$.

The variation in total thermal conductivity with temperature for doped and undoes materials is shown in Figure 6.4c. Total thermal conductivity decreases with the increase in resistivity as expected for the La- and Na-doped materials. For the estimated κ_l with temperature shown in Figure 6.4d, the La doped material showed good agreement with $Yb_{14}MnSb_{11}$ until at high temperature the bipolar effect starts becoming apparent, as expected. The room temperature value for κ_l was estimated to be 0.75 $W{\cdot}m^{-1}K^{-1}$. This value is consistent with what is expected in the Callaway-Von Bayer model, not including strain effects, since the masses of La and Yb are almost identical.[47, 51, 52] Volume fluctuation effects are also expected to be small as the difference atomic radii less than 1% as shown in Table 6.2. The Na doped material showed a decrease in estimated κ_l with a 300K value of 0.58 W/m-K. The Callaway-Von Bayer model predicts a substantial 25% decrease in κ_l just considering mass scattering and volume fluctuation scatter is expected to be nothing as the atomic radii of Na^{+1} and Yb^{+2} are identical.; however this decrease is also seen in $Yb_{14}Mn_{1-x}Al_xSb_{11}$ which does not follow as expected.[47, 51, 52]

A graph of power factor versus temperature is shown in Figure 6.5a for La-doped and Na-doped materials. The La-doped material showed an overall decrease in power factor which was consistent with what was seen for the comparable ball milled $Yb_{14}Mn_{0.6}Al_{0.4}Sb_{11}$ sample.

For the Na-doped material, a continued decrease in power factor at high temperatures was expected due to mixed conduction effects. The ZT versus temperature plot of La doped material is plotted with an Al-doped sample at a similar carrier concentration and undoped $Yb_{14}MnSb_{11}$ in Figure 6.5c. While this La-doped sample outperforms the Al-doped sample, neither outperforms the undoped ball milled material. A similar ZT plot for Na-doped and Al-doped equivalent ($Yb_{14}Mn_{0.6}Al_{0.4}Sb_{11}$) can be seen in Figure 6.5d. In spite of the reduced power factor, the calculated ZT does show some improvement for the Na-doped material in the same temperature range as the Al-doped sample over $Yb_{14}MnSb_{11}$. From the modeling put forth in Chapter 2, the improvement in ZT at lower temperatures qualitatively matches the behavior seen in Figure 2.7 where peak ZT shifts to lower temperature with lower effective masses. Improvement at higher temperatures is counteracted with the appearance of thermally created charge carrier pairs which are not taken into account in the simple model.

Table 6.2. Table summarizing the standard atomic mass (S.A.M.), possible ionic states and ionic radii of substitutions considered.

Element	S.A.M.[97]	Ion	Ionic Radius[91] (pm)
Yb	173.0	Yb^{+2}	116
		Yb^{+3}	108
Tm	168.9	Tm^{+2}	117
		Tm^{+3}	102
La	138.9	La^{+3}	117.2
Ca	40.1	Ca^{+2}	114
Na	23.0	Na^{+2}	116
Mn	54.9	Mn^{+2}	97
		Mn^{+3}	78.5
Al	27.0	Al^{+3}	67.5

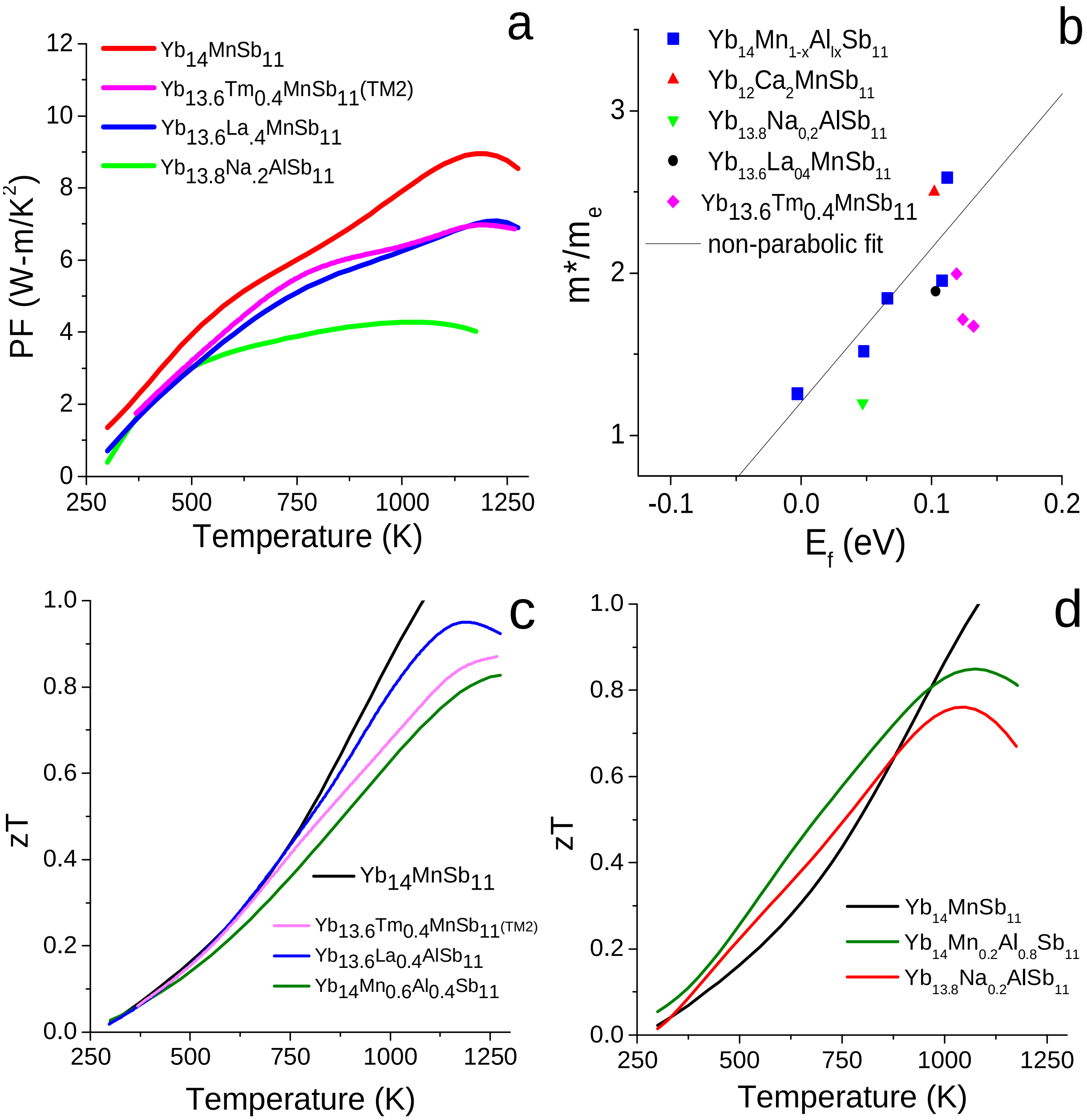

Figure 6.5. a) Plot of power factorwith temperature for ball milled $Yb_{13.6}$ $La_{0.4}MnSb_{11}$, $Yb_{13.8}Na_{0.2}MnSb_{11}$, $Yb_{14}MnSb_{11}$, and Sn flux $Yb_{13.6}Tm_{0.4}MnSb_{11}$ samples from Reference 94. b) Plot of calculated m^* with calculated Fermi level for various doped $Yb_{14}MnSb_{11}$ materials and the line fit given by equation (4.2). c) ZT plot with temperature of samples with 300K carrier $Yb_{13.6}$ $La_{0.4}MnSb_{11}$, $Yb_{14}Mn_{0.6}Al_{0.4}Sb_{11}$, $Yb_{14}MnSb_{11}$, and Sn flux $Yb_{13.4}$ $Tm_{0.4}MnSb_{11}$d) ZT plot of $Yb_{13.6}$ $La_{0.4}MnSb_{11}$, $Yb_{14}Mn_{0.6}Al_{0.4}Sb_{11}$ and $Yb_{14}MnSb_{11}$.

6.3.3. $Yb_{14-x}Tm_xMnSb_{11}$

$Yb_{14-x}Tm_xMnSb_{11}$ grown with a Sn flux method was characterized for high temperature electronic and thermal transport properties. The full results can be seen in reference 94. The samples were expected to have compositions of x= 0.3 (TM1), 0.5 (TM2) and 0.7 (TM3). However, it was found that the composition of the majority phase for all samples was close to x~0.4. Tm is expected to be isoelectronic in the structure with La, results should compare well with the previously discussed La-doped samples.[94] However, Tm can also form a +2 oxidation state which does not exist for La. TM2 was found to have a marginal improvement in ZT above the undoped Sn flux-grown $Yb_{14}MnSb_{11}$ and the best performing of the $Yb_{14-x}Tm_xMnSb_{11}$ samples.[94]

TM2 was found to be comparable in carrier concentration to the undoped ball milled $Yb_{14}MnSb_{11}$ with a Hall hole concentration of $1.1\pm1 \times 10^{21}$ cm^{-3} and mobility of 2.5 ± 0.3 cm^2/Vs. This carrier concentration measured value was slightly reduced but not significantly outside of the measurement error uncertainty of the reported Sn Flux value for $Yb_{14}MnSb_{11}$ of 1.3×10^{21} cm^{-3} and is much less than the~ 4×10^{20} cm^{-3} value expected from Tm^{3+} following Zintl-Klemm rules. This highly suggests that Tm is actually in a Tm^{2+} valence state. The hole mobility was also lower than the 3.2 cm^2/Vs observed in ball milled $Yb_{14}MnSb_{11}$.[94]

High temperature resistivity values of TM2 diverge from $Yb_{14}MnSb_{11}$ at higher temperatures as shown in Figure 6.4a, but do not reach the values of $Yb_{13.6}La_{0.4}MnSb_{11}$. Table 6.3 contains values measured and calculated properties at 500K for comparison. The values of α are comparable with $Yb_{14}MnSb_{11}$ (Figure 6.4b), as expected from the near identical carrier concentration to that of the baseline Sn-flux grown 14-1-11 sample. . As a result TM2 has a lower power factor than the two ball milled samples as shown in Figure 6.5a.

The value of the lattice thermal conductivity κ_l was estimated using the Wiedemann-Franz law and degenerate statistics, assuming acoustical phonon scattering, to calculate L. The results are plotted in Figure 6.6 with temperature. κ_l values around 300K for Tm-doped samples and Sn flux-grown $Yb_{14}MnSb_{11}$ were in good agreement those of ball-milled $Yb_{14}MnSb_{11}$, with values of 0.7±0.1 W/m-K which is within the expected range.[27, 94] At higher temperatures, the values diverge more from those of ball milled $Yb_{14}MnSb_{11}$, possibly due to increased thermal conductivity from the likely semiconducting second phase. As shown in Figure 6.5a, despite having a power factor close to the La doped sample, ZT above 750K for Tm-substituted samples is less than for the La-doped materials.

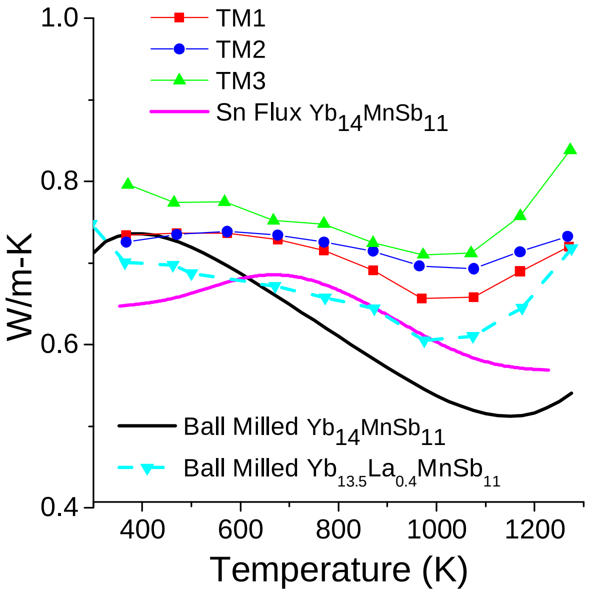

Figure 6.6**.** Temperature dependence of the thermal conductivity after subtraction of the estimated electronic conductivity. Yb_{14-x} Tm_xMnSb_{11} samples TM1, TM2 and TM3 (x ~ 0.4) from reference 94 are compared to ball milled $Yb_{14}MnSb_{11}$ and $Yb_{13.6}$ $La_{0.4}MnSb_{11}$.

6.3.4. Modeling of Thermoelectric Properties

Previous research showed that ZT for Sn flux-grown doped samples of $Yb_{14}MnSb_{11}$ peaked at a carrier concentration in the range of 2-6x10^{20} cm^{-3}.[37, 45] In ball-milled doped materials it was found that carrier concentration was not constant with temperature and there was no peak in ZT nor was there an improvement over undoped $Yb_{14}MnSb_{11}$. It is useful to attempt to use a single parabolic band model to explain these behaviors. Also, in Chapter 4, calculations for m^* indicated that $Yb_{14}Mn_{1-x}Al_xSb_{11}$ decreased with increasing aluminum content and this was consistent with a non-parabolic band seen in narrow band gap semiconductors.[87, 98] Here, modifying the carrier concentration by substitutions on the Yb site has shown conflicting results. The decrease in m^* calculated for La- and Tm-doped $Yb_{14}MnSb_{11}$ was consistent with non-parabolic bands. While Na-doped $Yb_{14}AlSb_{11}$ showed lower m^* than predicted by a non-parabolic fit, Ca-substituted $Yb_{14}MnSb_{11}$ did not show a drop in m^*. It is possible that metallic secondary phases in the Na doped materials are negatively impacting Seebeck coefficient values leading to reduced calculated m^* thus inducing such an apparently contradictory result.

Table 6.1. Summary of measured and calculated properties at 500K. Errors in Hall carrier concentration (p^+ Hall) and mobility (μ) were derived from the standard deviation of measured hall resistance. Reduced Fermi energy (η), effective mass (m*), lattice thermal conductivity (κ_{lat}) was estimated using degenerate statistics method outlined in the text. Resistivity (ρ) was measured and measured errors estimated to be less than 3%. Measures Seebeck coefficient (α) is expected to have errors of 5%. Measured thermal conductivity (κ) is expected to have errors of around 10%. Calculated Power Factor (P.F.) and ZT values are expected to have errors of 13% and 25% respectively.

Composition	p^+ Hall (cm^{-3})	μ ($cm^2V\cdot s$)	η	m* (m^*/m_e)	ρ ($m\Omega\cdot cm$)	α ($\mu V/K$)	κ ($W\cdot m^{-1}K^{-1}$)	κ_{lat} ($W\cdot m^{-1}K^{-1}$)	P.F. ($mW\cdot m^{-1}K^{-2}$)	ZT
$Yb_{14}MnSb_{11}$	$7.5\pm0.5x10^{20}$	3.0±0.2	0.112	2.6	2.6	96	1.09	0.72	3.5	0.18
Yb_{12} Ca_2MnSb_{11}	7 ± 2 $x10^{20}$	2.0±0.3	0.102	2.5	3.1	110	0.90	0.60	3.9	0.21
$Yb_{13.6}$ $Tm_{0.4}MnSb_{11}$ (TM2)	$6\pm1x$ 10^{21}	3.9±0.7	0.12	2.0	3.0	97	1.05	0.73	3.1	0.15
$Yb_{13.6}$ $La_{0.4}MnSb_{11}$	5.0 ± 1 $x10^{20}$	3.9±0.8	0.103	1.9	3.2	99	0.98	0.71	3.1	0.16
$Yb_{14}Mn_{0.6}Al_{0.4}Sb_{11}$	$4.8\pm0.5x10^{20}$	4.0±1	0.108	2.0	3.2	98	1.00	0.71	3.0	0.15
$Yb_{14}Mn_{0.3}Al_{0.7}Sb_{11}$	$2.5\pm0.3x10^{20}$	5.7±0.6	0.066	1.8	4.6	129	0.81	0.62	3.6	0.22
$Yb_{14}Mn_{0.2}Al_{0.8}Sb_{11}$	$1.5\pm0.1x10^{20}$	7.2±0.4	0.048	1.5	5.6	146	0.68	0.52	3.8	0.28
$Yb_{13.8}Na_{0.2}AlSb_{11}$	1 ± 0.2 $x10^{20}$	10.4±2	0.047	1.2	5.2	129	0.64	0.58	3.2	0.25
$Yb_{14}Mn_{0.05}Al_{0.9.5}Sb_{11}$	$4.8\pm0.5x10^{19}$	11.1±1	-0.003	1.3	11.5	208	0.53	0.45	3.8	0.35

The introduction (Chapter 2) described a formulism for calculating various materials properties using an energy dependent scattering mechanism for charge carriers. This takes into account the ratio of scattering by charged defects to that of acoustic phonons (b). Three cases are modeled in this chapter. The first is a single parabolic model with a fixed effective mass of $2.5m_e$, a value for $Yb_{14}MnSb_{11}$ estimated in Chapter 5, and only acoustic phonon scattering (b=0). This first case is commonly assumed for high temperature thermoelectric materials. This is a reference case as these are common assumptions when modeling thermoelectric materials and has been applied to $Yb_{14}Mn_{1-x}Al_{1x}Sb_{11}$ and other Zintl compounds.[35, 45, 96] The second case assumes a variable m^* with composition, in addition to assuming only acoustic scattering (b=0). The effective mass was calculated using equation (4.2) with a=2.8eV and $m_0^* = 1.2m_e$. In the third case, the b value was also calculated. The ratio between charged impurity scattering and acoustic phonon scattering using equation (2.10) and (2.11) was estimated using materials parameters ($\varepsilon_{DC} = 30\varepsilon_o$ and E_{def}=5eV) derived from the properties of $Yb_{14}MnSb_{11}$ around 500K and the measured Hall coefficient. Table 6.3 shows the values for both measured and derived properties of the samples under consideration. The calculated Seebeck values as a function of carrier concentration for all three cases are plotted in Figure 6.7a for all of the doped compositions considered so far (except for $Yb_{14}Mn_1Sb_{11-y}Bi_y$) at 500K. The Seebeck coefficient can be calculated using equation (2.17). The reduced Fermi level, η, was related to Hall carrier concentration using equations (2.9) and (2.21b). A temperature of 500K was chosen since results above 500K have an increasingly larger error in carrier mobility measurements. All methods reasonably describe the data trends with most data points falling between the first case (parabolic bands, acoustic carrier scattering only) and second case (non-parabolic bands and acoustic carrier scattering only). The Hall mobility was calculated using equation (2.21) for the three cases for m^* and b and is plotted versus Hall carrier concentration in Figure 6.7b. At lower concentrations, deviation from the third case model might be due to some other scattering mechanism such as neutral impurity scattering or grain boundary scattering.

The effect of carrier concentration on power factor was calculated using equation (2.17) and (2.20), and is shown in Figure 6.8a. In the first case of fixed m^* and b=0, the power factor increases with hole concentration and then falls off abruptly. In the other two cases, the reduction in m^* leads to an increase in power factor with decreasing carrier concentration. For $Yb_{14}Mn_{1-x}Al_xSb_{11}$, the power factor remains almost unchanged with carrier concentration. This is due to reduced hole mobility increasing the electrical resistivity. $Yb_{12}Ca_2MnSb_{11}$ trends higher because of its higher calculated effective mass. The other samples with Yb-substituted doping trended lower, since they all exhibited secondary phases, it is uncertain if these are the source of lower mobility or Seebeck coefficient or if there is an effect due to the properties of the material itself.

For the model ZT curves, κ was estimated using the Wiedemann-Franz law and the 500K calculated κ_l (0.71 $Wm^{-1}K^{-1}$) for ball milled $Yb_{14}MnSb_{11}$ with L calculated from equation (2.24). This value was then used to calculate ZT as a function of Hall carrier concentration and the results are plotted on Figure 6.8b. There was no substantial difference between the second and third cases, while for the first case there is a sharp increase in ZT followed by a sharp decline. In spite of showing the correct trend for $Yb_{14}Mn_{1-x}Al_xSb_{11}$, this result is largely due to a drop in κ_l. La- and Na-doped samples as well as the Sn flux-grown Tm-doped samples, exhibited a lower ZT. It is uncertain to whether this specifically has to do with doping effects on the Yb site, or if this is rather due to the presence of detectable second phases.

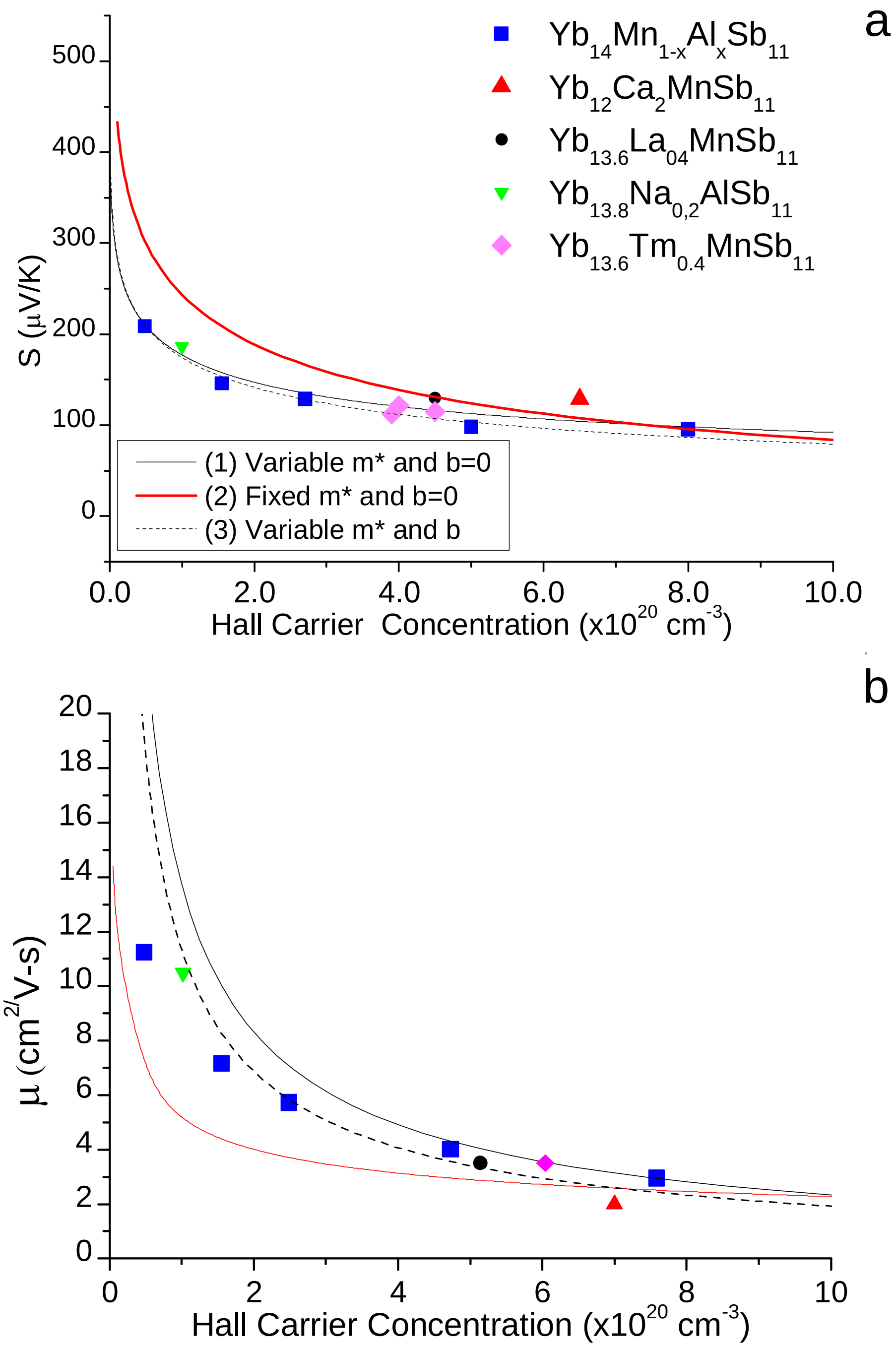

Figure 6.7. a) Calculated Seebeck coefficient and b) Hall mobility at 500K for ball milled Yb$_{14}$MnSb$_{11}$ with various dopants and Sn flux-grown Yb$_{13.6}$Tm$_{0.4}$MnSb$_{11}$ from reference 94.

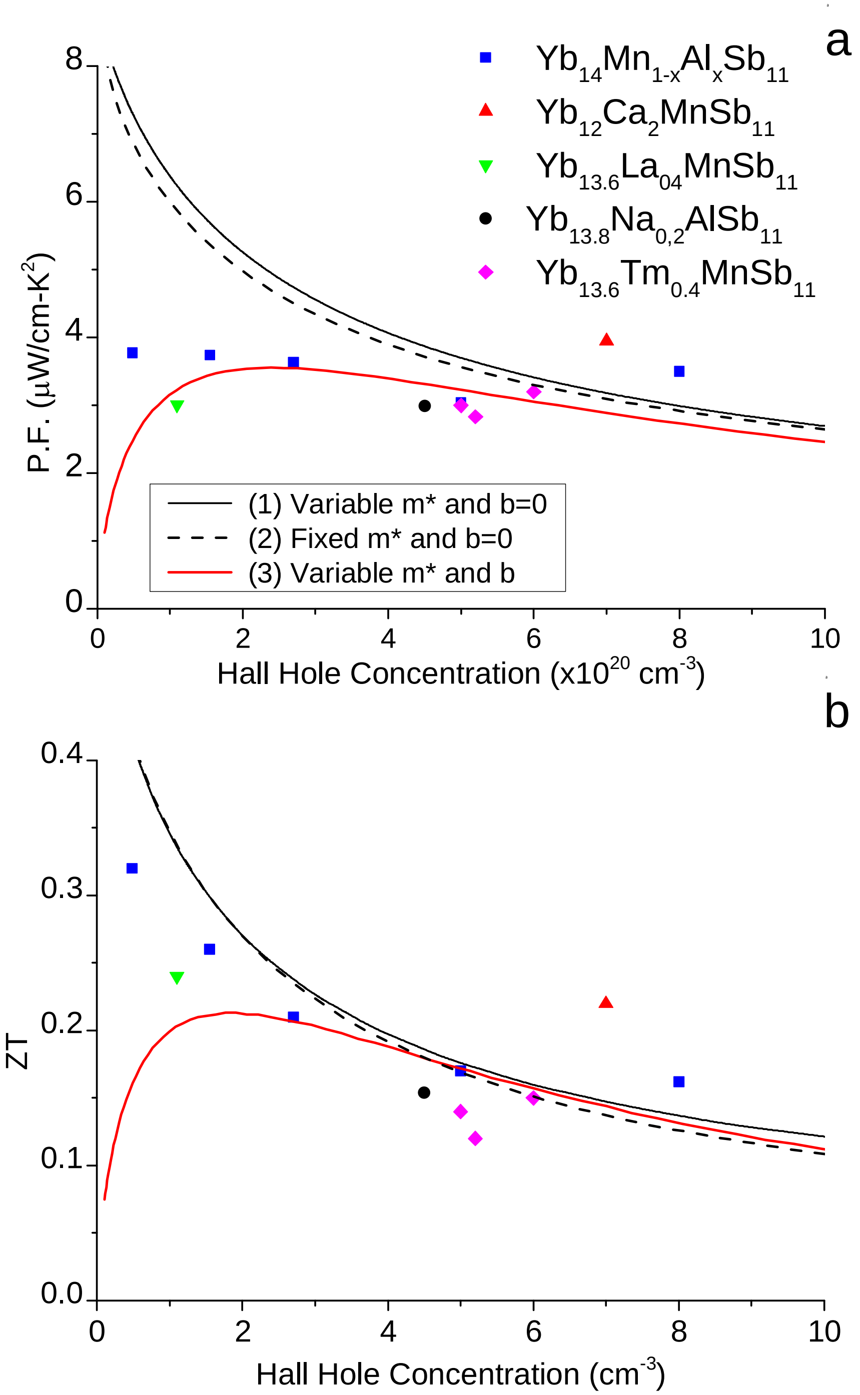

Figure 6.8. a) Calculated power factor (P.F) and (b) ZT at 500K for ball milled $Yb_{14}MnSb_{11}$ with various dopants and Sn flux-grown $Yb_{13.6}Tm_{0.4}MnSb_{11}$ from reference 94.

6.4. Conclusion

$Yb_{13.6}$ $La_{0.4}MnSb_{11}$, $Yb_{13.8}Na_{0.2}AlSb_{11}$ and $Yb_{12}Ca_2MnSb_{11}$ were synthesized using a high energy ball milling technique and their high temperature thermal and electronic transport properties were characterized. $Yb_{13.6}$ $La_{0.4}MnSb_{11}$ and $Yb_{13.8}Na_{0.2}AlSb_{11}$ were found to have ZT values similar to that of samples of the $Yb_{14}Mn_{1-x}Al_xSb_{11}$ series with similar carrier concentrations, with no improvement over the peak ZT of 1.2 achieved for the baseline ball milled $Yb_{14}MnSb_{11}$. In the Ca-substituted material, contrary to expectations, there was little calculated effect of point defect scattering in the estimated κ_l and power factor values were found to be nearly unchanged from $Yb_{14}MnSb_{11}$. As a result, ball milled $Yb_{12}Ca_2MnSb_{11}$ was found to have ZT values matching closely those of $Yb_{14}MnSb_{11}$.

Sn flux-grown $Yb_{13.6}Tm_{0.4}MnSb_{11}$ was analyzed using degenerate statistics to compare estimated values of κ_l and m^* to ball milled equivalently doped $Yb_{14}MnSb_{11}$. It was found at the room temperature lattice thermal conductivity was close to that of undoped $Yb_{14}MnSb_{11}$ but diverged upward at higher temperatures due to the presence of second phases. There was also no significant change in effective mass value compared to the other doped samples. No matter which substitutional doping method was employed for $Yb_{14}MnSb_{11}$, it did not greatly affect the overall performance of the material. Even a substantial substitution of Yb with Ca led to virtually no change in ZT values.

Chapter 7. Conclusions and Future Work

Previous research on 14-1-11 compounds focused primarily on flux based synthesis methods. In this dissertation, we found that we found that high energy ball milling from elemental sources was capable of synthesizing a wide range of $Yb_{14}MnSb_{11}$ derivatives with substitutions for each element. These materials were found suitable for characterization of thermal and electrical properties.

The Callaway and von Baeyer model predicted substantial reductions in lattice thermal conductivity for the substitutions synthesized. The studied substitutions where shown to have a varying degrees of success in lowering lattice thermal conductivity as a rout to higher ZT. A significant decrease in κ_l, by as much as 33% of the pure antimonide value, was observed but not to the extent predicted by the Callaway and von Baeyer model, when only scattering effects due to point defect mass fluctuations were considered. For $Yb_{14}MnSb_{10}As_1$, calculated κ_l reduction was close to expected values, but within the expected error of the thermal conductivity measurement. In the Ca-substituted material, contrary to expectations, there was little calculated effect of point defect scattering in the estimated κ_l and power factor values were found to be nearly unchanged from $Yb_{14}MnSb_{11}$. Unexpectedly, $Yb_{14}Mn_{1-x}Al_xSb_{11}$ showed a decrease in κ_{lat} with increasing x. $Yb_{14}Mn_{1-x}Al_x\ Bi_{5.5}\ Sb_{5.5}$ show similarly enhanced improvement in κ_{lat} with increasing x.

The $Yb_{14}Mn_1Sb_{11-y}Bi_y$ system, $Yb_{14}Mn_1Sb_{10}As_1$ and $Yb_{12}Ca_2MnSb_1$ were expected to be isoelectrical with $Yb_{14}MnSb_{11}$ and later could be doped to yield materials with possibly superior ZT. The $Yb_{14}Mn_1Sb_{11-y}Bi_y$ system was found to have increasing metallic content with increasing Bi content. Up to y=5 for $Yb_{14}Mn_1Sb_{11-y}Bi_y$, the calculated values for carrier mobility (μ) and effective mass (m*) were remained similar. In a departure from what the Zintl-Klemm rules, carrier concentrations were observed to increase with increasing Bi content. Reduced power factor and increased electronic contribution to the thermal conductivity lead to a reduction in ZT in spite of lower κ_{lat} for the Bi containing alloys. Similarly to its thermal properties, $Yb_{14}Mn_1Sb_{10}As_1$ showed electrical properties which were in the expected error of the measurement and ZT was not significantly changed. $Yb_{12}Ca_2MnSb_{11}$ was found to have a calculated increase in m* and decrease carrier concentration versus $Yb_{14}MnSb$. However, overall power factor and ZT remained unchanged.

In parallel with isoelectric substitutions, several different methods of doping to improve ZT were attempted. Samples in the $Yb_{14}Mn_{1-x}Al_xSb_{11}$ system were found with decreased charier concentration and increase semiconducting properties with increasing Al content which was consistent with previous work. However, calculated ZT curves showed different behavior between ball milled material presented here and other's materials synthesized through a Sn-flux method. Unlike the previously published Sn-flux material, peak ZT decreased with the addition Al. For the best published composition, $Yb_{14}Mn_{0.2}Al_{0.8}Sb_{11}$, peak ZT was lower in the ball milled sample at similar composition, but below the peak ZT of ball milled $Yb_{14}MnSb_{11}$. Since calculated ZT for $Yb_{14}MnSb_{11}$ is given as significantly higher (1.4 versus 0.9), material quality differences should be explore as discrepancies. The ZT curves of both methods of synthesis $Yb_{14}Mn_{0.2}Al_{0.8}Sb_{11}$ do yield some improvement over ball milled $Yb_{14}MnSb_{11}$ below 1000K. In $Yb_{14}Mn_{1-x}Al_x Bi_{5.5} Sb_{5.5}$, the addition of Al lead to reduced carrier concentration, but ZT never exceeded that of $Yb_{14}MnSb_{11}$. $Yb_{13.6} La_{0.4}MnSb_{11}$ and $Yb_{13.8}Na_{0.2}AlSb_{11}$ showed similar values of ZT when compared with samples in the $Yb_{14}Mn_{1-x}Al_xSb_{11}$ at approximately equivalent carrier concentrations.

Transport property modeling at 500K using a degenerate statistical approach was found to give a good description of the thermoelectric properties of doped $Yb_{14}MnSb_{11}$ when the effective mass was dependent on the Fermi potential (non-parabolic behavior). Trends in calculated effective mass on doped $Yb_{14}AlSb_{11}$ and $Yb_{14}MnSb_{11}$ were inconclusive in helping to determine if the decrease in m^* with carrier concentration or reduced Fermi potential was due to band bending or changes in the band structure with composition.

Though none of the compositions studied here lead to a clear increase in average ZT, there are some indicators of where future work research might be directed. The possibility of the reduction of lattice thermal conductivity by point defect scattering or some other mechanism to increase ZT at low temperatures might still be obtainable. Samples in the $Yb_{14}Mn_{1-x}Al_xSb_{11-y}Bi_y$ system were calculated to have a significant reduction in lattice thermal conductivity though changes in electrical properties caused ZT to decrease. $Yb_{14}Mn_1Sb_{10}As_1$ and $Yb_{12}Ca_2MnSb_{11}$ were shown to have minimal effect on electrical properties though there was little calculated reduction in lattice thermal conductivity. There still might be some substitution which might cause an increase scattering of phonons with little change to the electrical properties. This should lead to moderate increase in ZT at lower temperatures. Further improvements in material quality might allow for higher mobility materials which might minimize electron scattering due to boundaries and other defects not considered here.

For high temperature performance, a drastic change in chemistry coupled with a better understanding of how to tune the band structure will be needed to better exploit the 14-1-11 structure as a thermoelectric material. Materials with a band gap wider than that of $Yb_{14}MnSb_{11}$ remain an attractive target of search as the effectiveness of conventional doping is held back at high temperatures by intrinsic carrier formation. Materials which have novel band structures suggested by first principles calculations due to the preferential filling of sites pnicogen in the tetrahedra of the structure might still exist.[40] The space covered in the thesis is just a small area of the potential compounds which might have these properties.

As a last potential area of potential future work, composites might be explored as a way to improve high temperature performance. As discussed in Chapter 5, Sn-flux grown samples[47] appeared to suffer less degradation in power factor due to thermally created carriers than the more phase pure ball milled samples. Further work understanding the mechanism of this enhanced performance might lead to controlled composites which might lead to increased high temperature performance.

REFERENCES

[1] J.-P. Fleurial, *Journal of the Mineral* **2009,** *61*, 79.

[2] D.M. Rowe (Ed.), *Thermoelectrics Handbook: Macro to Nano-structured Materials*, Taylor & Francis, **2005**.

[3] *Atomic Power in Space—A History*, U.S. Department of Energy, Washington, D.C., **1987**.

[4] C. B. Vining, G. L. Bennett, *46th AIAA Joint Propulsion Conference & Exhibit,* **2010,** 6598.

[5] C. Wood, *Reports on the Progress of Physics* **1988,** *51*, 459.

[6] C. Wood, J. W. Vandersande, and C. B. Vining, *proceedings of the Eighth International Conference on Thermoelectric Energy Conversion*, **1989**, 83.

[7] A. McEvoy, T. Markvart and L. Castaner, Eds., *Practical Handbook of Photovoltaics, 2nd* Ed., Academic Press, **2012**.

[8] G. J. Snyder, T. S. Ursell, *Physical Review Letters* **2003,** *91*, 148301.

[9] T. C. Jean-Pierre Fleurial, Bill J. Nesmith, Richard C. Ewell, David F. Woerner, Gregory C. Carr and Loren E. Jones, *Thermoelectrics: From Space Power Systems to Terrestrial Waste Heat Recovery Applications*, 2011 Thermoelectrics Application Workshop, DOE, San Diego, CA, **2011**.

[10] J. P. Fleurial, L. Gailliard, R. Triboulet, H. Scherrer, S. Scherrer, *Journal of Physics and Chemistry of Solids* **1988,** *49*, 1249.

[11] J. Chan, Wood, J.G., and Schreiber, J.G., *proceedings of Space Technology and Applications International Forum,* **2007,** 8.

[12] G. J. Snyder, *Interface* **Fall 2008,** 3.

[13] L. I. S. Shure, J. Harvey,in *Survey of Electrical Power Plants for Space Applications*, **1965**, 33.

[14] A. Shakouri, *proceedings of the Twentieth Annual IEEE Semiconductor Thermal Measurement and Management Symposium,* **2004**, 1.

[15] T. S. Mann, Stan; Grenoble, Ray; Mason, Brian; Rosario, Sev; Fairbairn, *proceedings of the 53rd AIAA/ASME/ASCE/AHS/ASC Structures, Structural Dynamics and Materials Conference*, **2012**, 11.

[16] S. H. Yang, T. J. Zhu, T. Sun, J. He, S. N. Zhang, X. B. Zhao, *Nanotechnology,* **2008,** *19*,

245707.

[17] Y. Pei, A. F. May, G. J. Snyder, *Advanced Energy Materials* **2011** *1*, 291.

[18] T. Caillat, J. P. Fleurial, G. J. Snyder, *Solid State Sciences* **1999,** *1*, 535.

[19] G. S. Nolas, J. L. Cohn, G. A. Slack, S. B. Schujman, *Applied Physics Letters* **1998,** *73*, 178.

[20] B. C. Sales, D. Mandrus, R. K. Williams, *Science* **1996,** *272*, 1325.

[21] G. J. Poon, M. T. Terry, in *Semiconductors and Semimetals*, Elsevier, **2001**, *70*, 37.

[22] E. S. Toberer, A. Zevalkink, G. J. Snyder, *Journal of Materials Chemistry* **2011**, *21*, 15843.

[23] G. J. Snyder, E. S. Toberer, *Nature Materials* **2008,** *7*, 105.

[24] D. T. Morelli, *MRS Proceedings* **1997,** *478*, 279.

[25] S. R. Brown, S. M. Kauzlarich, F. Gascoin, G. J. Snyder, *Chemistry of Materials* **2006,** *18*, 1873.

[26] S. K. Bux, R. G. Blair, P. K. Gogna, H. Lee, G. Chen, M. S. Dresselhaus, R. B. Kaner, J.-P. Fleurial, *Advanced Functional Materials* **2009,** *19*, 2445.

[27] C. A. Cox, E. S. Toberer, A. A. Levchenko, S. R. Brown, G. J. Snyder, A. Navrotsky, S. M. Kauzlarich, *Chemistry of Materials* **2009,** *21*, 1354.

[28] J. Y. Chan, M. M. Olmstead, S. M. Kauzlarich, D. J. Webb, *Chemistry of Materials* **1998,** *10*, 3583.

[29] A. Rehr, T. Y. Kuromoto, S. M. Kauzlarich, J. Del Castillo, D. J. Webb, *Chemistry of Materials* **1994,** *6*, 93.

[30] J. Y. Chan, M. E. Wang, A. Rehr, S. M. Kauzlarich, D. J. Webb, *Chemistry of Materials* **1997,** *9*, 2131.

[31] D. M. Young, C. C. Torardi, M. M. Olmstead, S. M. Kauzlarich, *Chemistry of Materials* **2002,** *7*, 93.

[32] S. M. Kauzlarich, M. M. Thomas, D. A. Odink, M. M. Olmstead, *Journal of the American Chemical Society* **1991,** *113*, 7205.

[33] J. T. Vaughey, J. D. Corbett, *Chemistry of Materials* **1996,** *8*, 671.

[34] S. C. Sevov, in *Intermetallic Compounds - Principles and Practice*, John Wiley & Sons, **2002**, 113.

[35] E. S. Toberer, A. Zevalkink, N. Crisosto, G. J. Snyder, *Advanced Functional Materials* **2010**, *20*, 4375.

[36] D. Sanchez-Portal, R. M. Martin, S. M. Kauzlarich, W. E. Pickett, *Physical Review B* **2002,** *65*, 144414.

[37] E. S. Toberer, S. R. Brown, T. Ikeda, M. K. Susan, G. J. Snyder, *Applied Physics Letters* **2008,** *93*, 062110.

[38] S. R. Brown, E. S. Toberer, T. Ikeda, C. A. Cox, F. Gascoin, S. M. Kauzlarich, G. J. Snyder, *Chemistry of Materials* **2008,** *20*, 3412.

[39] C. Cox, S. Brown, G. Snyder, S. Kauzlarich, *Journal of Electronic Materials* **2010**, *39*, 1373.

[40] T. Vo, P. von Allmen, J. P. Fleurial, *APS Meeting*, **March 2011**, *1*, 28004.

[41] H. K. Jianxiao Xu, *Journal of Computational Chemistry* **2008,** *29*, 2134.

[42] V. L. Fistul, *Heavily Doped Semiconductors*, Plenum Press, **1967**.

[43] N. F. Mott, H. Jones, *The theory of the properties of metals and alloys*, Dover Publications, **1958**.

[44] M. Cutler, J. F. Leavy, R. L. Fitzpatrick, *Physical Review*, **1964,** *133*, A1143.

[45] E. S. Toberer, C. A. Cox, S. R. Brown, T. Ikeda, A. F. May, S. M. Kauzlarich, G. J. Snyder, *Advanced Functional Materials* **2008,** *18*, 2795.

[46] T. Caillat, private communication.

[47] J. Callaway, *Physical Review* **1959,** *113*, 1046.

[48] M. G. Holland, *Physical Review* **1963,** *132*, 2461.

[49] D. G. Cahill, S. K. Watson, R. O. Pohl, *Physical Review B* **1992,** *46*, 6131.

[50] P. G. Klemens, *proceedings of the Physical Society. Section A* **1955,** *8*, 1113.

[51] A. Borshchevsky, T. Caillat, J. P. Fleurial, *proceedings of Fifteenth International Conference on Thermoelectrics*, **1996**, 112.

[52] J. Callaway, H. C. von Baeyer, *Physical Review* **1960,** *120*, 1149.

[53] R. W. Ure, *Energy Conversion* **1972,** *12*, 45.

[54] K. Z. Star, Alex Huang, Chen-Kuo Dunn, Bruce Fleurial, Jean-Pierre, *MRS Proceedings*, **2010**, *1267*, 1267-DD03-05

[55] V. A. L. Ravi, B. Chun-Yip, J.-P. Fleurial, K. Star, *Nasa Tech Briefs* **2010.**

[56] A. F. May, J.-P. Fleurial, G. J. Snyder, *Physical Review B* **2008,** *78*, 125205.

[57] C.-K. Huang, G. J. Snyder, R. Blair, A. May, J.-P. Fleurial, *Nasa Tech Briefs* **2007**.

[58] C. Suryanarayana, *Progress in Materials Science* **2001,** *46*, 1.

[59] G. Schaffer, P. McCormick, *Metallurgical and Materials Transactions A* **1990,** *21,* 2789.

[60] J. Michiels, K. A. Gschneidner, *Journal of Applied Physics* **1997,** *82,* 4952.

[61] J. Schilz, M. Riffel, K. Pixius, H. J. Meyer, *Powder Technology* **1999,** *105*, 149.

[62] L. Zhang, A. Grytsiv, M. Kerber, P. Rogl, E. Bauer, M. J. Zehetbauer, J. Wosik, G. E. Nauer, *Journal of Alloys and Compounds* **2009,** *481*, 106.

[63] M. Abdellaoui, E. Gaffet, *Acta Metallurgica et Materialia* **1995,** *43,* 1087.

[64] B. C. Sales, in *Handbook on the Physics and Chemistry of Rare Earths* **2003,** *33*, 1.

[65] R. P. Hermann, F. Grandjean, D. Kafle, D. E. Brown, C. E. Johnson, S. M. Kauzlarich, G. J. Long, *Inorganic Chemistry* **2007,** *46*, 10736.

[66] J. F. Rauscher, C. A. Cox, T. Yi, C. M. Beavers, P. Klavins, E. S. Toberer, G. Snyder, S. M. Kauzlarich, *Dalton Trans.* **2009,** *39*, 1055.

[67] S. M. Kauzlarich, T. Yi, M. N. Abdusalyamova, F. Makhmudov, *Journal of Materials Chemistry* **2012**, *22*, 14378.

[68] W. Hume-Rothery, R. E. Smallman, C. W. Haworth, *The structure of metals and alloys.* The Institute of Metals, **1988**.

[69] A. L. Allred, E. G. Rochow, *Journal of Inorganic and Nuclear Chemistry* **1958,** *5*, 264.

[70] A. C. Payne, M. M. Olmstead, S. M. Kauzlarich, D. J. Webb, *Chemistry of Materials* **2001,** *13*, 1398.

[71] M. Levinshtein, M. Shur, in *Handbook series on semiconductor parameters,* World Scientific, **1995**.

[72] S. T. Eric, A. C. Catherine, R. B. Shawna, I. Teruyuki, F. M. Andrew, M. K. Susan, G. J. Snyder, *Advanced Functional Materials* **2008,** *18*, 2795.

[73] J. A. McCormack, J.-P. Fleurial, *MRS Proceedings*, **1991**, *234*, 135.

[74] C. Wood, D. Zoltan, G. Stapfer, *Review of Scientific Instruments* **1985,** *56*, 719.

[75] K. Vidyasagar, W. Hoenle, H. G. Von Schnering, *ChemInform* **1996,** *27,* D24-109.

[76] A. F. May, M. A. McGuire, J. Ma, O. Delaire, A. Huq, R. Custelcean, *Journal of Applied Physics* **2012**, *111,* 033708.

[77] F. Gascoin, S. Ottensmann, D. Stark, S. M. Hale, G. J. Snyder, *Advanced Functional Materials* **2005,** *15*, 1860.

[78] D. Sanchez-Portal, R. M. Martin, S. M. Kauzlarich, W. E. Pickett, *Physical Review B* **2002,** *65*, 144414.

[79] A. P. Holm, T. C. Ozawa, S. M. Kauzlarich, S. A. Morton, G. Dan Waddill, J. G. Tobin, *Journal of Solid State Chemistry* **2005,** *178*, 262.

[80] T. Caillat, A. Borshchevsky, J. P. Fleurial, *MRS Proceedings* **1997**, *478*, 103.

[81] S. R. Brown, E. S. Toberer, T. Ikeda, C. A. Cox, F. Gascoin, S. M. Kauzlarich, G. J. Snyder, *Chemistry of Materials* **2008,** *20*, 3412.

[82] H. Goldsmid, J. Sharp, *Journal of Electronic Materials* **1999,** *28*, 869.

[83] B. C. Sales, P. Khalifah, T. P. Enck, E. J. Nagler, R. E. Sykora, R. Jin, D. Mandrus, *Physical Review B* **2005,** *72,* 205207.

[84] L. Kleinman, *Physical Review* **1962,** *128*, 2614.

[85] J. Bardeen, W. Shockley, *Physical Review* **1950,** *80*, 72.

[86] M. V. Fischetti, *IEEE Transactions on Electron Devices* **1991,** *38*, 634

[87] D. M. Riffe, *Journal of the Optical Society of America B* **2002,** *19,* 1092.

[88] D. J. Bergman, O. Levy, *Journal of Applied Physics* **1991,** *70*, 6821.

[89] C. Yu, T. J. Zhu, S. H. Yang, J. J. Shen, X. B. Zhao, *Physica Status Solidi -Rapid Research*

Letters **2010**, *4*, 212.

[90] I. R. Fisher, S. L. Bud'Ko, C. Song, P. C. Canfield, T. C. Ozawa, S. M. Kauzlarich, *Physical Review Letters* **2000,** *85*, 1120.

[91] R. D. Shannon, *Acta Crystallographica A* **1976,** *32*, 751.

[92] C. A. Cox, S. R. Brown, G. J. Snyder, S. M. Kauzlarich, *Journal of Electronic Materials* **2010,** *39*, 1373.

[93] C. A. Uvarov, J. F. Rauscher, S. M. Kauzlarich, *Science of Advanced Materials* **2011,** *3*, 646.

[94] C. A. Uvarov, M. N. Abdusalyamova, F. Makhmudov, K. Star, J. P. Fleurial, S. M. Kauzlarich, *Science of Advanced Materials,* **2012**, *3*, 652.

[95] D. M. Rowe, C. M. Bhandari. in *Modern Thermoelectrics*, Holt, Rinehart and Winston, **1983**, 7.

[96] A. Zevalkink, E. S. Toberer, W. G. Zeier, E. Flage-Larsen, G. J. Snyder, *Energy & Environmental Science* **2011**, *4*, 510.

[97] M. E. Wieser, et al., *Pure and Applied Chemistry*, **2013**, *85*, 1047.

[98] E. Kane, in *Narrow Gap Semiconductors Physics and Applications* **1979,** *133*, 13.